National Chiao Tung University

Department of Mechanical Engineering

PhD Thesis

以平行化二維流體模型模擬 CF$_4$ 低溫電感耦合式電漿源蝕刻二氧化矽(SiO$_2$)之研究

Numerical Investigation of Carbontetrafluoride Inductively Coupled Plasma Source Considering Silicon Dioxide Etching Process Using a Parallel 2-D Axisymmetric Fluid Model

Student: Yuan-Ming Chiu (邱沅明)

Advisor: Dr. Jong-Shinn Wu (吳宗信 博士)

July 2012

以平行化二維流體模型模擬 CF$_4$ 低溫電感耦合式電漿源蝕刻二氧化矽(SiO$_2$)之研究

Numerical Investigation of Carbontetrafluoride Inductively Coupled Plasma Source Considering Silicon Dioxide Etching Process Using a Parallel 2-D Axisymmetric Fluid Model

研 究 生 ： 邱沅明　　　　　Student : Yuan-Ming Chiu

指導教授 ： 吳宗信 博士　　　Advisor : Dr. Jong-Shinn Wu

國 立 交 通 大 學

機 械 工 程 研 究 所

博 士 論 文

by

Yuan-Ming Chiu

B.Tech., National Dong Hwa University, Hualien, 2003

M.S., National Tsing Hua University, Hsinchu, 2006

A Thesis

Submitted in partial fulfillment of the requirements

for the degree of Doctor of Philosophy in Mechanical Engineering

in the Graduate College of the National Chiao Tung University, 2012

Hsinchu, Taiwan

July 2012

中文摘要

以平行化二維流體模型模擬 CF$_4$ 低溫電感耦合式電漿源蝕刻二氧化矽(SiO$_2$)之研究

國立交通大學機械工程學系

學生：邱沅明　　　　　　　　　　　　指導教授：吳宗信博士

本論文研究目的是發展、驗證與應用一個平行化二維軸對稱的電漿流體模型程式。本研究所使用的電漿流體模型程式包含了流體模型方程式、計算感應電磁場的 Maxwell's equations、計算靜電場的 Ambipolar 擴散模型、計算蝕刻二氧化矽表面鍵結情形的表面平衡方程式。我們是使用半隱式(semi-implicit)有限差分法離散流體模型所考慮的方程式。這些離散後的矩陣方程式則是使用 Krylov subspace (KSP)和矩陣前處理器(preconditioner)數值方法來求解。在計算的過程中，我們利用區域切割的平行計算方法來加快計算時間，處理器在計算期間所需要的資訊交換是透過 MPI 的函式庫來完成。接著，我們利用此一電漿流體模型來探討不同型式的 CF$_4$ 低溫電感式電漿源在蝕刻 SiO$_2$ 基版時所發生之電漿物理與化學特性。研究結果顯示 CF$_3^+$是主要的離子氣體，而負離子 F$^-$的濃度相較於正離子氣體稍微低一點，但是和電子相比，F$^-$的濃度卻相當的接近電子濃度，代表所模擬的電漿源為負離子電漿源。在中性氣體的模擬結果顯示活性自由基 F 原子氣體僅次於 CF$_4$ 進氣氣體，為最多的活性氣體; 另外，SiF$_4$、COF$_2$ 和 O$_2$ 為蝕刻 SiO$_2$ 時所產生最主要的蝕刻氣體，和實驗所量測之蝕刻產物氣體成分相當吻合。最後，模擬顯示螺旋式線圈和進氣口均圍繞在傳統腔體側邊的電漿源的蝕刻效率最好，因為不但有高蝕刻速率並且有良好的蝕刻均勻度。本研究主要可以分成四個部份。第一部分為二維軸對稱電漿流體模型方程式之描述，第二部分為

我們所使用的離散方法、數值方法和平行化的方法之簡介，第三部分為平行程式之驗證與平行效能測試，第四部分主要是利用所驗證的平行化流體模型程式來研究各種不同 CF_4 電感式電漿源。以下將一一簡單介紹每一部份。

在第一部分，我們將詳細介紹由波茲曼方程式推導出之電漿流體模型、Maxwell's equations 和表面動力模型。此電漿流體模型包含所有粒子的連續方程式、帶電粒子的漂移-擴散(drift-diffusion) 近似的動量方程式以及電子的能量方程式。流體模式中所需要的靜電場是依據 Ambipolar 擴散模型所得到。電子能量方程式所需要的電子吸收功率，則是計算 Maxwell's equations 得到軸向的感應電場並帶入 Ohmic heating 得到電漿吸收功率。程式裡面用來計算二氧化矽覆蓋率和表面化學特性的表面動力學也會在此部份中做一詳盡的介紹。

在第二部分，我們將介紹程式中計算流體的數值方法和平行化的計算。此部份一開始會詳細介紹離散化後之方程式。在每一時間步進中，我們使用 Krylov subspace method (KSP)和矩陣前處理(precondition)之組合求解離散化後之矩陣方程。為了加速計算的速率，我們使用區域切割計算方法來平行化這些計算之數值方法。

在第三部分，我們將驗證與測試所發展之平行化電漿流體程式的正確性和平行計算效能。程式之驗證是和 Fukumoto 等人[26][74]之前的研究結果作一比較，在同一模擬條件下所模擬的結果和他們所作之實驗和模擬數據非常一致。我們將所發展的平行化電漿流體模型在台灣國家高速電腦中心 IBM1350 的機器上作一效能測試，發現疊代法使用 GMRES 和矩陣前處理器使用 Block Jacobi 在網格數為 122×179 之電漿模擬能線性加速計算效能至 26 顆處理器。

在第四部分，我們利用所發展和所驗證的平行化電漿流體模型程式探討不同型式的 CF_4 電感式電漿源內之物理機制和化學特性。此部份所探討之電感式電漿源包括標準的 GECRC 電漿源、平板式線圈設計在傳統腔體上方的電漿源、螺旋式線圈設計在傳統腔體側邊的電漿源以及圓頂式腔體的電漿源。本部份的電漿流

體化學模型總共考慮 96 條氣相化學反應式和 27 條二氧化矽表面反應。首先，我們將詳盡地討論在 GECRC 電感式電漿源和圓頂腔體式電感式電漿源內之電漿氣體的空間分布、化學特性、蝕刻產物和化學反應速率。結果顯示不論在 GECRC 或是圓頂式腔體內部主要的離子氣體為 CF_3^+，原因為解離 CF_4 產生 CF_3^+ 的解離能在所有的解離反應為最低。而負離子 F^- 的濃度相較於正離子氣體稍微低一點，但是由於其電子附著反應能很低，使得 F^- 的濃度相當的接近電子濃度。此外，在中性氣體的結果發現氟原子氣體 F 僅次於 CF_4 背景氣體為最多的活性氣體，因為氟原子在游離反應中被大量的生成。此外，蝕刻過程所產生的蝕刻氣體大部份為 SiF_4、COF_2 和 O_2，其結果和很多實驗所量測結果一致。同時，我們應用此模型來探討各種電感式電漿源的蝕刻速率和蝕刻均勻度並幫助改進電感式電漿源的腔體設計。模擬結果顯示把螺旋式線圈和環狀進氣口兩者圍繞在傳統腔體測邊的電漿源之蝕刻效率最好，因為不但有高蝕刻速率並且有良好的蝕刻均勻度，其原因為電漿生成區域接近外圍基版，不會過度集中於腔體中間區域，使的蝕刻所需的活性離子氣體如氟原子氣體均勻地傳輸到基版。

　　此外，我們會將本論文研究的主要發現以及未來應進行之研究部分條列說明於論文之最後。

　　關鍵字：電感式電漿源; 流體模型; 平行計算; GECRC; 圓頂式電搞式電漿源; CF_4 氣體放電; 表面動力學

ABSTRACT

Numerical Investigation of Carbontetrafluoride Inductively Coupled
Plasma Source Considering Silicon Dioxide Etching Process Using a
Parallel 2-D Axisymmetric Fluid Model

Department of Mechanical Engineering

Student: Yuan-Ming Chiu   Advisor: Dr. Jong-Shinn Wu

This thesis reports development and validation of a parallel 2-D axisymmetric plasma fluid model which includes the fluid modeling equations for plasma transport, the Maxwell's equations for induced electric field, ambipolar diffusion for electrostatic electric field, and surface kinetic model for modeling SiO_2 etching. This model is discretized by using the semi-implicit finite difference method with preconditioned Krylov subspace (KSP) method for discretized modeling equations. The fluid modeling code is parallelized using domain decomposition method through the use of MPI protocol. We employ this plasma fluid model to study plasma physics and chemistry of tetrafluoromethane (CF_4) gas discharge considering the etching process of a SiO_2 substrate in different inductively coupled plasma (ICP) sources. The results show that CF_3^+ is the dominant charged species, and F^- concentration is comparable to that of electron. Reactive F atom is the most dominant radical in CF_4 discharge. In addition, the major etching products from the the substrate are SiF_4, COF_2 and O_2 in all ICP reactors considered in this thesis. Finally, the results show that it is possible to design an ICP reactor with relatively high and uniform etching rate with both gas inlet and coil arranged along the cylindrical wall. Researches in this thesis are divided into four major parts. The first part is the description of the fluid moldeing equations. The second part is the numerical schemes and algorithms for

solving the fluid modeling equations and corresponding parallel computing method. The third part is the description of validation and parallel performance of the parallel fluid modeling code. The fourth part is the description of applications of the developed fluid modeling code for study the CF_4 discharge in various inductively coupled plasma sources.

In the first part, the fluid modeling equations, derived from the velocity moments of Boltzmann equation, the Maxwell's equations and the surface kinetic model are introduced in detail. The fluid modeling equations include the continuity equations for charged and neutral species, the electron energy density equation, the momentum equations by the drift-diffusion approximation for the charged species, the ambipolar diffusion approximation for the electrostatic field. The power absorption that is needed in electron energy equation is solved through the Maxwell's equation. The surface kinetic model (or site balance equations) for CF_4 discharge etching SiO_4 is also introduced in this part.

In the second part, the numerical schemes and algorithms for solving fluid modeling equations and the corresponding parallel computing method are introduced. The discretized equations are presented in detail. A combined method of preconditioning and Krylov subspace method (KSP) are proposed to solve the large sparse algebraic linear system formed at each time step. Parallel computing of the fluid modeling code using domain decomposition is also reported.

In the third part, the validation and parallel performance of the developed parallel 2D axisymmetric plasma fluid model are reported. Simulations are compared reasonably well with the previous simulation and experimental results by Fukumoto *et al.* [26][74]. Parallel performance study shows that the fluid code is scalable up to 26 processors on the IBM-1350 at National Center for High-Performance Computing in

Taiwan using the combination of GMRES and Block Jacobi with sub-preconditioner ILU with a problem size of 122×179.

In the fourth part, we employ our developed and validated parallel plasma fluid model to study plasma physics and plasma chemistry of CF_4 discharge in different geometries of ICP reactors: a typical ICP reactor, a GECRC, and a dome-shaped ICP reactor. The plasma chemistry includes 96 gas-phase reaction channels and 27 surface reaction channels. The spatial distributions of various plasma properties, etching characteristics, and production rate are described in detail in the both GECRC and dome-shaped ICP reactor. The numerical results indicate that CF_3^+ is the dominant charged species because the threshold energy of electron-impact dissociative ionization reacting with the feedstock that produces CF_3^+ is the lowest among all dissociative ionization. In addition, F^- concentration is comparable to that of electron in the CF_4 discharge because dissociative-attachment energy of CF_4 is the lowest. Furthermore, the reactive F atom is found to be the most dominant radical in CF_4 ICP discharge. The major etching products from the substrate are SiF_4, COF_2 and O_2, which is consistent with the previous experimental observations. Meanwhile, this plasma fluid model is employed to study the etching characteristics in different geometries of ICPs reactor for predicting etching rate and corresponding uniformity on the substrate surface. The results show that the typical cylindrical ICP reactor with both gas inlet and coils arranged along the cylindrical wall gives relatively high and uniform etching rate because the dissociative ionization tends to peak off-axis to affect plasma density profile most likely off-axis so that the discharge region is flat and wide near the substrate. It proofs that this simulation tool could help to optimize the designs of large reactors with very low cost.

Finally, major findings and recommendations for future study are outlined at the end of the thesis.

ACKNOWLEDGMENTS

First and foremost the author is heartily grateful to his supervisor, Prof. Jong-Shinn Wu, whose encouragement, guidance and support from the initial to the final level enabled the author to develop an understanding of this research and implementation of this lengthy thesis. The author would also like to present his appreciations to Prfo. Feng-Nan Hwang (NCU) and Prof. Tsin-Fu Jiang (NCTU) who helped a lot during the course of this research. The author would also like to convey thanks to his thesis committee members (Prof. Shou-Shing Hsieh, Prof. Tong-Miin Liou, Prfo. Chwung-Shan Kou, Prof. Feng-Nan Hwang, Prof. Cheng-Che Hsu, Prof. Chi-Chuan Wang, and Prof. Yao-Hsien Liu) providing many valuable suggestions and insightful advice.

In addition, the author would also acknowledge Dr. Chieh-Tsan Hung, Dr. Hsin-Yun Chou, Dr. Ming-Hung Chiang, Dr. Yun-Min Lee, Fu-Li Li, Kai-Wen Cheng, Kai-Wen Cheng, Ya-Ju Lin, Kun-Mo Lin, Cheng-Chin Su, Tzu-Hao Chou, Bi-Ren Gu, Yi-Wei Yang, Chih-Tung Liu, Guan-Rung Lai, Wei-Cheng Hung, Chih-Wei Lu, Tsung-Han Lin, Wun-Ci Wu, Zheng-Ling Lu, Yu-Tsung Liu, Chih-Liang Liu, Ying-Chih Wang, I-Min Lin, Jyun-Jie Lin, Po-Tsun Shen, Ruei-Shang Chen, and Huang-Chin Chen for their endless supports, advice and their willingness to share their bright thoughts with him, which were very fruitful for shaping up his ideas and research.

Lastly, the author offers his regards and blessings to all of those who supported him in any respect during the completion of the reserarch.

Yuan-Ming Chiu

July 2012   Hsinchu, Taiwan

TABLE OF CONTENTS

XIII

LIST OF TABLES

LIST OF FIGURES

NOMENCLATURE

A   area (m^2)

$\vec{B}$ magnetic field

c velocity of light in vacuum

d   denotes an exact differential

d distance(m)

D diffusion coefficient (m^2/s)

$e\ or\ q$ unsigned charge on an electron (1.602×10^{-19} C)

$\vec{E}$ electric field (V/m)

f frequency (Hz)

i imaginary integer $\sqrt{-1}$

I current (A)

k Boltzmann constant $1.381 \times 10^{-23} J/K$

m_e electron mass 9.11×10^{-31} Kg

m_i ion mass

n density

p pressure

$Power$ power absorption

t time (s)

T_e electron temperature

$\Gamma_e \Gamma_i \Gamma_n$ flux of electron, ion and neutral

Δ denotes the change of a quantity

μ mobility (m^2/V-s)
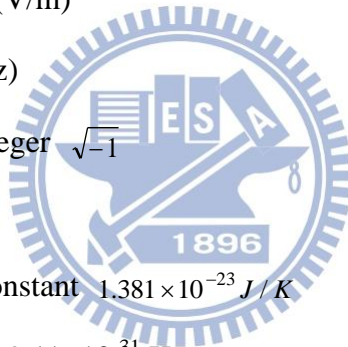
υ_m collision frequency of momentum transfer

σ cross section; electrical conductivity

φ electric potential ; azimuthal angle

ω_{pe} electron plasma frequency

ω_{RF} RF frequency

CHAPTER 1

INTRODUCTION

1.1 Background and Motivation

Plasmas which are ionized gases also known as discharge consist of positive ion, negative ion, electron and neutral species. In generally, plasma is treated as the fourth state of matter since sufficiently heating of a gas could give sufficient energy to ionize gas turning the gas into plasma. Plasmas are the most common phase state of matter in the universe, and they can be found from stars, interstellar matters to earth. According to ionization degree, plasmas can be divided from fully ionized gas (100%), such as stars, solar and fusion, to partially ionized gases (10^{-4}~10^{-6}), such as aurora, flames, and artificial plasmas. While generation of artificial plasmas via heating is very difficult to handle, it could be generated easily via electromagnetic wave in our daily lives as well as in industry. Artificial plasma generated in the laboratory and industry can be generally categorized by many aspects which include the type of power sources (DC, RF and microwave), operating pressure, temperature (thermal plasma $T_e=T_i$ and low-temperature non-equilbirium plasma $T_e >> T_i$), and application (light emission, material etching and material deposition, to name a few). The major fields of application may include: plasma processing, thin film deposition, plasma spray and bulk materials work, display systems, environmental and health applications, switches, relays, focus, antennas and power systems [1][3].

For the past three decades, the applications of glow discharge for manufacturing integrated circuit (IC) have increased tremendously in semiconductor industry, such as etching and deposition. These plasmas are often operated at low pressure because

1

of easier gas breakdown under this condition. Some low-pressure and high-density plasma sources had been invented in the semiconductor industry. These may include: capacitively coupled plasma (CCP), helicon discharge, electron cyclotron resonance (ECR), ion cyclotron resonance (ICR), and inductively coupled plasma sources (ICPs). In particular, among these high density plasma sources, inductively coupled plasma sources have been playing an important role in etching and nano-material deposition because of its advantages, such as high plasma density, controllable energetic ions, and potential of generating chemically active radical species [1][3][4][6]. The feed gases for ICPs' etching process are usually noble gases (He, Ne, Ar, Kr and so on) and halogen gases (Cl_2, CF_4, HBr and so on) in which fluorocarbon (CF_4) is generally encountered plasma etching of dielectrics in semiconductor fabrication. Such etching processes of dielectric usually damage and charge Si or SiO_2 contact layer; therefore, understanding of how etching rates and selectivity of SiO_2, caused by such a plasma, vary under different conditions are extremely important for a better etching of new devices [1][7][8].

Development of processing equipment for plasma etching had been accomplished mostly by trial-and-error approach; however, it was found that this approach was often time-consuming and very costly as the etching reactors become more complicated. It is generally difficult and very expensive to directly measure plasma properties within an ICP chamber. Due to the advancement of modern computer technology and numerical schemes, plasma modeling becomes an invaluable tool for understanding complex plasma physics and chemistry in ICP etching process. Indeed, plasma modeling for a realistic discharge system with complicated plasma chemistry (gas-phase and surface) and a large reactor size is often very time-consuming. [1][8][9]. Fortunately, parallel computation can efficiently

reduce the computational time [10], although there have been very few reports in this regard in the community [79]. Thus, it is important to develop and validate a parallel computational tool which can simulate the complex etching process of any ICP source considering realistic plasma physics and chemistry.

1.2 Overview of Low-Pressure Non-Equilibrium Plasma Sources

The common features of low-pressure non-equilibrium plasma sources include operations under low-pressure environment for easier gas breakdown (lower voltage) and different kinetic temperatures among different species (electron's temperature >> ion's temperater ≈ neutral's temperature). In general, the electron temperature is in the range of 1-10 eV, while the temperatures of ions and neutrals are not far from the room temperature. For polyatomic gas discharge, energy relaxation of rotational and vibrational temperatures is also impotant in maintaining the discgarge. For a glow discharge confined in a bounded space, there exists a large quasi-neutral region in the central part of the space with thin sheath regions closed the bounded walls. Because of frequent electron collision with neutral species, electronic excitations of neutral species and light emission due to de-excitation of electrons are very common in a glow discharge.

In this section, various kinds of low-pressure non-equilibrium plasma sources often found in semiconductor fabrication industry and especially the inductively coupled plasma source will be introduced.

1.2.1 Classification of Low-Pressure Gas Discharges in Semiconductor Fabrication

Several commonly seen low-pressure plasma sources, incuding direct current plasma (DCP), capacitively coupled plasma (CCP), electron cyclotron resonance (ECR), inductively coupled plasma (ICP) [1][3][4][5][6], are introduced in turn next.

1.2.1.1 Direct Current Plasma (DCP)

The direct current plasma is the simplest laboratory discharge, but it provides the basic understanding of fundamental discharge phenomena for other more complex discharges. When a sufficiently high electric field is applied between two electrodes placed in a gas, gas breaks down into positive ions and electrons, which is so-called gas discharge. The mechanism of gas breakdown in a DC plasma can be explained briefly as follows. First, a few electrons exist naturally in the universe and emitted from the electrodes due to the cosmic radiation from space. When a voltage is applied on an electrode, the electrons are accelerated by the electric field near the electrode and collide with the gas for exchanging energy and momentum. The most important collisions are the inelastic collisions that lead to excitation and ionization of neutral molecules. The excitation collisions, followed by de-excitations with the emission of radiation, are responsible for the terminology, glow discharge. The ionization collisions generate new electrons and ions. The ions are accelerated by the electric field toward the cathode, where they release new electrons due to ion or neutral bombardment, which is the so-called secondary electron emission. The electrons are accelerated in the sheath near the cathode, giving rise to new ionization collisions that generate new ions and electrons. These processes of secondary electron emission at the cathode and ionization in the plasma bulk make the glow discharge a

self-sustaining plasma. DC plasma with addition of magnetic field near the cathode (e.g., permanent magnet) can be used to deposit the material substrate as the anode using the sputtered atom which releases from material placed on the cathode. Nevertheses, it is seldom to apply DC plasma directly in industry. The reasons are described as follows. Firstly, the cathode is easily eroded by the ion bombardment which often releases metal material that is undesirable in materials processing. Secondly, although operated in low-pressure environment, the gap voltage often has to increase to several kVs for an acceptable plasma density for several practical applications. When a time-varying voltage is applied, the role of the electrodes becomes less important because electrons can oscillate in the plasma between the two electrodes. This is the so-called capacitively coupled discharge which is introduced next.

1.2.1.2 Capacitively Coupled Plasma (CCP)

As one of the electrodes of DC plasma is applied by an alternating voltage and the other grounded, each electrode acts alternately as either the cathode or anode, which is a typical capacitively coupled plasma (CCP). In a typical CCP, probability of heavy charged particles bombarding to the electrodes becomes low since they cannot respond quickly enough to the high-frequency oscillation of electric field. If one or both of the electrodes are non-conducting materials the charge accurmulated on electrodes will be partially neutralized by the opposite charge accumulated during the other half cycle. However, the frequency should be high enough so that half the period of the alternating voltage is less than the time during which the insulator would be charged up and bombarded. Otherwise, there will be a series of short-lived

discharges with the electrodes successively taking opposite polarities instead of a quasi-continuous discharge.

The frequencies generally used for these alternating voltages are typically in the radiofrequency (rf) range (100 kHz ~ 100MHz). The term "capacitively coupled" refers to the way of coupling the input power into the discharge, and the sheaths near two electrodes form one kind of capacitor. The electrons may have obtained energy from the oscillating electric field by the so-called Ohmic heating, and stochastic heating especially in low-pressure environment. Additionally, heating of the electrons can also be realized in the bulk plasma, when the bulk electric field is significant. This happens in the case of electronegative gases where radial losses due to ambipolar diffusion to the walls are important. However, for plasma processing applications, plasma density and mean free path of particles in a typical CCP are relatively low, which is not favored in etching process. In recent years, there have been new ideas by adding another lower frequency power source, named as dual-freqency CCP [80], for a better control of bombarding flux and energy of ions, which is used for etching purpose.

1.2.1.3 Electron Cyclotron Resonance Plasma (ECR)

Electron cyclotron resonance (ECR) plasma is generated from the interaction between an electric field at microwave frequency and a superimposed magnetic field, in which the electrons are in resonance with the microwave field. A characteristic feature of microwave is that the wavelength of power source (2.45 GHz) is comparable to the dimension of the plasma apparatus. ECR reactor consists essentially of two parts: a resonance region and a process region (with the surface to be treated). The plasma flows along the magnetic field lines from the resonance

region into the process region, where energetic ions and free radicals from the plasma can bombard the surface. When a magnetic field B is applied, the charged particles are confined and gyrating around the magnetic field lines with an angular cyclotron frequency that is a function of local magnetic field. When the cyclotron frequency is in resonance with the 2.45 GHz, very high power absorption by the electrons can be expected. This would lead to a high-density plasma generated in the chamber.

While the goals of high rates and low damage have been required in semiconductory fabrication industry, there are some disadvantages of the ECR technology. Firstly, the ECR resonance can lead to "mode hopping". Real wide-range fully automatic tuning of the microwave energy is difficult or impossible. It is very expensive to scale the technology up to large wafer sizes. Operation outside the resonance (at pressures > 2 mtorr) can lead to microwave energy transferring to the wafer [1][5][6].

A much simpler processing technology such as "Inductively Coupled Plasma" can possibly address all of the above problems. Today many major suppliers of plasma equipment utilize the ICP or similar technologies for high rate and low damage etch applications. The description of inductively coupled plasma will be introduced next.

1.2.1.4 Inductively Coupled Plasma (ICP)

In the inductively coupled plasma source, as shown in Figure 1 and Figure 2, the plasma chamber is surrounded by a high-frequency oscillating current coil. Simply speaking, the rf current in the coil generates an rf magnetic flux, which penetrates into the plasma region. According to Faraday's law, time-varying magnetic flux density

induces an azimuthal rf electric field, which accelerates the free electrons and sustains the discharge.

Inductively coupled plasma sources have the same required advantages, including the simplicity, no requirement for D.C. magnetic field, and operated in RF range rather than in microwave range. In contrast to ECRs, which can be configured to achieve plasma density $n_o \geq 10^{19}$ m^{-3}, inductively coupled discharges may have density limit, $n_o \leq 10^{19}$ m^{-3}, for an efficient power transfer to the plasma. However, the practical plasma density, $10^{17} \leq n_o \leq 10^{18}$ m^{-3}, for an efficient inductive discharge operation, is still typically 10 times higher than that of a capacitive RF discharge in the same pressure range (~ 1 Pa).

Major advantanges of ICP sources can be summarized as follows: [1][3][4][5][6]:

1. High etch rates are achieved by high ion density ($>10^{17}$ m^{-3}) and high radical density.

2. Control over selectivity and damage is achieved by lowering ion energy.

3. Separate control over ICP and electrode RF provides high process flexibility.

4. ICP source has combined effect of chemical and ion-induced etching.

5. ICP can be used for deposition in ICP-CVD mode, offering very dense films at lower temperature than PECVD and lower damage deposition onto temperature sensitive substrates.

1.2.2 Some Fundamentals of Plasma Physics

Plasma is loosely described as an electrically neutral medium of positive and negative particles (i.e., quasi-neutral). It is important to note that although these charged particles are unbound, but they are not totally free. When the charges move,

8

they generate electrical currents with magnetic fields, and as a result, they are affected by each other's fields. This governs their collective behavior with many degrees of freedom. A definition of plasma could have three criteria: the plasma approximation, bulk interaction, and plasma frequency [2].

The first criterion is plasma approximation. Charged particles must be close enough together that each particle influences many nearby charged particles, rather than just interacting with the closest particle. The plasma approximation is valid when the number of charge carriers within the sphere of influence of a particular particle is higher than unity to demonstrate collective behavior of the charged particles. This sphere is often called the Debye sphere whose radius is the Debye screening length.

The second criterion is bulk interaction. The Debye screening length is short compared to the physical size of the plasma. This criterion means that interactions in the bulk of the plasma are more important than those at its edges, where boundary effects may take place. When this criterion is satisfied, the plasma is quasi-neutral.

The third criterion is plasma frequency. The electron plasma frequency is large enough as compared to the electron-neutral collision frequency. When this condition is valid, electrostatic interactions dominate over the processes of ordinary gas kinetics. Briefly, collision frequency must be so sufficient that kinetic and statistical theory is valid.

In the following, some fundamentals of of plasma physics, including sheath, Debye length, Bohm velocity and plasma frequency, are described in turn next.

1.2.2.1 Debye Length

Debye length is the distance scale over which mobile charge particles screen out electric fields in plasmas and other conductors. In other words, the Debye length is the

distance over which significant charge separation can occur. A Debye sphere is a volume whose radius is the Debye length, in which there is a sphere of influence, and outside of which charges are screened. Debye length is expressed as [2][3][4][5]:

$$\lambda_{De} = \sqrt{\frac{\varepsilon_0 T_e}{q n_g}} \tag{1.1}$$

where ε_0 is the permittivity of free space, T_e is the electron temperature in eV, q is the elementary charge, and n_g is the background gas density. Overall speaking, it is a measure of the shielding distance or thickness of the sheath.

1.2.2.2 Plasma Sheath

The sheath is generated by the interaction of the plasma with the boundary material. As positive charges and electron diffuse thermally to wall, the sheath is formed that is caused by the velocity of electron is much larger than the velocity of positive ions. Physically this means that the electron density must be always less than the ion density in the sheath region. The function of a sheath is to form a potential barrier so that the more mobile electrons are confined electrostatically in the bulk. The height of the barrier adjusts itself so that the flux of electrons that have enough energy to overcome the barrier to the wall is just equal to the flux of positive ions reaching the wall.

1.2.2.3 Bohm Velocity

As the ions enter the sheath, they are accelerated by the large electric field and their density must decrease to maintain a constant flux. If this decrease is too fast, the ion density will fall off well before the electrons (which diffuse a bit into the region of positive potential) vanish, leading to a net negative charge, which would then increase the ion velocity. The stable solution must occur when the ions entering the sheath

have enough initial velocity to ensure that the sheath remains positive charged. The sheath can exist only if the initial ion velocity exceeds the critical condition at the presheath position, which is called Bohm sheath criterion. In the presheath region, a weak electric field penetrating into the plasma near the sheath edge, which accelerates the ions as they enter the "main" sheath. The initial velocity at the preshaeth position which could allow ion transport from the plasma bulk into the main sheath is known as Bohm velocity [3][4]:

$$u_s \geq u_B = \sqrt{\frac{qT_e}{M}}$$

(1.2)

where u_s is ion velocity, u_B is Bohm velocity and M is ion's mass. It only depends on electron temperature and mass of ion.

1.2.2.4 Plasma Oscillations (plasma frequency)

An important property of plasma is the time scale for plasma oscillations to occur. Plasma oscillations, also known as "plasma frequency" and "Langmuir frequency", are rapid oscillations of the electrons in conducting media such as plasmas or metals. The oscillations can be described as instability in the dielectric function of a free electron gas. In other words, under assumption of quasi-neutral plasma, if an electron is moved from its equilibrium position, the resulting positive charge exerts an electrostatic attraction on the electron, causing the electron to oscillate about its equilibrium position. Because the interaction between electrons is strong, they all oscillate together at a characteristic frequency that depends on the nature of the particular plasma. Electron plasma frequency is shown as [2][3][4]:

$$\omega_{pe} = \sqrt{\frac{q^2 n_0}{\varepsilon_0 m_e}}$$

(1.3)

11

where ω_{pe} is plasma frequency, ε_0 is permittivity of vacuum, and m_e is electron mass. The electron plasma frequency is the fundamental characteristic frequency of plasma that determines the time scale of a plasma response to external electric perturbations.

1.2.3 Classification of Plasma Chemistry

A major part of any plasma modeling is the description of the chemical reactions occurring in the gas phase and at surfaces in the plasma reactor. This description consists of a set of reaction paths with kinetic rate parameters for each reaction. For a low-pressure plasma process, the gas-phase reaction mechanism typically comprises a large set of electron-impact collisions as well as fast reactions between neutral radicals, ion-neutral reactions and ion-ion reaction. According to kinetic theory, the elementary processes can be expressed by some collision parameters such as cross section, reaction rate coefficient and collisional frequency where the transport coefficients and the rate constants related to electron are calculated by solving the Boltzmann equation [3][4]. For the current study, we consider a relatively complex set of plasma chemistry involving CF_4 gas, which will be presented in CHAPTER 2. Several important types of plasma chemistry often seen in gas discharges are described briefly for completeness in the following in turn .

1.2.3.1 Electron-Impact Reactions

Electron-impact reactions are by far the most important type of gas-phase reaction. Thus, mechanism development begins with the compilation of available electron-impact cross sections, starting with electrons impacting the atoms and molecules. There are a multitude of possible electron-impact excitation processes that

can occur for any target atom or molecule, but the mechanism development must focus on those collisions that are most likely to affect etching and deposition processes.

Plasma-enhanced etching and deposition chemistry depends on the kinds and impact fluxes of ions and radicals from the plasma bulk to the wafer surface. Therefore, processes such as ionization, excitation leading to dissociation, and dissociative ionization are of primnary importance. Moreover, a more complicated molecule would naturally have a number of paths such as dissociation and dissociative ionization. Many of the process gases typically used for materials processing applications also have electronegative properties where the amount of negative charges are sometimes comparable to that of electrons, so that electron attachment, dissociative attachment, and detachment reactions also need to be considered in the modeling.

Excitation of molecules resulting from electron impact need to be considered because the mean electron energy that drives ionization and dissociation processes is determined from a balance between the plasma power source and collisional energy losses. Hence, all processes that lead to significant energy loss of the electrons need to be considered. Typically, the data for electronic excitation to the lowest few excited states that sometimes refer to metastable excitation should be also included for a proper modeling, but not all the higher excited states.

1.2.3.2 Ion Related Reactions

Ion-neutral and ion-ion reactions often play a significant role in the plasma chemistry. In addition, mutual neutralization between positive and negative ions is an important loss process for ions in an electronegative discharge, and may also result in

atom transfer or molecular re-arrangements. A high density of negative ions in an electronegative discharge may also lead to appreciable electron detachment processes.

In general, the dominant positive ion in the discharge is expected to be related to the molecule or atom with the lowest ionization potential, provided the corresponding neutral is of sufficient abundance in the plasma. Charge-exchange reactions also provide a route for energy exchange between the ion and the neutral species. If the difference in ionization potential between two species is large, enough energy may be released by the charge transfer that may cause dissociation.

1.2.3.3 Neutral Related Reactions

Electron-impact reactions can generate a large amount of different radical species that participate in the etching or deposition processes at the wafer. In addition to surface reactions, these neutral species may react in the gas phase. Although radical recombination reactions are important, they often require stabilization by collision with a third body. It is sometimes reasonable to neglect these reactions entirely in a high-density plasma due to the very low-pressure environment. However, in some plasma such as SiH_4, the neutral reactions which form several large clustering species have to be considered.

1.3 Overview of Inductively Coupled Plasma Source (ICPs)

Inductively coupled plasma sources (ICPs) have been using frequently in semiconductor fabrication industry to produce high-density plasma for materials processing such as etching and deposition. The ICP source is the simplest type of high-density plasma source because it does not require an external magnetic field like ECR. The plasma in an ICP source is produced by radio frequency (RF) coils parallel

to the plasma source. The RF coils are separated from the plasma by a dielectric wall, and the discharge is typically operated with the frequency in the range of 1~40 MHz. The dielectric wall is part of the vacuum barrier and may be flat, domed, or cylindrical. Radio frequency currents in ICP coils induce opposing electric field (RF currents) in the plasma, which are concentrated primarily within a skin depth of the plasma surface, generally a few centimeters. The plasma thus acts as the secondary transformer with the ICP coils as the primary one.

The RF current in the plasma is carried primarily by electrons which rapidly transfer power to the plasma by frequent electron-neutral collision. High voltages on electrodes are not required in an ICP source, which leads to a very low plasma potential and low loss of charged particles to the wall. For example, the high plasma density produced in ICP sources, typically $> 10^{17}$ m^{-3}, which implies that the substrate sheath is relatively thin and fewer ion scatterings in the sheath as compared to capacitive coupled plasma sources because the debye length is relatively low [1][6].

Figure 1 and Figure 2 show the typical reactors of ICP with planar and cylindrical types of coil. In general, an ICP source consists of inductive coils, plasma chamber, RF generator, quartz window, match network and pumping system. Substrate hosting a wafer is often located at the bottom. Moreover, a dc voltage could be applied to the substrate for controlling the processing condition. A radio frequency (RF) current generator produces an oscillating current in an induction coil that is arranged around the chamber. The induction coil creates an oscillating magnetic field which produces an oscillating electric field being vertical to magnetic field according to the Maxwell's equations. The induced electric field alternately induces an oscillating current that is generated by the ions and electrons in the plasma. However, the magnitude of electromagnetic field, which transfers energy for electron to react

ionization, is relatively low if ICPs is operated in high presuree. Therefore, nonthermal ICP plasma discharges are usually operated at low pressure to make mean free path of electoron long enough to obtain sufficient energy and to make high electron conductivity to transfer the energy from skin depth to plasma bulk. From the viewpoint of an equivalent circuit, the characteristics between the inductive coil and plasma can be interpreted as a transformer. For an effective coupling of the plasma with the RF power supply, it requires a low plasma resistance. Thus, when ICPs are in a gas-discharge state, they are convenient to reach high currents, high electric conductivity and high electron density at relatively low electric field and voltage. The principle of heating plasma in an ICPs is related to electromagnetic field according to the Maxwell's equations,

$$\frac{1}{\mu_0}\nabla \times \vec{B} = \vec{J}_{total} + \frac{\partial(\varepsilon_0\vec{E})}{\partial t} = \frac{\partial \varepsilon \vec{E}}{\partial t} = \frac{\partial \vec{D}}{\partial t} \tag{1.4}$$

where $\vec{B}$ is inductive magnetic field, $\vec{J}_{total}$ is total current density and μ_0 is permeability of free space. The time-dependent current in the azimuthal direction induces time-dependent magnetic field in the r and z direction. We can calculate the time-dependent induced electric field in θ direction generated by the time-dependent magnetic field in term of Faraday's Law as

$$\nabla \times \vec{E} = -\frac{\partial \vec{B}}{\partial t} \tag{1.5}$$

Time-dependent induced electric field in the azimuthal direction can be applied to accelerate electrons leading to more energetic electrons to sustain the discharge. It has to be noted that power transferred from the electric field to the plasma is within a skin depth layer. The conductivity, wave, skin depth and Ohmic heating (power absorption) of ICP will be described in the following [3].

1.3.1 Dielectric Constant and Conductivity

Electron and ions in the plasma respond differently to an oscillating electric field because of the very large difference of masses between them. It can be shown that plasma acts like a dielectric medium in the range of GHz frequency. The plasma permittivity or dielectric constant is derived by combining the Maxwell's equations with the equation of motion. We can obtain an effective plasma dielectric constant as [3]

$$\varepsilon_p = \varepsilon_0 \left(1 - \frac{\omega_{pe}^2}{\omega(\omega + j\upsilon_m)} \right) = \varepsilon_0 + \frac{\sigma_p}{j\omega} \tag{1.6}$$

where σ_p is the plasma conductivity and it can be written as

$$\sigma_p = \frac{\varepsilon_0 \omega_{pe}^2}{\omega + j\upsilon_m} \tag{1.7}$$

where ω_{pe} is plasma frequency, ω is frequency of applied current, and υ_m is collisional frequency. At a lower frequency ($\omega < \omega_{pe}$) or in a low presuree (lower collisional frequency), σ_p is relatively high to act plasma like a good conductor.

1.3.2 Wave and Skin Depth in ICPs

Because plasma usually acts like a good conductor, the EM wave can only penetrate into distance within skin depth. To understand mechanism more, we start from wave propagation. The electric and magnetic fields of a RF EM wave, oscillating transverse to the direction of propagation x, have a spatial dependence given by E(x) ~ E$_0$ exp(jkx), where $k = \sqrt{\varepsilon_0}\,\omega/c$ is the propagation constant and c is the speed of light. For a low-frequency RF field, where $\omega < \omega_{pe}$ and $\sqrt{\varepsilon_0}$ is imaginary, the electric field

17

attenuates according to $E(x) \cong E_0 \exp(-\omega_{pe}x/c) = E_0 \exp(-x/\varsigma)$. The attenuation distance for RF fields in the plasma is given by the collisionless skin depth [3] as

$$\delta = c/\omega_{pe} \approx \frac{1.7cm}{\sqrt{n_e}} \qquad (1.8)$$

where n_e is the electron density in cm^{-3}. The skin depth is typically a few cm for the partially ionized low-pressure plasma that is relatively long enogh to heat low pressure ICPs comparing to real conductor (skin depth in ~mm), and the skin depth determines where the RF power is deposited in inductively coupled plasma (ICP) sources.

1.3.3 Ohmic Heating in an ICPs

Collisional heating (it is also named Ohmic heating or Joule heating) is present in all discharges as a result of the transfer of energy from the acceleration of electron in an electric field through collisional processes. Especially, under a sufficient large collision frequency but $\omega < \omega_{pe}$, the dominant electron heating mechanism is collisional heating because the collision frequency is very high. Although the electric field in the bulk plasma is small comparing to skin depth, it gives rise to a significant electron heating due to electron-neutral collisions. Collisional heating can be derived from the electron force equation. Since the mass of ion is much larger than electron, ion is very difficult to gain energy from an oscillating electric field. A significant electron heating due to electron-neutral collisions is given by the power absorption as

$$P_{abs} = \vec{J}(t) \cdot \vec{E}(t) \qquad (1.9)$$

where the total current induced by electric field is shown as

$$\vec{J}_{plasma}(t) = \mathrm{Re}[\tilde{J}_{plasma}e^{j\omega t}] \qquad (1.10)$$

and the current with a phase show as

$$\tilde{J}_{plasma} = \sigma_p \tilde{E} \qquad (1.11)$$

Substituting **(1.10)** and **(1.11)** into **(1.9)**, we could rewrite **(1.9)** as

$$p_{abs}(t) = \text{Re}[\tilde{J}_{plasma}e^{j\omega t}] \cdot \text{Re}[\tilde{E}e^{j\omega t}] \qquad (1.12)$$

The time average power per unit volume absorbed by the plasma is given by [3]

$$\bar{p}_{abs} = \frac{1}{T}\int_0^T \bar{J}_{plasma} \cdot \bar{E}dt = \frac{1}{T}\int_0^T p_{abs}(t)dt \qquad (1.13)$$

The ICP source is usually operated at the radio-frequency range with $\upsilon_m \ll \omega_{RF} \ll \omega_{pe}$, which is typical for a low-pressure RF discharge. Electrons could obtain the sufficient energy due to long mean free path in that reange frequency.

1.4 Literature Survey for Modeling ICP

The development of fluid model has been lasting for more than five decades. The early work using zero-dimensional or one-dimensional fluid models investigated the capacitively coupled discharges. Due to limitation of computer resources, the focus was on validations and refining modeling techniques by studying fundamental plasma physics. By the end of 1980s, the improvement of computer performance had improved the early work to combine the comprehensive chemistry with the Maxwell's equations, although it is still limited as one-dimensional. Later on by the end of 1990s, several two- and three-dimensional fluid models with detailed chemistry in studying inductively coupled plasmas were developed because of the necessary knowledge in design and optimization of new plasma processes in the semiconductor fabrication industry.

Until now, some groups applied the fluid model by solving momentum equations of ions and/or electron to analyze the dynamics of thin sheath. However, most of these were applied to electropositive plasmas such as Ar, Xe, He, and C_2H_2 [11][12][13].

19

Some other groups employed an approach, named ambipolar diffusion, to deal the presence of negative ions in plasma without considering the effect of sheath. Most of these were employed to simulate electronegative plasmas, such as Cl_2, CF_4, and SiH_4, which are important etching processes used in semiconductor industry [11][12][13]. In addition, there has been nearly no study about parallel computing of fluid modeling for ICPs. Table 1 and Table 2 summarize the list of past studies in modeling electropositive and electronegative inductively coupled plasmas using fluid model respectively. More details of the review are described in the following.

1.4.1 Numerical Modeling of ICPs

A plasma model is a computer program that numerically solves a system of equations describing the physical and chemical processes occurring in the plasma. Modeling and numerical simulations of plasma processing can be useful in many ways. An improved understanding of a plasma processing system can be achieved by comparing predictions from numerical simulations with experimental observations. The optimization of existing processes or the development of new plasma processes that offer better processing results may follow such an understanding. Modeling and simulations based on reliable physical or chemical modeling of a plasma processing system can significantly reduce the number of associated experiments that otherwise would have to be performed. Additionally, such modeling and simulations can also be used in the computer-aided design of new process system and to optimize fabricating processes within the framework of existing processing system.

Plasma simulation methods include kinetic and continuum methods [11][12][13]. The method for kinetic modeling is the Particle-In-Cell and Monte-Carlo-Collision (PIC/MCC) method, in which the plasma is modeled by a system of charged

superparticles that move in a self-consistent electromagnetic field and collide following given collision cross sections for different processes. Fundamentally, the PIC/MCC method solves the Boltzmann equation directly using no more than collision kinetics; however, it is generally very time-consuming and becomes impractical for a multidimensional simulation with complex plasma chemistry if the pressure is not too low. An alternative method, fluid model, is generally applied to simulate the plasma under imtermediate to high pressure conditions. It consists of the continuity equations, momentum equations and energy equations for various neutral and charged species in the plasma, which are obtained by taking velocity moments of the Boltzmann equation [14]. In addition, the Maxwell equations are often required to couple with fluid equations to obtain a self-consistent electric field. Among these equations, the momentum equation is the most difficult one to solve due to its highly nonlinear term. Therefore, a method called the drift-diffusion approximation is used, instead of solving the momentum equation directly when the momentum transfer collisional frequency is larger than the radio frequency (RF). However, the diffusion approximation may become highly questionable when the plasma density is high and the pressure is very low in the range of mtorr for a typical ICPs (i.e., collisionless sheath). Alternatively, the assumption of ambipolar diffusion [3] that does not consider the effect of sheaths has been employed successfully in the fluid model, in which the fluid model is still valid in a plasma bulk that was demonstrated by Meyyappan [52].

1.4.2 Electropositive ICP

Table 1 summarizes the past studies we have found in the literature for simulating electropositive ICPs using fluid modeling. In 1993, Ventzek and Kushner *et al.* [15] were the first group to publish a 2-D hybrid model consisting of

electromagnetic, electron Monte Carlo and hydrodynamic modules, and an offline plasma chemistry Monte Carlo simulation. They used this method to predict the distributions of the plasma density, plasma potential and ion fluxes for Ar, O_2, Ar/CF_4/O_2 gas mixtures operated at low pressure (10-20 mTorr).

In the same year, R. Stewar and Graves *et al.* [16] presented a 2-D fluid model that consists of the continuity equations for electron, ions and neutrals, the momentum equations for ions, drift-diffusion approximation for electron and neutral, the energy density equation for electron and the Poisson's equation for electrostatic potential. In this literature, they applied the assumed power profiles with solving the Maxwell's equation. They present the effect of neutral gas pressure on the plasma uniformity for an argon discharge in the range of 1-20 mTorr and the comparison between the fluid model and the global model. The same group, Stewar *et al.* [17], improved their model to include the Maxwell's equations. As a result, they had studied the power heating driven by external planar or cylindrical coils.

Lnmberoupoulos and Economou [18] used a 1-D fluid model to investigate the spatiotemporal dynamics of a pulsed-power inductively coupled argon plasma at 10 mTorr. Their model involved the continuity equations for all species, the drift-diffusion approximation for electron, the momentum equations for ions, the energy density equation for electron, the Maxwell's equation for induced electric field and the Poisson's equation for electrostatic electric field. Furthermore, an addition of RF bias applied in the model for modeling accelerated positive ions. The spatiotemporal dynamics and sheath thickness of argon plasma at 10 mTorr were investigated in detail by their model.

Later, Gao and Wang *et al.* [20] develop a 2-D hybrid Monte Carlo/fluid model, in which the method,is similar to Stewar, *et al.* [17], except they have obtained the electron energy distribution function (EEDF) through Monte Carlo simulations. They have further applied this model to investigate the mode transition of ICP [21], and study the variation of plasma parameters and EEDFs due to various discharge conditions [20].

1.4.3 Electronegative ICP

Table 2 summarizes the past studies we have found in the literature for simulating electronegative ICPs using fluid modeling. Modeling electronegative ICPs is more challenging than modeling electropositive ICPs. A 2-D fluid model applied to Cl_2 was first developed by Lymberopoulos and Economou *et al.* [22] in 1995. In their simulation, they assumed that the drift-diffusion approximation is still valid using a concept of "effective electric field", rather than solving the full momentum equations directly. In fact, this method only works well for capacitive coupled plasmas, and it would be a failure for inductively coupled plasma if assumation of azimuthal variation is axisymmetric. We actually double that method and model they report.

In 2001 and 2002, Ramamurthi and Economous *et al.* [23][24] did not apply effective electric field in their model. In contrast, a method, named ambipolar diffusion for dealing with the flux of charged particles, was adopted. A self-consistent fluid model, including the Maxwell's equation for power deposition, the electron energy density equation and the species mass balance, was proposed. The important assumptions of their model are summarized as follows: (1) The charged particle flux can be described by the drift-diffusion approximation since the pressure is larger than 10 mTorr, and (2) Electron heating is assumed to be collisional. The other assumptions

are similar to those of most other studies in the literature. The model was used to study a pulsed-power chlorine discharge sustained in an ICP reactor with planar coil.

Hash and Meyyappan *et al.* [25] employed the ambipolar diffusion for solving the continuity, electrostatic electric field and momentum equations using the drift-diffusion approximation. They also solved the energy equations of neutral species and electron. The space charge induced electric fields are given directly by the Boltzmann relation assuming that the plasma is quasi-neutral. The most important result they have found was that the neutral gas in ICP reactors heats up significantly in the plasma. The model was applied to study CF_4 discharge in a GEC chamber.

In 2006, Hsu and Graves *et al.* [19] had developed a fluid model in which they assumed the plasma is ambipolar and quasi-neutral so that the total flux of charged species outside the sheath is zero. The model equations for neutral species include overall mass continuity, momentum balance, energy balance and mass continuity for each species. In addition, the equations for charged species include the continuity equations for positive and negative ions, the energy density equation for electron, electric field from the balance of the summed flux of charged species and the Maxwell's equations for induced electric field. They have considered plasma chemistry involving Ar, mixtures of Ar and O_2 and mixtures of $Ar/O_2/Cl_2$. Moreover, they model the plasma as quasi-neutral everywhere. In their study, a comparison between the simulation and the experiment was performed.

Until very recently, Fukumoto *et al.* [26] present a two-dimensional fluid model, which assumes ambipolar diffusion, for etching SiO_2 substrate in a CF_4 ICP source, taking into account the plasma and surface chemistry of etch product species. The surface reaction model assumed Langmuir adsorption kinetics with the coverage of fluorine atoms, fluorocarbon radicals and polymers on SiO_2 surface. Their numerical

results indicated that etch products become a significant fraction of reactive ions and neutrals in the reactor, which in turn changes the plasma characteristics. While the plasma model include the surface kinetics, the density and the distribution of etch products in the reactor were changed by varying the ion bombardment energy on the substrate surface, gas pressure, mass flow rate and coil configuration, which arises in part from gas-phase reactions depending on plasma electron density and temperature.

1.4.4 Tetrafluoromethane CF_4 Discharge in ICPs

There have been some reports about modeling of tetrafluoromethane (CF_4) plasma in either capacitive coupled plasma or inductively coupled plasma that is used for etching purpose. Some of these reports focused on global modeling considering only gas-phase reactions [29][30][31][32], and some of them only considered feeding gas-phase reactions and highly simplified surface reactions using the concept of stick coefficients without taking any etching products into account [25][33][34][35]. It was found that etching products from the substrate significantly influence the composition of the gas phase species in a CF_4 glow discharge while etching SiO_2 and Si [36]. The etching of SiO_2 consumes F atom to form SiF_4, but the oxygen, released from the etching of SiO_2, reacts with CFx radicals to form CO, CO_2 and COF_2 [37].

Etching products were observed as important gas-phase reactants by several experiments. For example, Coburn $et~al.$ [36] found that the escaping oxygen hinders polymerization on the SiO_2 surface by forming volatile CO, CO_2 and COF_2, which allows etching process to continue under substrate surface without oxygen. Hikosaka $et~al.$ [38] used a quadrupole mass spectrometer (QMS) to measure CO^+ and SiF_3^+ in high power CF_4 discharge and found that they are produced mostly from quartz walls that could significantly deteriorate the etching selectivity of SiO_2 in an ICP reactor.

O'Neill and Singh [39] studied the surface effect on the concentration of gas-phase reactants in high-density etching plasmas by using ultraviolet-adsorption spectroscopy. COF_x^+ and CO^+ were detected in gas phase with oxygen radicals produced from a quartz substrate in CF_4 and CF_4/Ar ICPs [40][41][42]. The spatial concentrations of etching products such as SiF and SiF_2 were resolved through laser-induced fluorescence in inductively driven discharges containing C_2F_6 and C_4F_8 by Hebner [43][44]. Later, Cruden [45] applied Fourier transform infrared spectroscopy (FTIR) to detect SiF_4, CO and COF_2 from window etching products in a gaseous electronics conference reference cell (GECRC). Significant amounts of etch products, SiF_x^+/COF_x^+ (x=1~3), of quartz window were also detected by Rao *et al.* [48][49] and Zhou *et al.* [50]. To summarize, for an accurate modeling of CF_4 ICP discharge, fluid model has to consider not only the gas-phase plasma chemistry but also the surface reactions.

Because etching products are important as well as gas-phase reactants resulting from feedstock gases in a high-density plasma, both the complex gas and surface chemical reactions in CF_4 plasma have to be considered in fluid model to reproduce the major characteristics of etching process. Zhang *et al.* [51] were among the first group working on combination of plasma gas and surface model. They used a hybrid model coupled with a surface kinetics model to simulate CF_4 discharge for etching Si in CF_4. Fukumoto *et al.* [26] employed a fluid model coupled with a surface site balance model to simulate CF_4 plasma etching SiO_2 in a reactor with simple geometry without considering detailed gas-phase reactions of CF_4. Since they solved the Maxwell's equations using the Biot-Savart's law analytically and fluid model without parallel computation, their method can only be applied to simple reactor geometry. The Biot-Savart's law is analytic solutions which do not consider the plasma induced

electric field. In addition, the computational time may become prohibitively high for the fluid modeling combining with surface kinetic model when considering very complex gas phase and surface reactions. Thus, how to speed up the fluid modeling for a realistic inductively coupled plasma source is important, which is one of the major objectives in this thesis.

In conclusion, some groups adopted solving full momentum equations of ions instead of drift-diffusion approximation for electropositive plasma, and some groups used drift-diffusion approximation of charged species coupling with flux balance and ambipolar diffusion but for electronegative plasma. For CF_4 discharge, thses reports almost used drift-diffusion approximation and flux balance to study typical cylindrical reactor and GEC chamber. The summarization of literature survey was list as Table 1 and Table 2 in detail.
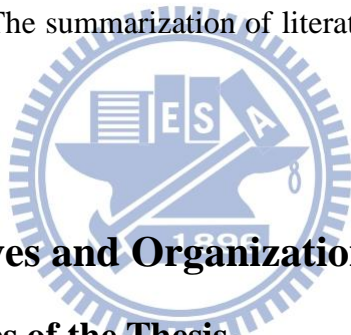
1.5 Specific Objectives and Organization of this Thesis

1.5.1 Specific Objectives of the Thesis

The specific objectives of the thesis are summarized as follows:

1. To develop a parallel 2D axisymmetric fluid model coupling with the Maxwell's equations and a surface kinetic model;

2. To validate the above fluid model code by comparing with previous simulations and experiments wherever available;

3. To parallelize the fluid model on distributed-memory machine using Message Passing Interface (MPI) [73];

4. To study the parallel performance of the above parallel fluid modeling code;

5. To apply the parallel fluid modeling code to predict plasma characteristics with etching SiO_2 substrate in a CF_4 discharge considering complicated gas-phase and surface reactions;

6. To investigate plasma and surface characteristic in different configurations of ICP sources such as gaseous electronic conference reference cell (GECRC) and dome-shaped reactor.

1.5.2 Organization of the Thesis and Research Framework

First, Figure 3 shows the research framework of this thesis. This framework consists of Background, Motivation, Objectives, Computational Model, Validation, Results and Discussion. It is clear that there are three major sets of results discussed: GECRC, dome-shaped reactor, and comparision among different geometries of ICP reactors. Chapter 1 describes the background and motivation of focusing on the fluid modeling of inductively coupled plasmas in this thesis. Chapter 2 presents in detail a 2-D fluid model consisting of fluid modeling equations, the Maxwell's equation and surface model, and corresponding numerical schemes and algorithms. Chapter 3 presents the validation and parallel performance of the developed fluid modeling code. Chapter 4 describes the results of simulating CF_4 plasma in GECRC and dome-shaped reactors using the fluid modeling code presented in Chapter3. In addition, comparison of etching characteristics at the substrate surface using various kinds of ICP reactor configurations is also presented. Finally, Chapter 5 summarizes the major findings of this thesis and recommendations of some possible directions for future research.

CHAPTER 2
NUMERICAL METHODS

2.1 Introduction

In this chapter, we will describe proposed fluid model for studying the plasma physics and chemistry of ICP sources. The model consists of the fluid modeling equations, the Maxwell's equation and the surface site balance equations, and the ambipolar diffusion assumption for static electric field. In the case of electronegative plasma, the thin sheaths near the walls are not considered in the model since the sheath thickness are typically only hundreds of microns in the high density plasma for a typical ICP source. It was found that the accuracy of the solution is not affected much without considering the existence of sheaths. Thus, we assume that the electronegative plasma is ambipolar and quasi-neutral without considering thin sheaths, which had been adopted by Hsu *et al.* [19], Ramamurthi *et al.* [23][24], and Fukumoto *et al.* [26].

Figure 4 shows the architecture of the proposed simulation model. The model consists of several key modules which include: Chemistry Module, Geometry Module, Electric Field Module, Electron Module, Ion Module, Neutral Module, Maxwell's Equations Module and Surface Kinetic Module. Figure 5 illustrates the major physical and chemical processes that occur within a plasma processing reactor. It shows an inductively coupled plasma reactor (e.g., GECRC) with a top coil that induces an azimuthal electric field. The electrons are accelerated by absorbing energy through the movement in the induced electric field and collide with neutral species for ionization,

excitation and dissociation, to name a few. This necessitates the consideration of electrodynamics and gas kinetics at the same time. In addition, the species in discharge region diffuse (and drift for charged species) to react with wall and substrate by considering the transport phenomena and surface kinetics. Finally, the etching products and etching properties are predicted as a steady solution is obtained.

In this following, all the important model equations, including the fluid model equations, the Maxwell's equations, the surface site balance equations, CF_4 gas-phase reactions, surface reactions with SiO_2 substrate, are introduced in turn. Finally, the numerical schemes and algorithm in solving these nonlinear coupled partial differential equations are presented.

2.2 Fluid Model Equations

In this study, because Knudsen number ($Kn = \lambda/L$ where λ is mean free path and L is a characteristic dimension of the reactor) for electron is approximately 0.05 and for CF_4 is approximately 0.01, the fluid approximation was used. The Peclet number ($Pe = LU/D$ where U is velocity and D is mass diffusion) for CF_4 is approximately 0.09, and the Reynolds number ($Re = LU\rho/\mu$ where ρ is mass density and μ is viscosity) for CF_4 is approximately 1200. Therefore, it is reasonable that the fluid model is valid, and the transports of neutral species adopt only effect of diffusion in this situation. The summary of these nondimentional numbers was summarized in Table 12. From the moments of the Boltzmann equation, we can obtain the macroscopic conservation equations that describe the averaged quantities, such as species density, mean velocity and energy density [2][3]. These equations involve continuity equation, momentum equation and energy density equation. In the fluid model, the general continuity equations for all species can be written as

$$\frac{\partial n_\alpha}{\partial t} + \nabla \cdot \left(n_\alpha u_\alpha \right) = R_{\alpha,\text{source}} - R_{\alpha,\text{sink}} \qquad (2.1)$$

Momentum equations for all species can be written as

$$m_\alpha n_\alpha \left\{ \frac{\partial \vec{u}_\alpha}{\partial t} + \left(\vec{u}_\alpha \cdot \nabla \right) \vec{u}_\alpha \right\} = q_\alpha n_\alpha \left(\vec{E} + \vec{u}_\alpha \times \vec{B} \right) - \nabla p_\alpha + \sum_{\alpha \neq \beta} \vec{P}_{\alpha\beta} \qquad (2.2)$$

where α denotes for electron, charged species and neutral species; n_α is the density of

the αth species; $\vec{u}_\alpha$ is the velocity of the αth species; $R_{\alpha,\text{source}}$ is the rate of generating

the αth species per unit volume; $R_{\alpha,\text{sink}}$ is the rate of destroying the αth species per unit

volume; m_α is the αth species mass; q_α is the charge of the αth species; $\vec{E}$ is the

electrostatic field; $\vec{B}$ is the external applied magnetic field; p_α is the pressure

generated by the αth species; $\sum_{\alpha \neq \beta} P_{\alpha\beta}$ is the summation of momentum transferred by

the αth species colliding with other species β.

In addition, the temperature of electron is governed by the electron energy density

equation as

$$\frac{\partial}{\partial t} \left(\frac{3}{2} n_e k T_e \right) + \nabla \cdot \left(\frac{3}{2} n_e k T_e \vec{u}_e \right) + n_e k_B T_e \nabla \cdot \vec{u}_e = -\nabla \cdot \vec{Q}_e + \sum_{\alpha \neq \beta} E_{\alpha\beta} \qquad (2.3)$$

where k_B is the Boltzman constant; T_e is the electron temperature; Q_e is the

electron energy flux; $\sum_{\alpha \neq \beta} E_{\alpha\beta}$ is the summation of energy transferred by the αth species

colliding with the other species β.

For the momentum equations, the drift-diffusion approximation is often used

instead of solving the momentum equations directly. Firstly, we assume that the

background species is at rest or the velocity is small and that the momentum transfer

frequency υ_α is a constant, independent of the drift velocity. Secondly, we assume the

plasma properties vary slowly with time; we can thus neglect the inertial term

$(\vec{u} \cdot \nabla \vec{u})$ and the magnetic forces in the momentum equations. In turn, pressure and collision can be written as $\sum_{\alpha \neq \beta} E_{\alpha\beta} = -m_\alpha n_\alpha \upsilon_\alpha \vec{u}_\alpha$ and $p_\alpha = n_\alpha k_B T_\alpha$ respectively. Thirdly, only the stead-state solution is considered. Then, the momentum equation (**2.2**) can be further simplified as

$$q_\alpha n_\alpha \vec{E} - \nabla(n_\alpha k_B T_\alpha) - m_\alpha n_\alpha \upsilon_\alpha \vec{u}_\alpha = 0 \qquad (2.4)$$

After rearranging the above, we can obtain

$$\vec{u}_\alpha = -\frac{1}{m_\alpha n_\alpha \upsilon_\alpha} \nabla(n_\alpha k_B T_\alpha) + \frac{q_\alpha}{m_\alpha \upsilon_\alpha} \vec{E} \qquad (2.5)$$

With this, one can obtain flux $\vec{\Gamma}_\alpha$ as

$$\vec{\Gamma}_\alpha = n_\alpha \vec{u}_\alpha = -\frac{1}{m_\alpha \upsilon_\alpha} \nabla(n_\alpha k_B T_\alpha) + \frac{q_\alpha n_\alpha}{m_\alpha \upsilon_\alpha} \vec{E} \qquad (2.6)$$

Equation (**2.6**) can be rewritten as

$$\vec{\Gamma}_\alpha = n_\alpha \vec{u}_\alpha = -\nabla(D_\alpha n_\alpha) \pm \mu_\alpha n_\alpha \vec{E} \qquad (2.7)$$

Equation (**2.7**) is the so-called the drift-diffusion approximation as mentioned earlier. In the drift-diffusion approximation, the transport of charged particles is described as the combined effect of a drift flux caused by an electric field, and a diffusion flux caused by density gradients. At a fixed RF frequency of 13.56MHz, the range of pressures for which the drift-diffusion approximation can be properly applied depends mainly on two criteria. The first is the characteristic time of the charged particle has to be much smaller than the RF oscillation period, i.e., $\tau_m \gg f_{RF}$. This condition means that we assume charged particles react almost instantaneously to variations of the electric field. This applies well to electron, which is very light and has a very small characteristic time. The second is the collisional mean free path has to be much smaller than the characteristic gradient lengths, i.e., $\frac{v_\alpha}{\upsilon_\alpha} = \lambda_\alpha \ll L$. The above two criteria correspond to the transport of charged particles is dominated by collision.

In a typical ICP chamber, the mean free path for electron is ~ mm in a ICP chamber (e.g., 20 mtorr), which is much smaller than the chamber size. Therefore, the drift-diffusion approximation can replace the full momentum equations for all charged species in the present study. Thus, the continuity equations for all charged species using the drift-diffusion approximation can be rewritten as

$$\frac{\partial n_\alpha}{\partial t} + \nabla \cdot \vec{\Gamma}_\alpha = R_{\alpha,\text{source}} - R_{\alpha,\text{sink}} \tag{2.8}$$

Similarly, the electron energy density equation can be rewritten as

$$\frac{\partial}{\partial t}\left(\frac{3}{2}n_e k_B T_e\right) = -\nabla \cdot \vec{Q}_e - e\vec{\Gamma}_e \cdot \vec{E}_s + P_{abs} - P_{coll} \tag{2.9}$$

where $\vec{Q}_e = \frac{5}{2}k_B T_e \vec{\Gamma}_e - \frac{5}{2}\frac{n_e k_B T_e}{m_e \upsilon_e}\nabla(k_B T_e)$ is the electron energy flux, υ_e is the electron-neutral collision frequency, P_{abs} is the externally deposited power per unit volume through coils, and P_{coll} is the power lost per unit volume due to electron-neutral elastic collisions. Eventually, (2.7), (2.8), and (2.9) are solved together numerically in our simulation model that will described in detail later.

In brief summary, the current fluid modeling includes the following model equations:

1. The continuity equations for various ions with drift-diffusion approximation;

2. The continuity equations for various neutral species;

3. The electron energy density equation with electron current density from flux balance relation;

4. Quasi-neutrality enforcement for the electron number density;

5. The flux balance relation for the electrostatic electric field;

6. The Maxwell's equations for the electron power absorption.

More details of the model equations are introduced in turn in the next few sections.

2.2.1 Transport Equations for Charged Species

The continuity equation for ions can be written as

$$\frac{\partial n_\alpha}{\partial t} + \nabla \cdot \vec{\Gamma}_\alpha = R_{\alpha,\text{source}} - R_{\alpha,\text{sink}} \qquad (2.10)$$

where n_α is the αth ion number density, $R_{\alpha,\text{source}}$ and $R_{\alpha,\text{sink}}$ are source and sink terms

of αth ion species, respectively, resulting from chemical reactions. Based on the

drift-diffusion approximation, $\vec{\Gamma}_\alpha$ is the αth ion flux that can be written as

$$\vec{\Gamma}_\alpha = -D_\alpha \nabla n_\alpha \pm \mu_\alpha n_\alpha \vec{E} \qquad (2.11)$$

where $\vec{E}$, μ_α, and D_α are the electrostaic electric field, the mobility of the αth ion,

and the diffusivity of the αth ion, respectively. In the current study, the mobility of αth

ion in background neutral species β is calculated by using the Langevin mobility

expression at low electric field and the mobility of αth ion in the background gas

mixture is obtained using the Blancs law [33]. In addition, corresponding diffusivities

of all ion species are calculated through the Einstein relation.

Instead of solving sheath dynamics directly, flux balance of ions and electron is

assumed in the current study, which is similar to previous studies [3]. Thus, the

electrostatic electric field can be written as

$$\vec{E}_{r,z} = \frac{\sum_+ D_+ \nabla n_+ - \sum_- D_- \nabla n_- - D_e \nabla n_e}{\sum_+ \mu_+ n_+ + \sum_- \mu_- n_- + \mu_e n_e} \qquad (2.12)$$

where the subscript $+$, $-$ and e refer to positive ion, negative ion and electron,

respectively. $\Gamma_+, \Gamma_-, \Gamma_e$ are the particle fluxes, D_+, D_-, D_e are the diffusivities, and

μ_+, μ_-, μ_e are the mobilities. On the other hand, electron number density and electron

flux are obtained from the enforcement of quasi-neutrality and flux balance based on

the assumption of ambipolar diffusion, which are expressed as:

$$\sum_{+} \Gamma_{+} = \sum_{-} \Gamma_{-} + \Gamma_{e} \tag{2.13}$$

$$\sum_{+} n_{+} = \sum_{-} n_{-} + n_{e} \tag{2.14}$$

2.2.2 Transport Equations for Neutral Species

The general continuity equation for neutral species, assuming diffusion dominated flow under low-pressure condition, can be written as

$$\frac{\partial n_k}{\partial t} + \nabla \cdot (D_k \nabla n_k) = R_{k,\text{source}} - R_{k,\text{sink}} \tag{2.15}$$

where n_k is the density of the kth neutral species, $R_{k,\text{source}}$ and $R_{k,\text{sink}}$ are source and sink terms of the kth ion species, respectively, summed from various chemical reactions involving the kth ion species, and D_k is the diffusion coefficient of the kth neutral species in a mixture of background gas. The latter is obtained by the Blancs law with binary diffusion coefficient calculated using Chapman-Enskog kinetic equation [27] as follows:

$$D_{kl} = 0.0018585 \times 10^{-4} \times \sqrt{T^3 (\frac{1}{M_k} + \frac{1}{M_l})} \bigg/ P_{tot} \sigma_{kl}^2 \Omega_{D,kl} \tag{2.16}$$

where $T(k^o)$, $M_k(a.m.u.)$, $M_l(a.m.u.)$, $\sigma_{kl}(\overset{o}{A})$, and $\Omega_{D,kl}$ are the gas temperature, the molecule weight of the kth and jth neutral species, Lennard-Jones parameter, and the dimensionless collisional integral, respectively.

The Neumann boundary condition is applid at the axis of symmetry. The thermal flux of $\frac{1}{4} n \sqrt{8 k_B T_g / \pi M_k}$ is enforced at all solid surfaces. Feedstock gas CF$_4$ is taken as a gas flowing into the discharge region from a gas inlet, and an adjustable amount of all neutral species at the outlet boundary are pumped out of the chamber by a pumping outlet. The flux of feedstock gases entering the reactor chamber is

proportional to the preset mass flow rate S_{in} (sccm) at the inlet so that the total flux of gas inlet is $\vec{\Gamma}_{in} = 2.6868 \times 10^{25} \cdot S_{in} / Area$ where *Area* is the total inlet area. The loss of neutral species due to pumping is controlled by the flux $\vec{\Gamma}_{out}$ at the gas outlet boundary, which is adjusted to maintain a preset chamber pressure throughout the simulation. The adjusting method of pumping rate is described in the section 2.6 (boundary condition).

2.2.3 Electron Energy Density Equation

The electron energy density equation is expressed as,

$$\frac{\partial n_\varepsilon}{\partial t} + \nabla \cdot \vec{Q}_e = -e\vec{\Gamma}_e \cdot \vec{E}_s - \sum_l S_l \varepsilon_{loss} - 3\frac{m_e}{M} n_e k_B \nu_e (T_e - T_g) + P_{abs} \quad \textbf{(2.17)}$$

where $n_\varepsilon \left(= \frac{3}{2} n_e k_B T_e \right)$ is the electron energy density, T_e is the electron temperature, ε_{loss} is the energy loss for the lth inelastic electron collision, k_B is the Boltzmann constant, ν_e is the exchange momentum collision frequency between electron (mass m_e) and background neutral (mass M), T_g is the background gas temperature, P_{abs} is power absorption given by Equation **(2.34)** and $\vec{Q}_e$ is the corresponding electron energy density flux as,

$$\vec{Q}_e = \frac{5}{2} k_B T_e \vec{\Gamma}_e - \frac{5}{2} \frac{n_e k_B T_e}{m_e \upsilon_e} \nabla (k_B T_e) \qquad \textbf{(2.18)}$$

where $\vec{\Gamma}_e$ is the electron flux obtained from Equation **(2.13)**. In addition, boundary condition at walls based on thermal diffusion is applied as $\vec{Q}_e = 2k_B T_e \vec{\Gamma}_e$ [3], and $\vec{Q}_e = 0$ at the axis of symmetry.

2.3 Maxwell's Equations for Electron Power Absorption Calculation

2.3.1 Vector Wave Equation

The electromagnetic field in plasma generated by the antenna coil can be obtained by solving the general homogeneous vector wave equation that is derived from the Maxwell's equations. Because the arrangement of the coils and is generally approximately as axisymmetric, only the azimuthal component of electromagnetic field needs to be computed. The Maxwell's equations are written as

$$\nabla \cdot \vec{E} = \frac{\rho_{total}}{\varepsilon_0} \qquad \text{(Gauss's law)} \qquad \textbf{(2.19)}$$

$$\nabla \cdot \vec{B} = 0 \qquad \text{(Divergence-free magnetic field)} \qquad \textbf{(2.20)}$$

$$\nabla \times \vec{E} = -\frac{\partial \vec{B}}{\partial t} \qquad \text{(Faraday's law)} \qquad \textbf{(2.21)}$$

$$\nabla \times \vec{B} = \mu_0 \vec{J}_{total} + \frac{1}{c^2} \frac{\partial \vec{E}}{\partial t} \qquad \text{(Ampere's law with Maxwell's correction)}$$

$$\textbf{(2.22)}$$

where ρ_{total} is the total space charge density, and c is speed of light. ρ_{total} is expressed as $\rho_{total} = \rho_{free} + \rho_{bound}$. However, $\rho_{free} = 0$ and $\rho_{bound} \approx 0$ in the quasi-neutral plasma bulk. Then, applying the curl to **(2.21)** and using vector identity, we obtain:

$$\nabla(\nabla \cdot \vec{E}) - \nabla^2 \vec{E} = -\frac{\partial}{\partial t}(\nabla \times \vec{B}) \qquad \textbf{(2.23)}$$

Because $\rho_{total} \approx 0$ in plasma, we obtain $\nabla \cdot \vec{E} = 0$. Then we substitute **(2.22)** into **(2.23)** to obtain the vector wave equation as

$$\nabla^2 \vec{E} = \mu_0 \frac{\partial \vec{J}_{total}}{\partial t} + \frac{1}{c^2} \frac{\partial^2 \vec{E}}{\partial t^2} \qquad \textbf{(2.24)}$$

where $\vec{J}_{total} = \vec{J}_{free} + \vec{J}_{bound} + \vec{J}_{polarization}$ is a general form of current density. $\vec{J}_{free}$ is the free current density caused by the movement of free electrons. $\vec{J}_{bound}$ is the bound current density caused by magnetic polarization. $\vec{J}_{polarization}$ is the polarization current density caused by electric polarization. Equation **(2.24)** is a general form of vector wave equation, which provides the temporal and spatial evolution of electromagnetic wave. In the current study, we are interested in solving the EM wave evolution within an ICP chamber, which consists of various regions including plasma region, quartz region, coil region and air region. In each region, the form of $\vec{J}_{total}$ is different, which is described next in turn.

2.3.1.1 Plasma Region

We can write the total current density through the Ohm's law if the bound current and polarization current are ignored, because the plasma bulk acts like a conductor. For most conductors, the current density is proportional to the force per unit charge that is the Lorentz force $\vec{E} + \vec{v} \times \vec{B}$. However, the induced magnetic field is small such that only electrical force needs to be considered. Thus, the total current density in plasma is proportional to the electric field:

$$\vec{J}_{total} = \vec{J}_{free} = \sigma_p \vec{E} \qquad (2.25)$$

where σ_p, as shown in equation **(1.7)**, is the effective plasma conductivity. We can further separate it into real and imaginary parts as follows:

$$\sigma_p = \frac{\varepsilon_0 \omega_{pe}^2 \upsilon_m}{\omega^2 + \upsilon_m^2} - j \frac{\varepsilon_0 \omega_{pe}^2 \omega}{\omega^2 + \upsilon_m^2} = \sigma_{p,R} + i\sigma_{p,I} \qquad (2.26)$$

2.3.1.2 Quartz Region

We can ignore both the free current and bound current densities because their effects are small in the quartz region. Therefroe, we only consider the polarization current density as follows:

$$\vec{J}_{total} = \vec{J}_{pol} = \frac{\partial \vec{P}}{\partial t} = \frac{\partial(\varepsilon_0 \chi \vec{E})}{\partial t} \tag{2.27}$$

where $\vec{P}$ is the electric polarization, ε_0 is the permittivity of vacuum, and χ is the electric susceptibility. By substituting Equation **(2.27)** into Equation **(2.24)**, we can obtain

$$\nabla^2 \vec{E} = \mu_0 \frac{\partial^2 \varepsilon_0 \chi \vec{E}}{\partial t^2} + \frac{1}{c^2}\frac{\partial^2 \vec{E}}{\partial t^2} = \mu_0 \varepsilon_0 (1+\chi)\frac{\partial^2 \vec{E}}{\partial t^2} = \mu_0 \varepsilon_0 \varepsilon_r \frac{\partial^2 \vec{E}}{\partial t^2} = \frac{\varepsilon_r}{c^2}\frac{\partial^2 \vec{E}}{\partial t^2}$$

$$\tag{2.28}$$

where ε_r is relative dielectric constant is set to be 3.8 for quartz. The term in the right-hand side is refered to be the so-called displacement current density.

2.3.1.3 Coil Region

In the coils, only the free current desity exists. Thus, the total current density is expressed as

$$\vec{J}_{total} = \vec{J}_{free} = \vec{J}_0 \cos \omega t \tag{2.29}$$

where $\vec{J}_o$ is the amplitude of applied RF current density in the coils. The coil is 6 mm in diameter throughout the study, unless otherwise specified.

2.3.1.4 Air Region

Since there is no any free current in the air, the total current density is zero. As follows:

$$\vec{J}_{total} = 0 \qquad\qquad\qquad\qquad (2.30)$$

2.3.1.5 Maxwell's Equations in Alternative Form

We now consider plasma driven by a small amplitude time-varying current that produces a small amplitude time-varying electric field. The coil current density and induced electric field can be written in complex function known phase domain solution, respectively, as

$$\vec{J}(t) = \vec{J}_0 \cos \omega t = \text{Re}[\tilde{J}_0 e^{j\omega t}] \qquad\qquad (2.31)$$

$$\vec{E}(t) = \vec{E} \cos \omega t = \text{Re}[\tilde{E} e^{j\omega t}] \qquad\qquad (2.32)$$

where $\tilde{\tilde{J}}_0$ and $\tilde{\tilde{E}}$ are the amplitudes of the current density and the electric field, respectively, in complex variable. If the induced electric filed is assumed as axially symmetric, and the azmuthual induced electric field can be written as $\tilde{E}_\varphi = E_R + iE_I$ where E_R and E_I are the real and imaginary parts of the induced electric field respectively. The coil current density only exists in the azimuthal direction and can be written as $\tilde{J}_0 = J_R$ where J_R is the real part of the applied current density. For the convenience, all E_R, E_I J_R are in the azimuthal direction, and we do not denote φ in the subsrcipt in later description. By substituting the complex form of $\tilde{E}_\varphi$ and $\tilde{J}_0$ as shown in the above into Equation (2.24) and by comparing the real and imaginary parts on both sides, respectively, we can then obtain the following:

$$\begin{cases} \nabla^2 E_R - \mu_0\omega\sigma_{p,I}E_R + \mu_0\omega\sigma_{p,R}E_I + \dfrac{\omega^2}{c^2}E_R = 0 \\ \nabla^2 E_I - \mu_0\omega\sigma_{p,I}E_I - \mu_0\omega\sigma_{p,R}E_R + \dfrac{\omega^2}{c^2}E_I - \mu_0\omega J_R = 0 \end{cases} \quad \textbf{(2.33)}$$

2.3.2 Power Absorption

The power deposition per volume by the applied RF current only through induced electric field in the azimuthal direction is calculated as [3]

$$P_{abs} = \bar{J}(t)\cdot\bar{E}(t) = \mathrm{Re}\left\{\tilde{J}e^{i\omega t}\right\}\mathrm{Re}\left\{\tilde{E}e^{i\omega t}\right\} = \frac{1}{2}\int \mathrm{Re}\left\{J^*(t)\cdot E(t)\right\}dt$$
$$= \frac{1}{2}\left\{\left(\sigma_{p,R}E_R + \sigma_{p,I}E_I\right)E_R + \left(\sigma_{p,R}E_I - \sigma_{p,I}E_R\right)E_I\right\}$$

$$\textbf{(2.34)}$$

where σ_p is a plasma conductivity as shown in Equation **(2.26)**. In most practical applications, given the specified absorption power, the input coil current density in the simulation is adjusted iteratively such that the calculated absorption power matches the specified value. As the convergence is reached, the corresponding plasma properties will be used to obtain the electron energy distribution in the plasma. The adjusting method of input coil is described in section 2.6 (boundary condition).

2.4 Heat eqution

If the substrate is heating, the heat equation is involved to resolve the background temperature, which will affect the transport of species. The heat equation describes the distribution of heat (or variation in temperature) in a given region over time. For a function *T(r,z)* of cyclindrical spatial variables *(r,z)* and the time variable in a steady state, the heat equation is

$$\nabla \cdot (k\nabla T) = 0$$
$$\Rightarrow \nabla k \cdot \nabla T + k\nabla^2 T = 0 \tag{2.35}$$

where k is thermal conductivity which could be obtained from Chapman-Enskog

theory [27]

$$k = (C_p + 10.3931)2.669 \times 10^{-5}(\mu/M) \tag{2.36}$$

$$= (C_p + 10.3931)2.669 \times 10^{-5} \frac{\sqrt{T}}{\sigma^2 \Omega \sqrt{M}}$$

where C_p is heat capacity which is obtained from thermal properties database of CEA

format, T is gas temperature, σ is Lennard-Jones parameter, Ω is collision integral, and

M is molecular weight. The boundary condition of equation (2.35) is specific thermal

temperature at substrate, and the temperature is 400 K at metal and quartz wall.

2.5 Surface Kinetic Model

In the current study, we have implemented a surface kinetic model considering

silicon dioxide (SiO_2) etching process based on site balance concept at the substrate.

With this, etching products can incorporate into the fluid modeling of CF_4 plasma and

the distribution of etching rate on the substrate can be obtained from the simulation.

Table 8 summarizes the surface reactions of SiO_2 etching and related coefficients

required for modeling [54][55]. In this surface model, fluorine (F), fluorocarbon

radicals (denoted as CF_x), and a surface polymer (P) consisting of clustering molecules

are considered to react with surface sites. A concept of surface "coverage," θ ($0 \leq \theta \leq 1$),

is applied to all these species in the surface layer under effects of ion and radical fluxes

impinging on the substrate. The etching mechanisms considered in the surface model

include: (a) physical sputtering, (b) ion-enhanced etching with F atoms and CF_x

radicals, and (c) thermal etching. The etching process continues as long as θ_P do not

occupied whole surface sites ($\theta_P<1$). The deposition mechanisms considered in the

surface model include: (a) direct ion deposition and (b) "stitching" or "ion-enhanced deposition" of CF_x radicals on the surface. A simultaneous mechanism of ion enhanced etching of polymer with F atoms is also considered. Therefore, the various kinds of surface coverage, including fluorine atom (θ_F), fluorocarbon radicals (θ_{CFx}) and polymer (θ_P), have to be involved in the surface model, which are solved by a set of equations of surface site balance in a steady state. These equations are written as [54]:

$$\frac{d(\theta_F)}{dt} = s_F(1-\theta_{TOT})\Gamma_F - 2\beta_F\theta_F\Gamma_{ION} = 0 \tag{2.37}$$

$$\frac{d(\theta_{CFx})}{dt} = \sum_i s_{CFi}(1-\theta_{TOT})\Gamma_{CFi} - y_c\theta_{CFx}\Gamma_{ION} - \beta_{CFx}\theta_{CFx}\Gamma_{ION} - k_{REC}\theta_{CFx}\Gamma_F = 0 \tag{2.38}$$

$$\frac{d(\theta_P)}{dt} = \sum_i x_i y_{d,i}\Gamma_{ION} + \beta_s\theta_{CFx}\Gamma_{ION} + \beta_s\theta_P\theta_{CFx/P}\Gamma_{ION} - \beta_{F/P}\theta_P\theta_{F/P}\Gamma_{ION} = 0 \tag{2.39}$$

where $\theta_{TOT}=\theta_F+\theta_{CFx}+\theta_P$ is the sum of coverage (i.e. $1-\theta_{TOT}$ is uncovered area). s_F and s_{CFx} are sticking coefficients for F and CF_x on surface SiO_2. β_F, β_{CFx}, β_s and $\beta_{F/P}$ are etching coefficients of ion enhanced chemical etching by F atom, etching coefficient of ion enhanced chemical etching by CF_x, etching coefficient of ion enhanced deposition of radicals, and ion enhanced etching of polymer by F. y_c and $y_{d,i}$ are etching yields for sputtering and direct ion deposition respectively. x_i denotes the ratio of ith ion flux to total ion flux. Moreover, Γ_F, Γ_{ION} and Γ_{CFi} are F atom flux, total ion flux and fluorocarbon flux. Besides, F and CF_x react not only with SiO_2 surface but also with polymer layer. Surface coverages for F and CF_x on polymer surface in a steady state are denoted as $\theta_{F/P}$ and $\theta_{CFx/P}$, respectively, expressed in a similar method [54]:

$$\frac{d(\theta_{F/P})}{dt} = s_{F/P}(1-\theta_{TOT/P})\Gamma_F - \beta_{F/P}\theta_{F/P}\Gamma_{ION} = 0 \tag{2.40}$$

$$\frac{d(\theta_{CFx/P})}{dt} = \sum_i s_{CFi/P}(1-\theta_{TOT/P})\Gamma_{CFi} - y_c\theta_{CFx}\Gamma_{ION} - \beta_{CFx/P}\theta_{CFx/P}\Gamma_{ION} - k_{REC}\theta_{CFx/P}\Gamma_F = 0$$

$$\tag{2.41}$$

where $\theta_{\text{TOT}}=\theta_{\text{F/P}}+\theta_{\text{CFx/P}}$. Because the treatments of site balance for $\theta_{\text{F/P}}$ and $\theta_{\text{CFx/P}}$ on polymer surface are similar to those of θ_{F} and θ_{CFx} on SiO$_2$, they are listed in Table 8 for reference [54][55]. In this study, the surface model is used to estimate etching products and etching rate through calculation of radical and neutral fluxes depleted from SiO$_2$ surface. When incident fluxes of F, CF_x, and ions are determined by fluid model, the surface site coverages can be obtained via solving site balance Equations **(2.39)**-**(2.43)**.

The above coverages are then employed to determine the net fluxes of etching products generated from SiO$_2$ etching into gas phase,. Before etching rate is calculated, the flux of etching yield has to be estimated through [54]

$$\Gamma y_{SiO_2} = \sum_i x_i y_{SP,i} (1-\theta_{TOT})\Gamma_{ION} + \beta_F \theta_F \Gamma_{ION} + \beta_{CFx}\theta_{CFx}\Gamma_{ION} + k_{rec}(1-\theta_{CFx}-\theta_P)\Gamma_F$$

(2.42)

where $y_{SP,i}$ is etching coefficient of physical sputtering. After etching yield is determined, the etching rate could be calculated by

$$\text{Etching rate} = \Gamma y_{SiO_2} / \sigma_{SiO_2}$$

(2.43)

where σ_{SiO_2} is the density of SiO$_2$, and is taken be $2.64 \times 10^{28} m^{-3}$. Since the flux of F is always much larger than those of CF_x and ions, the mechanism of surface reactions must be etching process (i.e. $\theta_P<1$), and the SiO$_2$ deposition yield does not occur in the simulation. In addition, Table 9 summarizes the list of surface reactions at metal walls based on concept of sticking coefficients.

2.6 Boundary Conditions

The boundary conditions used in the current plasma fluid model are summarized as follows:

1. Flux balance for electron:

$$\Gamma_e = \sum \Gamma_+ - \sum \Gamma_- \qquad (2.44)$$

$$n_e = \sum n_+ - \sum n_- \qquad (2.45)$$

2. Continuity equation for ions:

$$\Gamma_i = 0.61 n_i \sqrt{\frac{8kT_e}{M_i}} \qquad (2.46)$$

3. Continuity equation for neutral species:

$$\Gamma_k = \frac{1}{4} n \sqrt{8k_B T_g / \pi M_k} \qquad (2.47)$$

Sticking coefficient at metal wall (Table 9);

Surface reactions at the substrate (Table 8).

4. Electron energy density equation:

$$\Gamma_{Te} = 2T_e \Gamma_e \qquad (2.48)$$

5. Vector wave equation for electromagnetic wave:

$E_\varphi = 0$ on the grounded surfaces and central axis.

6. Electrostatic electric field

Concentrations of electron and ions are zero at all surfaces.

7. Background temperater

$T = $ specific temperature at the substrate.

$T = 400$ at metal wall

$T = \nabla \text{T}$ at gas pump

8. Applied current

The applied current will be modified by a specific power absorption Pow_{set},

and the current is varied through below fomular

$$I(new) = I + I \times factor \times (\frac{Pow_{set} - Pow}{Pow_{set}}) \qquad \textbf{(2.49)}$$

where I is original current, $I(new)$ is modified current, *factor* is 0.01 in this study, Pow is power absorption from Ohmic heating, and Pow_{set} is specific absorbed power.

9. Pumping rate

The pumping rate will be modified by a specific pressure P_{set}, and the pumping rate is varied through below fomular

$$S(new) = S + S \times factor \times (\frac{P_{set} - P}{P_{set}}) \qquad \textbf{(2.50)}$$

where S is unmodified pumping rate, $S(new)$ is modified pumping rate, factor is 0.0001 in this study, P is pressure from sum ot total neutral and charged species, and P_{set} is specific pressure.

2.7 Gas-Phase Reactions of CF$_4$ ICP Source

To properly model gas-phase etching products in a tetrafluoromethane discharge, we have extended the gas-phase reactions of CF$_4$ in a fluid model by adding related reactions of etching reactants, such as oxygen-containing species and tetrafluorosilane species, as compared to the previous study [26]. For a proper description of the gas-phase plasma chemistry related etching products, in addition to CF$_4$ related species, we also take O_2 and SiF_x into account in the model. Table 3 summarizes an overview of various species considered in the simulation along with their corresponding Lennard-Jones parameters and polarizabilities. Total number of species is 32, which include electron, F^+, CF_x^+ (x=1~3), O^+, O_2^+, CO^+, SiF_x^+ (x=1~3), F^-, O^-, F, CF_x (x=1~4), F_2, O, O_2, CO, CO_2, COF, COF_2, Si, SiF_x (x=1~4). Table 4 lists the reactions of electron impact with CF_x (x=1~4) and related gas-phase reactions involving CF_x (x=1~4), in which the above do not consider negative charged fluoride, F^-. In contrast, Table 5 lists

the reactions related to F$^-$. Table 6 summarizes the reactions related to electron-impact and gas-phase reactions for oxygen containing species. Table 7 lists the reactions related to electron-impact and gas-phase reactions of etching products SiF$_x$.

In brief summary, we consider 96 gas-phase reaction channels in the fluid model. Rate constants of electron-impact related reactions are calculated on the basis of energy dependent cross sections using a Boltzmann equation solver named BOLSIG+ [66]. After calculated by the Boltzmann equation solver, the electron mobility, electron diffusivity and rate constants of electron impact related channels are stored as a function of electron temperature. Through these tables, the rates, mobility, and diffusion coefficients can be computed depending on electron temperature calculated by the electron energy density equation. In addition, the rate constants of the remaining gas-phase reactions in Table 4, Table 5, Table 6, and Table 7 are available in the databases like NIST [67] and NIFS [68]. In some cases, since the uncertainties of reaction rates were not obtained completely, some rate parameter were estimated and adjusted to improve agreement between simulations and experiments based on physical understanding of the reaction process.

2.8 Numerical Discretizations and Algorithms

2.8.1 Discretizations of Conservation Equations

In this thesis, we descritize the plasma fluid modeling equations through the use of finite-difference method. By employing the backward Euler scheme for time integration for time-dependent euqaions, the equations in spatial coordinates are discretized using the finite-difference method in cylindrical coordinate system (r,z),

which is denoted as (i,j) in typical grid point. If the quantity (vector) is on the half grid point, we denote it as i±1/2 or j±1/2.

2.8.1.1 Discretizations of Continuity Equations

Since continuity equaiotn for different species are similar, we only present the discretiations for the continuity equation for charged species, Equation **(2.10)**. The resulting discretized equation in cylindrical coordinate system (r, z) can be written as

$$\frac{n_{\alpha(i,j)}^{t+\Delta t} - n_{\alpha(i,j)}^{t}}{\Delta t} + \frac{1}{r_i} \frac{\left(r_i + 0.5\Delta r_i\right)\Gamma_{\alpha(i+\frac{1}{2},j)} - \left(r_i - 0.5\Delta r_i\right)\Gamma_{\alpha,(i-\frac{1}{2},j)}}{\Delta r_i} + \frac{\Gamma_{\alpha(i,j+\frac{1}{2})} - \Gamma_{\alpha(i,z-\frac{1}{2})}}{\Delta z_j} = S_\alpha$$

(2.51)

where r_i is the distance from original point to grid point i, α can be ion or neutral species, Δr_i and Δz_j are the grid size at grid (i,j) in the r- and z-direction, respectively, and S_α is source term at grid point (i,j). In order to solve **(2.51)** in a matrix form, we rearrange the above into the following form:

$$n_{I,(i-1,j)}\left\{ -r_{i-1}\frac{\overline{D_{Ir,i-1}}}{\Delta r_{i-1}} - 0.5 \cdot r_{i-1} \cdot s_I \overline{\mu_{Ir,i-1}\vec{E}_{r,i-1}} \right\}$$

$$n_{I,(i.j-1)}\left\{ -z\frac{\overline{D_{Iz,j-1}}}{\Delta z_{j-1}} - 0.5 \cdot z \cdot s_I \overline{\mu_{Iz,j-1}\vec{E}_{z,j-1}} \right\}$$

$$n_{I,(i,j)}\left\{ \frac{1}{\Delta t} + r_i\frac{\overline{D_{Ir,i}}}{\Delta r_i} + 0.5 \cdot r_i \cdot s_I \overline{\mu_{Ir,i}\vec{E}_{r,i}} + r_{i-1}\frac{\overline{D_{Ir,i-1}}}{\Delta r_{i-1}} - 0.5 \cdot r_{i-1} \cdot s_I \overline{\mu_{Ir,i-1}\vec{E}_{r,i-1}} \right.$$

$$\left. + z\frac{\overline{D_{Iz,j}}}{\Delta z_j} + 0.5 \cdot z \cdot s_I \overline{\mu_{Iz,j}\vec{E}_{z,j}} + z\frac{\overline{D_{Iz,j-1}}}{\Delta z_{j-1}} - 0.5 \cdot z \cdot s_I \overline{\mu_{Iz,j-1}\vec{E}_{z,j-1}} \right\}$$

$$n_{I,(i,j+1)}\left\{ -z\frac{\overline{D_{Iz,j}}}{\Delta z_j} + 0.5 \cdot z \cdot s_I \overline{\mu_{Iz,j}\vec{E}_{z,j}} \right\}$$

$$n_{I,(i+1,j)}\left\{ -r_i\frac{\overline{D_{Ir,i}}}{\Delta r_i} + 0.5 \cdot r_i \cdot s_I \overline{\mu_{Ir,i}\vec{E}_{r,i}} \right\} = \frac{n_I^t}{\Delta t}S_I$$

(2.52)

2.8.1.2 Discretizations of Electron Energy Density Equation

The electron density enegy equation is descritized as

$$\frac{\frac{3}{2}n_{e(i,j)}^{t+\Delta t}T_{e(i,j)}^{t+\Delta t} - \frac{3}{2}n_{e(i,j)}^{t}T_{e(i,j)}^{t}}{\Delta t} + \frac{1}{r_i}\frac{\left(r_i + 0.5\Delta r_i\right)Q_{e(i+\frac{1}{2},j)} - \left(r_i - 0.5\Delta r_i\right)Q_{e(i-\frac{1}{2},j)}}{\Delta r_i} + \frac{Q_{e(i,j+\frac{1}{2})} - Q_{e(i,j-\frac{1}{2})}}{\Delta z_j}$$

$$= -e\vec{\Gamma}_e \cdot \vec{E} - \varepsilon_{loss} + P_{ind}$$

$$(2.53)$$

where T_e is in an unit of eV. In order to solve **(2.53)** in a matrix form, we rearrange the above into the following form:

$$T_{e,i-1}\left\{-r_{-i}\frac{5}{4}\vec{\Gamma}_{e,r-\frac{1}{2}} - r_{-i}\frac{5}{2}\frac{\overline{\left(n_e D_e\right)}_{r,i-1}}{\Delta r_{i-1}}\right\}$$

$$T_{e,j-1}\left\{-z_{zi}\frac{5}{4}\vec{\Gamma}_{e,z-\frac{1}{2}} - z_{zi}\frac{5}{2}\frac{\overline{\left(n_e D_e\right)}_{z,j-1}}{\Delta z_{j-1}}\right\}$$

$$T_{e,(i,j)}\left\{\frac{3n_e}{2\Delta t} + r_{+i}\frac{5}{4}\vec{\Gamma}_{e,r+\frac{1}{2}} + r_{+i}\frac{5}{2}\frac{\overline{\left(n_e D_e\right)}_{r,i}}{\Delta r_i} - r_{-i}\frac{5}{4}\vec{\Gamma}_{e,r-\frac{1}{2}} + r_{-i}\frac{5}{2}\frac{\overline{\left(n_e D_e\right)}_{r,i-1}}{\Delta r_{i-1}}\right.$$

$$\left. + z_{ri}\frac{5}{4}\vec{\Gamma}_{e,z+\frac{1}{2}} + z_{ri}\frac{5}{2}\frac{\overline{\left(n_e D_e\right)}_{z,j}}{\Delta z_j} - z_{zi}\frac{5}{4}\vec{\Gamma}_{e,z-\frac{1}{2}} + z_{zi}\frac{5}{2}\frac{\overline{\left(n_e D_e\right)}_{z,j-1}}{\Delta z_{j-1}}T_{e,j}\right\}$$

$$(2.54)$$

$$T_{e,j+1}\left\{+z_{ri}\frac{5}{4}\vec{\Gamma}_{e,z+\frac{1}{2}} - z_{ri}\frac{5}{2}\frac{\overline{\left(n_e D_e\right)}_{z,j}}{\Delta z_j}\right\}$$

$$T_{e,i+1}\left\{r_{+i}\frac{5}{4}\vec{\Gamma}_{e,r+\frac{1}{2}} - r_{+i}\frac{5}{2}\frac{\overline{\left(n_e D_e\right)}_{r,i}}{\Delta r_i}\right\} = \frac{3n_e T_e}{2\Delta t} - e\vec{\Gamma}_e \cdot \vec{E} - \varepsilon_{loss} + P_{ind}$$

2.8.1.3 Discretizations of Maxwell's Equation

The real and imaginary parts of the vector wave eqution (Equation **(2.33)**) can be discretized, respectively, as

$$\frac{1}{r_i}\frac{E_{\varphi,R(i+1)} - E_{\varphi,R(i-1)}}{\Delta r_{i-1} + \Delta r_i} + \left\{\frac{2E_{\varphi,R(i+1)}}{\Delta r_i\left(\Delta r_{i-1} + \Delta r_i\right)} + \frac{2E_{\varphi,R(i-1)}}{\Delta r_{i-1}\left(\Delta r_{i-1} + \Delta r_i\right)} - \frac{2E_{\varphi,R(i,j)}}{\Delta r_{i-1}\Delta r_i}\right\}$$

$$+ \left\{\frac{2E_{\varphi,R(j+1)}}{\Delta z_j\left(\Delta z_{j-1} + \Delta z_j\right)} + \frac{2E_{\varphi,R(j-1)}}{\Delta z_{j-1}\left(\Delta z_{j-1} + \Delta z_j\right)} - \frac{2E_{\varphi,R(i,j)}}{\Delta z_{j-1}\Delta z_j}\right\}$$

$$- \mu_0\omega\sigma_{p,I}E_{\varphi,R(i,j)} + \mu_0\omega\sigma_{p,R}E_{\varphi,I(i,j)} + \frac{\omega^2}{c^2}E_{\varphi,R(i,j)} = 0$$

$$(2.55)$$

$$\frac{E_{\varphi,I(i+1)} - E_{\varphi,I(i-1)}}{r_i\left(\Delta r_{i-1} + \Delta r_i\right)} + \left\{\frac{2E_{\varphi,I(i+1)}}{\Delta r_i\left(\Delta r_{i-1} + \Delta r_i\right)} + \frac{2E_{\varphi,I(i-1)}}{\Delta r_{i-1}\left(\Delta r_{i-1} + \Delta r_i\right)} - \frac{2E_{\varphi,I(i,j)}}{\Delta r_{i-1}\Delta r_i}\right\}$$

$$+ \left\{\frac{2E_{\varphi,I(j+1)}}{\Delta z_j\left(\Delta z_{j-1} + \Delta z_j\right)} + \frac{2E_{\varphi,I(j-1)}}{\Delta z_{j-1}\left(\Delta z_{j-1} + \Delta z_j\right)} - \frac{2E_{\varphi,I(i,j)}}{\Delta z_{j-1}\Delta z_j}\right\}$$

$$+ \left(-\mu_0\omega\sigma_{p,I} + \frac{\omega^2}{c^2}\right)E_{\varphi,I(i,j)} - \mu_0\omega\sigma_{p,R}E_{\varphi,R(i,j)} = \mu_0\omega J_{fR(i,j)}$$

$$(2.56)$$

The above equations can be rearranged to a matrix form. The resulting real part

is written as

$$\left\{\frac{2}{\Delta r_{i-1}\left(\Delta r_{i-1} + \Delta r_i\right)} - \frac{1}{r_i\left(\Delta r_{i-1} + \Delta r_i\right)}\right\}E_{\varphi,R(i-1)}$$

$$+ \left\{\frac{2}{\Delta z_{j-1}\left(\Delta z_{j-1} + \Delta z_j\right)}\right\}E_{\varphi,R(j-1)}$$

$$+ \left\{-\frac{2}{\Delta r_{i-1}\Delta r_i} - \frac{2}{\Delta z_{j-1}\Delta z_j} - \mu_0\omega\sigma_{p,I} + \frac{\omega^2}{c^2}\right\}E_{\varphi,R(i,j)} \quad (2.57)$$

$$+ \left\{\frac{2}{\Delta z_j\left(\Delta z_{j-1} + \Delta z_j\right)}\right\}E_{\varphi,R(j+1)}$$

$$+ \left\{\frac{1}{r_i\left(\Delta r_{i-1} + \Delta r_i\right)} + \frac{2}{\Delta r_i\left(\Delta r_{i-1} + \Delta r_i\right)}\right\}E_{\varphi,R(i+1)}$$

$$+ \left\{\mu_0\omega\sigma_{p,R}\right\}E_{\varphi,I(i,j)} = 0$$

The resulting imaginary part is written as

$$\left\{ -\frac{1}{r_i\left(\Delta r_{i-1}+\Delta r_i\right)}+\frac{2}{\Delta r_{i-1}\left(\Delta r_{i-1}+\Delta r_i\right)} \right\}E_{\varphi,I(i-1)}$$

$$+\left\{ +\frac{2}{\Delta z_{j-1}\left(\Delta z_{j-1}+\Delta z_j\right)} \right\}E_{\varphi,I(j-1)}$$

$$+\left\{ -\frac{2}{\Delta r_{i-1}\Delta r_i}-\frac{2}{\Delta z_{j-1}\Delta z_j}+\left(-\mu_0\omega\sigma_{p,I}+\frac{\omega^2}{c^2}\right) \right\}E_{\varphi,I(i,j)} \qquad \textbf{(2.58)}$$

$$+\left\{ \frac{2}{\Delta z_j\left(\Delta z_{j-1}+\Delta z_j\right)} \right\}E_{\varphi,I(j+1)}$$

$$+\left\{ \frac{1}{r_i\left(\Delta r_{i-1}+\Delta r_i\right)}+\frac{2}{\Delta r_i\left(\Delta r_{i-1}+\Delta r_i\right)} \right\}E_{\varphi,I(i+1)}$$

$$\left\{ -\mu_0\omega\sigma_{p,R} \right\}E_{\varphi,R(i,j)}$$

$$=\mu_0\omega J_{fR(i,j)}$$

2.8.1.4 Discretizations of Heat Equation

The heat equation (Equation (**2.35**)) is descritized in cylincrical coordinate, which is shown as

$$\frac{\partial k}{\partial r}\frac{\partial T}{\partial r}+\frac{\partial k}{\partial z}\frac{\partial T}{\partial z}+k\left\{ \frac{1}{r}\frac{\partial T}{\partial r}+\frac{\partial^2 T}{\partial r^2}+\frac{\partial^2 T}{\partial z^2} \right\}=0 \qquad \textbf{(2.59)}$$

In order to solve (**2.59**) in a matrix form, we rearrange the above equation into the following

51

$$\left\{-\frac{k_{i+1,j}-k_{i-1,j}}{\left(\Delta r_{i-1}+\Delta r_i\right)^2}-\frac{k_{i,j}}{r_i\left(\Delta r_{i-1}+\Delta r_i\right)}+\frac{k_{i,j}}{0.5\Delta r_{i-1}\left(\Delta r_{i-1}+\Delta r_i\right)}\right\}T_{i-1,j} \qquad (2.60)$$

$$+\left\{-\frac{k_{i,j+1}-k_{i,j-1}}{\left(\Delta z_{j-1}+\Delta z_j\right)^2}+\frac{k_{i,j}}{0.5\Delta z_{j-1}\left(\Delta z_{j-1}+\Delta z_j\right)}\right\}T_{i,j-1}$$

$$+\left\{-\frac{k_{i,j}}{0.5\Delta r_i\Delta r_{i-1}}-\frac{k_{i,j}}{0.5\Delta z_i\Delta z_{i-1}}\right\}T_{i,j}$$

$$+\left\{\frac{k_{i,j+1}-k_{i,j-1}}{\left(\Delta z_{j-1}+\Delta z_j\right)^2}+\frac{k_{i,j}}{0.5\Delta z_j\left(\Delta z_{j-1}+\Delta z_j\right)}\right\}T_{i,j+1}$$

$$+\left\{\frac{k_{i+1,j}-k_{i-1,j}}{\left(\Delta r_{i-1}+\Delta r_i\right)^2}+\frac{k_{i,j}}{r_i\left(\Delta r_{i-1}+\Delta r_i\right)}+\frac{k_{i,j}}{0.5\Delta r_i\left(\Delta r_{i-1}+\Delta r_i\right)}\right\}T_{i+1,j}=0$$

2.8.2 Numerical Algorithms for Solving Discretized Equations

As mentioned earlier, the set of nonlinear coupled partial differential equations, including the Maxwell's equation, the electron energy equation, the continuity equations for neutral species and ions, and the surface kinetic model, is discretized using the finite-difference method to form a linear algebraic system as $\mathbf{Ax}=\mathbf{b}$ at each time step, where $\mathbf{A}$ denotes the matrix representation of a linear operator, $\mathbf{b}$ is the right-hand-side vector, and $\mathbf{x}$ is the solution vector. Since the rate of convergence of iterative Krylov projection methods for particular linear system depends on its spectra, preconditioning is typically required to alter the spectrum and hence accelerates the rate of convergence rate. Thus, we have employed the combination of iterative Krylov subspace method and a preconditioning technique to solve this matrix system [70].

In this study, we have tested two types of Krylov subspace methods, which include generalized minimal residual method (GMRES), and biconjugate gradient method (BCGS). As for the preconditioning, we have tested successive over-relaxation (SOR),

block Jacobi method (BJACOBI), additive Schwarz methods (AMS) and LU decomposition (LU).

2.8.3 Numerical Procedures

The simulation begins by solving the Maxwell's equations to obtain the electromagnetic fields in the azimuthal direction and power deposition from a specified coil current that induces an azimuthal electric field. Through the electron energy density equation, the distribution of electron temperature is then obtained for calculating the electron related transport properties, rate constants, and source/sink through a prepared lookup table. Then, the ion and neutral continuity equations are solved using the most updated plasma properties to obtain the distributions of concentrations ions and neutrals. Accordingly, the electron density is obtained from the quasi-neutrality assumption. Meanwhile, the etching products depleted from SiO_2 etching into gas phase are obtained by solving surface kinetic model (site balance equations). In turn, the effective plasma conductivity is re-calculated using the most updated electron density. All the discretized equations are solved semi-implicitly (with most updated information) and sequentially one after one at each time step. The simulation continues until the steady-state solutions are obtained. In this study, a multi-scale time-marching approach is adopted in this study. For the charged species including electron and ions, we have employed a smaller time step because the electron is very light. In contrast, we have employed a much larger time step for those abundant neutral species to save the computational required for reaching the quasi-steady state of the discharge.

2.8.4 Implementation of Parallel Computation

In the process of simulation, the resulting algebraic linear system of each equation is solved independently by the Krylov subspace method with or without parallel preconditioner provided by PETSc library [72] through domain decomposition technique implemented by using MPI [73]. Among the iterative linear solvers of Krylov subspace, we have employed the GMRES and BCGS to solve the linear systems obtained by discretization since it has been shown to be the most robust linear matrix solver for most of the cases. Besides, in the preconditioning we test the performance of two sub-domain solvers such as LU (direct) and incomplete LU (ILU; iterative) factorizations. For preconditioners, we have selected the popular preconditioners such as Black Jacobi, successive over-relaxation (SOR), Additive Schwarz Preconditioners (ASM) and LU. The detail parallel performance will be presente using combination of Krylov subspace method and preconditioner later.
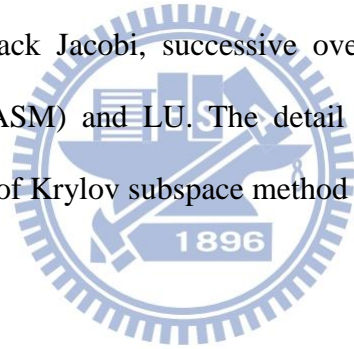
CHAPTER 3
VALIDATION
AND
PARALLEL PERFORMANCE

In this chapter, we validate our developed code by comparing with previous simulation and experimental results of a typical cyclindrical ICP chamber. After validation, parallel performance of the developed fluid code for simulating an ICP source is presented in turn.

3.1 Validation

In this section, we presents validation of the developed fluid modeling code by comparing with previous simulation and experiment of Fukumoto *et al.* [26][74] in a typical cylindrical ICP chamber. Figure 8 shows the schematic diagram of the ICP reactor under consideration. The plasma reactor is 30 cm in diameter, and 9 cm in height. The dielectric window is at the top of the chamber with five turns of coil right above it, and the wafer is 20 cm in diameter at the bottom of the chamber. Table 10 summarized the corresponding test conditions. The major operating conditions consist of: a frequency of 13.56 MHz of power source, a gas pressure of 20 mTorr, an ICP input power of 250 W, and a gas flow rate of 200 sccm. In addition, because of the simple geometry of the ICP chamber, an exact solution of Maxwell's equation based on the Biot-Savart's law was used as the boundary condition at the plasma-dielectric window interface in [26].

Figure 9 gives the prsent simulation results of chemical compositions of typical charged species averaged over the entire region of the ICP reactor along with the simulation results of Fukumoto *et al.* [26] for comparison purpose. In addition, Figure 10 gives their results of mass spectra measurements [74]. The results show that the trend and the quantity of the predicted concentrations of CF_x^+ (x=1~3) agree well with the experimental results [74], in which all show consistently the order of ion concentration as $CF_x^+ > CF_x^+ > CF_x^+$. Figure 10-15 show a series of the present simulation results of several important plasma properties along with previous simulation results of Fukumoto *et al.* [26]. These plasma properties include feedstock CF_4 density, electron density, electron temperature, F^- density, CF_3^+ density, and chemical compositions of ion species. Again, results showthat the present simulations agree reasonably well with those of Fukumoto *et al.* [26]. Thus, we conclude that the current fluid modeling code is valid at least under the similar conditions as simulated and measured by Fukumoto *et al.* [26][74].

3.2 Parallel Performance

Table 11 summarizes the computational time of the present parallel fluid modeling code for the CF4 ICP with a grid size of 122×179 with 32 species, which leads to about 700,000 unknowns in total. Two thousand time steps were run throughout the tests using the Generalized Minimal Residual Method (GMRES) as the linear equation solver in combination with various preconditioning techniques, including the Additive Swartz Method (ASM), block Jacobi, and Successive Over Relaxation (SOR), on an IBM-1350 clusters at NCHC (National Center of High-Performance Computing) of Taiwan. Note that the IBM-1350 consists of 2,048

cores in total with 4 cores per node, in which Intel X5450 Processor 3.0 GHz Quad core of CPU with 16 GB of RAM is used per node.

Figure 16 shows the corresponding data of parallel performance tests as those summarized in Table 11. The results indicate that the combination of GMRES and block Jacobi (or ASM) using iLU as the sub-domain solver gives the best performance, and this combination is scalable for up to 26 processors for the problem size of 122×179 with 32 species. However, because there are 4 cores in a node of IBM-1350 with a restricting memory, the performance is not as good as the ideal value using 4 processors. In addition, we do not show the cases that combine subdomain solver LU for preconditioner with GMRES because this combination costs more than ILU due to its large grain size in the current test case with fewer numbers of processors. In brief summary, we can reduce greatly runtime at least 10-20 times with the developed fluid modeling code for studying very complex plasma physics and chemistry of in an ICP chamber.
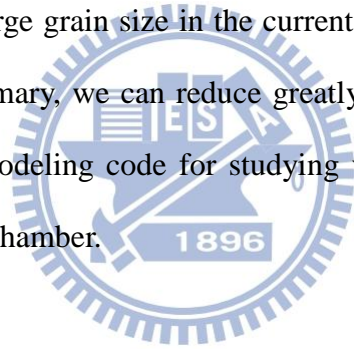
CHAPTER 4
RESULTS AND DISSCUSION

In this chapter, we employ our validated fluid model to study CF_4 discharge in GECRC (section 4.1) and in dome-shaped reactor (section 4.2). Then, we employ developed fluid model to investigate the etching rate, coverage, and fluxes on the substrate in different geometries of ICP reactors: t typical reactor with planar (top) coils, typical reactor with cylindrical (side) coils, and dome-shaped reactors, which is described in the section 4.3.

4.1 CF_4 Discharge in Gaseous Electronics Conference Reference Cell (GECRC)
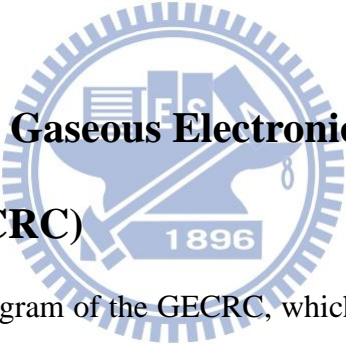
Figure 18 shows the diagram of the GECRC, which is applied for etching SiO_2. There are four turns of coil insulated from the plasma by a quartz window (1.2 cm in thickness and 8 cm in radius), which are driven by a current with a radio frequency (RF) of 13.56 MHz that induces electric field heating in the azimuthal direction. A wafer substrate is located at the central bottom of the reactor. A gas inlet ring for feedstock gas, CF_4, is located at the outer top of the chamber, and the pumping port is located at the outer bottom of the chamber.

The test conditions for CF_4 ICP discharge simulation in GECRC include a gas pressure of 30 mTorr, a CF_4 flow rate of 150 sccm, and a deposited power of 150 W. Several grid convergence tests show that a grid of 66×113 points suffices. The temperatures of the ion and the neutral species are assumed to be constant at 0.026 eV

and 400 K, respectively. The ion bombardment energy is set at 100 eV at the substrate

boundary and 20 eV on the quartz windows.

4.1.1 Spatial Profiles

In this section, we present the distributed profiles of species in CF$_4$ GECRC

discharge. The results are compared with the available experimental data. In the

discussion below, the "core region" and the "edge region" refer to the central and the

edge space, respectively, between the quartz window and the substrate. The "outer

region" refers to the cylindrical space surrounding the parallel plates.

4.1.1.1 Induced Electric Field, Power Absorption and Electron Temperature

Figures 19(a) and 19(b) show the real and the imaginary parts of the induced

electric field in the azimuthal direction, respectively. In addition, Figure 19(c) shows

the power deposition through Ohmic heating of electrons. The real part of the electric

field caused by plasma shows a maximum intensity of approximately 50 V/m in the

core region, where the electron temperature is high. The imaginary part of the induced

electric field caused by the coil current shows a maximum value of approximately

1,500 V/m near the coils and approximately 500 V/m in the gas phase, and it decays

rapidly by an order of magnitude within several centimeters into the high density

plasma, as expected. The total induced electric field is obtained from the magnitude of

the complex induced electric field, which is given by $\left| \tilde{E} \right| = \sqrt{E_{\mathrm{Re}}^2 + E_{\mathrm{Im}}^2}$, which indicates

that the total electric field induced by the coil current is dominant, but the electric filed

induced by plasma can be ignored when considering the contribution of the region

10~20% away from the core region. Therefore, absorption of inductive power is deposited mainly by the imaginary part of the induced electric field within a few centimeters of the dielectric roof. In this case, the plasma conductivity reaches its maximum value in the bulk plasma and decays toward the quartz, while the electric filed reaches its maximum value at the dielectric and decays towards the plasma. However, the power deposition of the plasma is stronger than the square of the imaginary part of the electric field. Therefore, the peak power deposition is approximately 1.5 W at 1 cm below the quartz, and the power deposition becomes 0.2 W away from the quartz and toward the plasma bulk at a height of 2.5 cm. Figure 19(d) illustrates the contours of the electron temperature, which follow a toroidal shape from the quartz to the core region, corresponding to the power absorption of plasma. The electron temperature is highest near the coils in the core region, where the power deposition is the highest. Although the power peaks in the confined region near the dielectric, electron thermal conduction at the low operating pressure helps to heat the whole plasma. The electron is cooled in the outer region, due to either the lower electron thermal conductivity or the higher collision frequency.

4.1.1.2 Production Rate

Figure 20(a) illustrates the profile of the feeding gas CF_4, which shows the gradient profile from the gas inlet to the gas outlet, and the feeding gas is mostly consumed by electron collisions and pumping outlet in the reactor. While the electron temperature and the feeding background gas CF_4 are determined, the reaction rate for production and destruction of each species are specified to influence the species distributions during computation. Therefore, the absolute reaction rates are studied to obtain information on the absolute importance of a reaction, which tells both the

important process and its importance level. In the following, we present the absolute reaction concentration rates (i.e., concentration per second) of the most important reactions in steady state, which are the product of the reaction rate and the reactant concentrations in $s^{-1}m^{-3}$. Figure 20(b) presents the production rate of the momentum transfer reaction, where the electrons collide with the background feedstock gas CF_4. Obviously, the highest frequencies of electron collision occur in two regions: the core region, where electron has a high concentration, and the gas inlet, where CF_4 has a relatively high concentration. Figure 21(a), Figure 21(b) and Figure 21(c) show the relative contributions of dissociative ionization, which are significant production of electron and charge ions. In Figure 21(a), it can be observed that the dissociative ionization that dissociates CF_4 contributes for 90% in generating electron and CF_3^+ because its threshold energy (14.8 eV) is lower than those in the reaction channels to produce CF_2^+ (20.8 eV) and CF^+ (23.9 eV). Although dissociative ionizations to produce CF_2^+ and CF^+ are not dominant reaction processes in CF_4 discharge, they have a significant influence on the production of F in the core region, as shown in Figures 21(b) and 21(c). The production rate of CF_x (x=1~3) from dissociating CF_4 is shown in Figures 21(d), 21(e) and 21(f). The production of CF_x (x=1~3) decreases with decreasing x because their dissociative thresholds increase with decreasing x. In Figure 21(d), CF_3 is completely governed by the electron impact dissociation from CF_4 because it has the lowest threshold energy among the CF_x, which has threshold energies of 5.67 eV (CF_3), 9.32 eV (CF_2) and 14.7 eV (CF). The dissociations of CF_4 that generate CF and CF_2 provide relatively lower productions than the dissociation of CF_4 that generates CF_3. The productions of F^- are shown in Figures 22(a), 22(b), 22(c) and 22(d), which are the dissociative attachment of CF_4, CF_3, CF_2 and F_2, respectively. We see that dissociative attachment of CF_4 clearly dominates the production of F^- in the

discharge. This type of reaction boosts up the production of F^- and the destruction of electron, and F^- shows high concentration in the outer region near gas inlet due to the threshold energy of attachment is relatively low.

4.1.1.3 Electron and Negative Charge Ions

The concentrations of negatively charged species like electron and F^- were illustrated in Figures 23(a) and 23(b) respectively. The electron density peaks at 2.5×10^{17} $1/m^3$ at the center of the core region, where electrons are produced in high quantity by the relative ionized reactions with high electron temperature (F01~F10). Most electrons are lost by diffusion into the chamber walls, and a small amount of electron is lost by dissociative attachment to CF_3 and CF_4 to form negative ions F^- (F01~F03). The static electric fields push the electrons toward the center, causing the electron density to decrease. The predicted high concentration of F^- is 4×10^{16} m^{-3} in the simulation. The profile and quantity of electron and F^- are reasonably consistent with the results measured by Rao $et\ al.$[48]. F^- ions are mainly generated from two reaction paths. One path is dissociative attachment to the feedstock gas CF_4, and the other is dissociative attachment to CF_3, which were dissociated from CF_4 near the gas inlet because it has a lower threshold energy than the other reaction paths. Because F^- is lost significantly via ion recombination, its density is lower in the core region, where CF_3^+ has maximum value, than at the gas inlet. For the other negative ion O^-, the main source of O^- is dissociative electron attachment to O_2 (Ox18 and Ox19), and it presents the largest concentration in the core region. However, this ion is a minor negative charge species, due to its low concentration of 10^{13} m^{-3}, and we do not show its contour here. All negative ions are related to attachment and recombination of negative and positive charges.

4.1.1.4 Positive Ions

Figure 24 shows the distributing profiles of (a) F^+, (b) CF^+, (c) CF_2^+, and (d) CF_3^+. The concentrations of CF_x^+ (x=0~3) peak at the core region due to electron relating ionization from the feedstock gas CF_4 (F01~F10). The comparison between CF_x^+ gives $CF_3^+(\sim2x10^{17}\,m^{-3}) > CF_2^+(\sim4x10^{16}\,m^{-3}) > CF^+(\sim1x10^{16}\,m^{-3}) > F^+(\sim1x10^{14}\,m^{-3})$, which was observed by some experiments [42][48]. The phenomenon is consistent with the threshold energy of electron-impact dissociative ionization reacting to the feedstock gas CF_4: 23.9 (CF^+) > 20.8 (CF_2^+) > 14.8 (CF^+). Moreover, the CF_3^+ concentration peaks not only at the core region but also at the outer region near the gas inlet because of its low threshold energy of dissociative ionization. Figure 25 shows the oxygen-containing charged species: (a) O^+, (b) O_2^+ and (c) CO^+, and Figure 26 shows the silicon-contain charge species: (a) SiF^+, (b) SiF_2^+ and (c) SiF_3^+, which are produced from volatile oxygen-containing and silicon-contain neutral species liberated in the etching process. O^+ and O_2^+ are generated via ionization of their mother gases O and O_2 (Ox01, Ox04, Ox19, Ox20 and Ox21). CO^+ is the product of ionized CO, which is produced from the gas phase of COF and COF_2 (Ox28). SiF_x^+ (x=1~3) are products of dissociative ionization from their mother gases SiF_x (SF01~SF06), and they were restricted in the central region by the electric field of ambipolar diffusion. The concentration of SiF_3^+ is higher than those of SiF^+ and SiF_2^+ because the threshold energy of SiF_3^+ is lower than those of SiF^+ and SiF_2^+.

4.1.1.5 Neutral and Radical Species

The contours of F and CF_x (1~3) were shown in Figure 27. These contours are dominant neutral species to etch SiO_2, and they have relatively high concentrations, which are only less than the feedstock gas concentration. Additionally, the threshold energy and the rate coefficients of the dissociated reactions strongly influence the distributions of these radical species, and the threshold energy of dissociating feedstock gas CF_4 by electron is $14.7 \, eV(CF) > 9.32 \, eV(CF_2) > 5.67 \, eV(CF_3)$. Neutral F atoms are produced principally through electron-impact dissociation reactions of the feedstock CF_4 (F11~F13) in the core region, where the electron density and electron temperature are relatively high. Because a higher threshold energy of reaction is necessary to dissociate the feedstock CF_4 to form CF or CF_2, the distribution peaks in the region of high electron temperature, i.e., in the core region. Because the necessary threshold energy to dissociate CF_4 to generate fragment CF_3 is lower than those to produce CF and CF_2, the concentration of CF_3 is high in both the core region and the outer region near the gas inlet.

When the reactive radicals CF_x (0~3) and the reactive ions approach the SiO_2 layers, including the substrate and the dielectric windows, the etching products are computed to produce through the surface model. Such etching products as O, O_2, COF, COF_2 and CO are liberated into the plasma as the reactive radicals bombard. Once these

etching products merge into the gas, the properties of the plasma will change, due to the impact of electrons on these etching products. The following discussion will include O, O_2, COF, COF_2 and CO, which spill from the etching processes of SiO_2, and their gas-phase products, such as O(1D), O_2(a) and CO_2, which are generated from electron-impact and gas-phase reactions. First, Figure 28(b) gives the distribution of O_2, which has a strong downhill-like gradient from the core region toward the edge region on the dielectric and the substrate surface. O_2 is mainly produced through the surface mechanisms of ion-enhance chemical etching by F (S3) and ion-enhanced chemical sputtering (S4), leading to a high F surface coverage, which is discussed in next section. O_2 is lost via electron-impact reactions (Ox10, Ox16 and Ox17), which produce considerable quantities of O, O(1D) and O_2(a). The profile of O is given in Figure 28(a). The maximum value of O concentration in the central core region occurs due to a high dissociation of O_2. Although O is liberated from physical sputtering (S1), it also recombines to form O_2 on the substrate surface (W15). Figures 28(c) and 28(d) show the profiles of O(1D) and O_2(a), which are excited species of O and O_2 (Ox02, Ox10), and they follow the distributions of O and O_2 struck by electron to form excitation reactions depending on the electron. Meanwhile, the distributions of carbonous oxide products from the etching substrate, such as COF, COF_2, CO and CO_2, are given in Figure 29. COF is mainly produced in the surface reactions with fluorocarbon radicals,

but it is lost via collision with such radicals as CF_x. While a portion of COF_2 is produced on the substrate via etching, most of it is produced in the reaction between CF_3 and O near the gas inlet region, where the concentration of CF_3 is high. CO and CO_2 are mainly distributed in the core region, where the gas reaction of COF_x and CF_x (Ox31, Ox32, Ox34, Ox36, Ox38 and Ox39) and the surface reactions (S7) occur.

Figures 30(a)-(e) show the distributions of SiF_x (x=0~4), which have a strong downhill-like gradient from the central core region to the substrate edge region because these species escape through the etching processes, depending on the fluxes of radicals and ions transported to the SiO_2 layer. SiF_x (x=0~4) are also produced on the SiO_2 dielectric windows and on the substrate surface as x increases. SiF_4 is the dominant etching product while etching SiO_2 in CF_4 discharge, which was also observed in many experiments [37][45][45]. Although the volatile SiF_x (x=0~3) strongly depend on the surface coverage of CF_x (θ_{CFx}), the volatile SiF_4 strongly depends on the surface coverage of F (θ_F). When θ_F is the dominant coverage on either the substrate or the dielectric windows, θ_{CFx} only covers the substrate because the low ion energy is presented at the dielectric windows. The distribution of F_2 in Figure 30(f) shows a large concentration near the gas inlet because F_2 molecules mainly come from the detached recombination of F^- and F (FN11), which are rich near the gas inlet, and it is assumed that F_2 would not interact with wall, due to its full chemical bond.

4.1.2 Chemical Ingredients

The chemical ingredients of the charged and the neutral species averaged over the core region of the reactor were shown in Figure 31 and Figure 32 respectively. The positive ion CF_3^+ is the obvious dominant charge with a concentration of $\sim 10^{17}$ $1/m^3$. Regarding the significant charges CF_x^+, the trend of $CF_3^+ > CF_2^+ > CF^+$ is observed in the simulation because of their threshold energies to fragment CF_4, which is consistent with the experiments [48][49][68]. The concentration of the negative ion F^- in simulation of CF_4 discharge is about 10^{16} $1/m^3$, and it is comparable to the concentration of electron in our simulation, which was also measured by Rao $et\ al.$ [48]. Moreover, Because CF_4 is fed from the gas inlet, it is the most numerous species as the background gas. F is the dominant radical species with a concentration of 10^{20} $1/m^3$, which explains the large value of fluorine coverage. At a given pressure, the number density of CF_x weakly increases as a function of the increasing x (x=1~3), as it has been observed in the APMS measurement [42] and FTIR measurement [50]. The COF_2 concentration is approximately equal to the SiF_4 concentration because they are assumed not to react with the wall, which was observed in the FTIR measurement [45][47].

4.1.3 Surface Coverage

Figure 33 shows the surface coverage as a function of r direction on the substrate. The fluorine surface coverage is the dominating coverage in our simulation because the fluorine atom fluxes are much larger than the fluorocarbon radical fluxes. However, because the low ion energy is assumed at 100 eV in the model, deposition of polymer surface coverage occurs when ion-enhanced deposition becomes more important. As a result, a balance between the etching process and the polymer deposition will determine the amount of coverage. It can be observed that etching mainly occurs in the region where fluorine fluxes have to be larger than or equal to the magnitude of fluorocarbon radical fluxes, i.e., $\Gamma_F \geq \Gamma_{CF_x}$, and ICPs always generate high fluorine fluxes [54]. The ratio of averaged θ_F : θ_P : $(1 - \theta_F - \theta_{CFx} - \theta_P)$ in our result is approximately 0.6: 0.15: 0.2. Thus, the etching process is mainly controlled by fluorine surface coverage, which makes the etching products almost entirely generated from fluorine surface coverage.

4.1.4 Etching Rate and Fluxes to Substrate

Figure 34 shows the fluxes of the ion CF_x^+, the fluxes of the radical CF_x and the etching rate, which has absolute values that are plotted as a function of the radial direction on substrate. The fluxes decrease smoothly toward the edge, as expected due to the decreased power absorption and static electric field, which has patterns that are consistent with the distributing profiles of the respective species. Obviously, the composition of fluxes to the substrate are 90% F atoms, 9% CF_x radicals, and 1% CF_x^+ ions overall. In other words, the flux ratio of fluorine atom to ions is approximately 100, and the flux ratio of fluorocarbon radicals to ions is approximately 10. Therefore, the

fluorine fluxes always dominate the etching process because the fluorine fluxes are higher than the fluorocarbon radical fluxes. However, when power is given, the predicted etch rate is between hundreds to a thousand nm per minute, which is reasonable compared to the experiment [50][54], and this rate decreases gradually near the edge of the substrate because the fluxes decrease radially.

4.2 CF$_4$ Discharge in a Dome-Shaped ICP Reactor

Figure 35 shows the diagram of the dome-shaped ICP reactor. The dome-shaped chamber includes a gas inlet ring through which a reaction gas (CF$_4$) is supplied, a vacuum pump for maintaining the inside of the chamber to be vacuum and exhausting the reaction gas after completing the reaction, and a gas outlet. A gas inlet ring is located at the central rim of the chamber, and the pumping port is located between inner substrate and the chamber wall. The dome-shaped roof is assumed a half sphere with radius of 20 cm. Six turns of antenna coil are insulated from the plasma by a dome-shaped roof of quartz window (2 cm in thickness), which are driven by a current with a radio frequency (RF) of 13.56 MHz that induces electric field heating in the azimuthal direction. A 12-inch wafer substrate is located at the central bottom of the reactor.

The test conditions for CF$_4$ ICP discharge simulation in GECRC include a gas pressure of 20 mTorr, a CF$_4$ flow rate of 230 sccm, and a deposited power of 200 W. The temperatures of the ion and the neutral species are assumed to be constant at 0.026 eV and 400 K, respectively. The ion bombardment energy is set at 100 eV at the substrate boundary. A grid of 221 × 351 points is used to test, in which each length of grids is 1 mm in r-direction and 1 mm in z-direction in this simulation. This grid size leads to about a total 2.5 million unknowns, and has to perform via parallel computing to reduce running time whit in one day. Because no experimental data is available, we could not compare our results to other's experiment but the results are acceptable through comparing with previous results from GECRC and typical reactor. In the following sections, these results are obtained in dome-shaped ICP with above condition, which is not mentioned again.

4.2.1 Spatial Profiles

In this section, we present the distributed profiles of species in CF$_4$ dome-shaped inductively coupled discharge. The discussions of results follow like discussions of GECRC discharge but of dome-shaped reactor.

4.2.1.1 Induced Electric Field, Power Absorption and Electron Temperature

Figures 36(a) and 36(b) show the real and the imaginary parts of the induced electric field in the azimuthal direction, respectively. In addition, Figure 36(c) shows the power deposition through Ohmic heating of electrons. The real part of the electric field caused by plasma shows a maximum intensity of approximately 20 V/m in the core region, where the electron temperature is high. The imaginary part of the induced electric field caused by the coil current shows a maximum value of approximately 500 V/m near the coils and approximately 300 V/m in the gas phase, and it decays rapidly by an order of magnitude within several centimeters into the high density plasma, as expected. The total induced electric field is obtained from the magnitude of the complex induced electric field, which is given by $\left| \tilde{E} \right| = \sqrt{E_{\mathrm{Re}}^2 + E_{\mathrm{Im}}^2}$, which indicates that the total electric field induced by the coil current is dominant, but the electric filed induced by plasma can be ignored when considering the contribution of the region ~10% in the discharge region. This contribution is not as high as in GECRC because the size of dome-shaped reactor is larger than GECRC. Therefore, absorption of inductive power is deposited also mainly by the imaginary part of the induced electric field within a few centimeters of the dielectric roof in not only GECRC bus also dome-shaped reactor. In dome-shaped reactor, the plasma conductivity also reaches its maximum

value in the bulk plasma and decays toward the quartz, while the electric filed reaches its maximum value at the dielectric and decays towards the plasma. The peak power deposition is approximately 1.5 W at 1 cm below the dome-shaped quartz, and the power deposition becomes 0.2 W toward the discharge in the central region. Figure 36(d) illustrates the contours of the electron temperature corresponding to the power absorption of plasma. The electron temperature is highest near the coils, where the power deposition is the highest. Although the power peaks in the confined region near the dielectric, electron thermal conduction at the low operating pressure helps to heat the whole plasma. The electron is cooled in the outer region, due to either the lower electron thermal conductivity or the higher collision frequency.

4.2.1.2 Production Rate

The importance of production rate has been mentioned in section 4.1.1.2. Here, we first present the profile of background feeding gas CF_4 in Figure 37(a), which strong determine the production rate and plasma property. The figure shows the gradient profile from the gas inlet to the gas outlet, and the feeding gas is mostly consumed by electron collisions in the central discharge region and pumping outlet in the bottom. In the following, we present the absolute reaction concentration rates of the more important reactions in steady state. Figure 37(b) presents the production rate of the momentum transfer reaction, where the electrons collide with the background feedstock gas CF_4. Obviously, the highest frequencies of electron collision occur in the central discharge region, where electron has a high concentration and relatively high reaction rate. Figure 38(a), Figure 38(b) and Figure 38(c) show the relative contributions of dissociative ionization, which are significant production of electron and charge ions. In Figure 38(a), it can be observed that the dissociative ionization that

dissociates CF_4 contributes for 90% in generating electron and CF_3^+ because its threshold energy (14.8 eV) is lower than those in the reaction channels to produce CF_2^+ (20.8 eV) and CF^+ (23.9 eV). Although dissociative ionizations to produce CF_2^+ and CF^+ are not dominant reaction processes in CF_4 discharge, they have a significant influence on the production of F in the core region, as shown in Figures 38(b) and 38(c). The production rate of generating CF_x (x=1~3) from dissociating CF_4 is shown in Figures 38(d), 38(e) and 38(f). The production of CF_x (x=1~3) decreases with decreasing x because their dissociative thresholds increase with decreasing x. In Figure 38(d), CF_3 is completely governed by the electron impact dissociation from CF_4 because it has the lowest threshold energy among the CF_x, which has threshold energies of 5.67 eV (CF_3), 9.32 eV (CF_2) and 14.7 eV (CF). The dissociations of CF_4 that generate CF and CF_2 provide relatively lower productions than the dissociation of CF_4 that generates CF_3. The productions of F^- are shown in Figures 39(a), 39(b), 39(c) and 39(d), which are the dissociative attachment of CF_4, CF_3, CF_2 and F_2, respectively. We see that dissociative attachment of CF_4 clearly dominates the production of F^- in the discharge. This type of reaction boosts up the production of F^- and the destruction of electron, and F^- shows high concentration in the region of gas inlet where the background feeding gas is more because the threshold energy of attachment is relatively low. Figures 40(a) and 40(b) give the production rate of O and O_2 ionization. Figure 40(c) give dissociation of O_2 to generate O, and Figure 40(d) give excitation of O_2 to generate excimer O_2(a). Figure 40(a) indicates the maximum production in the central region where electron and oxygen atom are high concentration. Figure 40(b), 40(c) and 40(d) indicate that the high production is near the substrate because O_2 is abundant etching product from F coverage. Otherwise, the relative low production

rate at central region near roof where O_2 is relative low density is shown in these figures.

4.2.1.3 Electron and Negative Charge Ions

The concentrations of negatively charged species (e^-, F^- and O^-) were respectively illustrated in Figures 41(a), 41(b), and 41(c). Figure 41(a) indicates that the electron density peaks at 1.3×10^{17} $1/m^3$ at the central region of chamber, where electrons are produced in high quantity by the relative ionized reactions with high electron temperature (F01~F10), and their relating production rate were described above. Most electrons are lost by diffusion into the chamber walls, and a small amount of electron is lost by dissociative attachment to CF_3 and CF_4 to form negative ions F^- (FN01~FN03). The static electric fields push the electrons toward the center, causing the electron density like onion-shaped gradient from center to wall. Figure 41(b) indicates that the predicted high concentration of F^- is 1.1×10^{16} m^{-3} in the simulation. F^- ions are mainly generated from two reaction paths. One path is dissociative attachment to the feedstock gas CF_4, and the other is dissociative attachment to CF_3, which were dissociated from CF_4 near the gas inlet because it has a lower threshold energy than the other reaction paths. Because F^- is lost significantly via ion recombination, its density is lower in the central region, where CF_3^+ has maximum value, than at the gas inlet. For the other negative ion O^-, the main source of O^- is dissociative electron attachment to O_2 (Ox18 and Ox19), and it presents the largest concentration in the core region. However, O^- is a minor negative charge species, due to its low concentration of 10^{12} m^{-3}, which is shown as Figure 41(c). Here, all negative ions are related to attachment and recombination of negative and positive charges.

4.2.1.4 Positive Ions

Figure 42 shows the distributing profiles of (a) F^+, (b) CF^+, (c) CF_2^+, and (d) CF_3^+. The concentrations of CF_x^+ (x=0~3) peak at the central reactor due to electron relating ionization from the feedstock gas CF_4 (F01~F10). The comparison between CF_x^+ gives $CF_3^+(\sim9 \times 10^{16}\,m^{-3}) > CF_2^+(\sim3 \times 10^{16}\,m^{-3}) > CF^+(\sim2 \times 10^{16}\,m^{-3}) > F^+(\sim1 \times 10^{13}\,m^{-3})$, which is as same as simulation in GECRC. The phenomenon is consistent with the threshold energy of electron-impact dissociative ionization reacting to the feedstock gas CF_4: 23.9 (CF^+) > 20.8 (CF_2^+) > 14.8 (CF_3^+). All of these ion species have profiles of onion-shaped gradient.

Figure 43 shows the oxygen-containing charged species: (a) O^+, (b) O_2^+ and (c) CO^+, and Figure 44 shows the silicon-contain charge species: (a) SiF^+, (b) SiF_2^+ and (c) SiF_3^+, which are produced from ionization of volatile oxygen-containing and silicon-contain neutral species liberated in the etching process. These species are restricted in the central region and formed gradient in shape of onion by the electric field of ambipolar diffusion. However, the species of O_2^+ and SiF^+ shows maximum gradient near the substrate depending on their relating mother gases and production rate. O^+ and O_2^+ are generated via ionization of their mother gases O and O_2 (Ox01, Ox04, Ox19, Ox20 and Ox21), which was discussed in section 4.2.1.2, and their profiles follow their production reaction paths shown in Figures 40(a) and 40(b). CO^+ is the product of ionized CO, which is produced from the dissociation of gas phase of COF and COF_2 (Ox28). SiF_x^+ (x=1~3) are products of dissociative ionization from their mother gases SiF_x (SF01~SF06). The concentration of SiF_3^+ is higher than those of SiF^+ and SiF_2^+ because the threshold energy of SiF_3^+ is lower than those of SiF^+ and SiF_2^+.

4.2.1.5 Neutral and Radical Species

Figure 45 shows the contours of (a) F and (b)(c)(d) CF_x (x=1~3). These contours are dominant reactive species to etch SiO_2, and they have relatively high concentrations, which are only less than the feedstock gas concentration. These reactive species also have onion gradient because of electron gradient and related production rate, which means the threshold energy and the rate coefficients of the dissociated reactions strongly influence the distributions of these radical species, and the threshold energy of dissociating feedstock gas CF_4 by electron is 14.7 eV(CF) > 9.32 eV(CF_2) > 5.67 eV(CF_3). Additionally, F is rich comparing with other reactive species, because F atoms are produced principally through electron-impact dissociation reactions of the feedstock CF_4 (F11~F13) in the central reactor, where the electron density is relatively high. CF_3 shows relative rich because the necessary threshold energy to dissociate CF_4 to generate fragment CF_3 is lower than those to produce CF and CF_2.

When the reactive radicals CF_x (0~3) and the reactive ions approach the SiO_2 layers, including the substrate and the dielectric windows, the etching products are computed to produce through the surface model. Such etching products as O, O_2, COF, COF_2 and CO are liberated into the plasma as the reactive radicals bombard. Once these etching products merge into the gas, the properties of the plasma will change, due to the impact of electrons on these etching products. The following discussion will include O, O_2, COF, COF_2 and CO, which spill from the etching processes of SiO_2, and their gas-phase products, such as O(1D), O_2(a) and CO_2, which are generated from electron-impact and gas-phase reactions. First, Figure 46(b) gives the distribution of O_2, which has a strong downhill-like gradient from the core region toward the edge region on the dielectric and the substrate surface. O_2 is mainly produced through the surface mechanisms of ion-enhance chemical etching by F (S3) and ion-enhanced chemical

sputtering (S4), leading to a high F surface coverage, which is discussed in next section. O_2 is lost via electron-impact reactions (Ox10, Ox16 and Ox17), which produce considerable quantities of O, O(1D) and O_2(a). The profile of O is given in Figure 46(a). The maximum value of O concentration occurs in the central chamber near substrate due to a high dissociation of O_2. Although O is liberated from physical sputtering (S1), it also recombines to form O_2 on the substrate surface (W15). Figures 46(c) and 46(d) show the profiles of O(1D) and O_2(a), which are excited species of O and O_2 (Ox02, Ox10), and they follow the distributions of O and O_2 struck by electron to form excitation reactions depending on the electron. Meanwhile, the distributions of carbonous oxide products from the etching substrate, such as COF, COF_2, CO and CO_2, are given in Figure 47. COF is mainly produced in the surface reactions with fluorocarbon radicals, but it is lost via collision with such radicals as CF_x. While a portion of COF_2 is produced on the substrate via etching, most of it is produced in the reaction between CF_3 and O near the gas inlet region, where the concentration of CF_3 is high. Because COF_2 does not react with metal wall, they show rich near the roof. Because CO and CO_2 are complementary, the CO is rich near the roof where CO_2 is poor via dissociation of CO_2 to produce CO (OX26). Meanwhile, CO_2 is rich near the substrate where the gas reaction of COF_x and CF_x (Ox31, Ox32, Ox34, Ox36, Ox38 and Ox39) and the surface reactions (S7) occur.

Figures 48(a)-(e) show the distributions of SiF_x (x=0~4), which have a strong downhill-like gradient from the center to the substrate edge region because these species produce through the etching processes, depending on the fluxes of radicals and ions transported to the SiO_2 layer. SiF_4 is the dominant etching product while etching SiO_2 in CF_4 discharge, which was also observed in GECRC experiments [37][45][45]. Although the volatile SiF_x (x=0~3) strongly depend on the surface coverage of CF_x

(θ_{CFx}), the volatile SiF$_4$ strongly depends on the surface coverage of F (θ_F). When θ_F is the dominant coverage on the substrate, θ_{CFx}. The distribution of F$_2$ in Figure 48(f) shows a large concentration near the gas inlet because F$_2$ molecules mainly come from the detached recombination of F$^-$ and F (FN11), which are rich near the gas inlet, and it is assumed that F$_2$ would not interact with wall, due to its full chemical bond.

4.2.2 Chemical Ingredients

The chemical ingredients of the charged and the neutral species averaged over the entire region of the reactor are shown in Figure 49 and Figure 50 respectively. Because experimental data is not available, we compare these results with previous GECRC results. The positive ion CF$_3^+$ is also the obvious dominant charge with a concentration of approximately 5.0×10^{16} 1/m^3, which is not as high as in GECRC, because discharge region of dome-shaped reactor is larger than GECRC. Regarding the significant charges CF$_x^+$, the trend of CF$_3^+ >$ CF$_2^+ >$ CF$^+$ is observed in the simulation because of their threshold energies to fragment CF$_4$, which is consistent with GECRC results described in section 4.1.2. The concentration of the negative ion F$^-$ in simulation of CF$_4$ discharge is about 10^{16} 1/m^3, and it is comparable to the concentration of electron in dome-shaped reactor simulation, which was also obtained in GECRC simulation.

For neutral species, because CF$_4$ is fed from the gas inlet, it is the most numerous species as the background gas. F is the dominant radical species with a concentration of 10^{20} 1/m^3, which explains the large value of fluorine coverage. At a given pressure, the number density of CF$_x$ weakly increases as a function of the increasing x (x=1~3) but CF$_2$ is comparable to CF$_3$, which is not consistent with GECRC result. Another two important species COF$_2$ and SiF$_4$ observed in experiment are also relative rich in

78

dome-shaped reactor, and COF_2 concentration is approximately equal to the SiF_4 concentration because they are assumed not to react with the wall and are produced almost from important F coverage in etching process.

4.2.3 Surface Coverage

In the case of dome-shaped reactor. Figure 51 shows the surface coverage as a function of r direction on the substrate. The fluorine surface coverage is still the dominating coverage in dome-shaped reactor simulation because the fluorine atom fluxes are much larger than the fluorocarbon radical fluxes shown in Figure 52. It can be observed that etching process still mainly occurs in the this case because fluorine fluxes are larger than the magnitude of fluorocarbon radical fluxes. The ratio of averaged θ_F : θ_P : ($1 - \theta_F - \theta_{CFx} - \theta_P$) in dome-shaped reactor simulation is approximately 0.8: 0.11: 0.08. Thus, the etching process is more strongly controlled by fluorine surface coverage in dome-shaped reactor than in GECRC, which makes the etching products almost entirely generated from fluorine surface coverage.

4.2.4 Etching Rate and Fluxes to Substrate

Figure 52 shows the fluxes of the ion CF_x^+, the fluxes of the radical CF_x and the etching rate, which has absolute values that are plotted as a function of the radial direction on substrate in dome-shaped reactor. The fluxes decrease smoothly toward the edge, as expected due to the decreased power absorption and static electric field, which has patterns that are consistent with the distributing profiles of the respective

79

species. Obviously, the composition of fluxes to the substrate are 90% F atoms, 9% CF_x radicals, and 0.1% CF_x^+ ions overall. Comparing to GECRC, the ion fluxes decrease a lot in dome-shaped reactor because the discharge region is far for substrate or is larger than GECRC. It is found that the ion fluxes of order at approximately 10^{20} $1/sm^2$ in GECRC decrease to approximately 10^{20} $1/sm^2$ in dome-shaped reactor. Thus, the flux ratio of fluorine atom to ions is approximately 1000, and the flux ratio of fluorocarbon radicals to ions is approximately 100. Therefore, the fluorine coverage occupies the site of SiO_2 more in dome-shaped reactor than in GECRC. Because of more fluorine coverage in dome-shaped reactor, it makes physical sputtering less. On the other hand, if the fluorine coverage and fluorocarbon coverage is formed, the only way to remove them is ion-enhanced chemical etching. However, decreasing ion fluxes make ion-enhanced chemical etching hard. It is obvious that etching rate is lower in dome-shaped reactor than in GECRC.
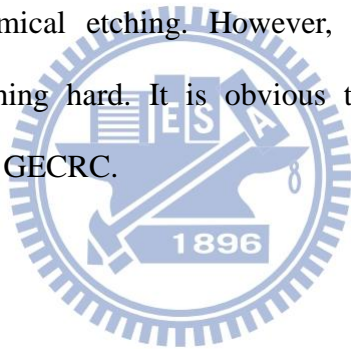
4.3 Comparison of Etching Rates in Different Type of Inductively Coupled Plasma Reactors

This section reports comparison of etching properties in different types of inductively coupled plasma sources (ICPs) with tetrafluoromethane (CF_4) gas using our developed parallel 2-D axisymmetric fluid model.

4.3.1 Reactor Geometries

The testing reactor geometries of ICPs include typical reactor with planar (top) coils, typical reactor with cylindrical (side) coils, and dome-shaped reactors shown in Figure 53. Figure 53 gives (a) gas inlet ring set beside typical cylindrical ICP chamber with planar coils, (b) gas inlet ring set beside typical cylindrical ICP chamber with cylindrical coils (side), (C) gas inlet port set upon typical cylindrical ICP chamber with cylindrical coils (side), (d) gas inlet port set upon dome-shaped ICP reactor of elliptic roof, (e) gas inlet port set upon dome-shaped ICP reactor of spherical roof, (f) gas inlet ring set beside dome-shaped ICP reactor of elliptic roof, and (g) gas inlet ring set beside dome-shaped ICP reactor of spherical roof. Figures 54, 55, 56 and 57 show the schematics of reactor geometries and coil configurations in detail respectively. The typical ICP reactor has simple cylindrical chamber which has height of 10 cm and radius of 20 cm. A 12-inch wafer is located on the bottom of reactor. Form this typical rector, if we extend the flat roof to a shape of elliptic or sphere, it becomes the so-called dome-shaped ICP reactor. The possible positions of gas inlet were also tested in these ICP reactors.

4.3.2 Testing Conditions

These simulations are examined under the same conditions: a gas pressure of 20 mTorr, a CF_4 flow rate of 230 sccm, and a deposited power of 200 W driven by 13.56 MHz frequency of current. The temperatures of the ion and the neutral species are assumed to be constant at 0.026 eV and 400 K respectively. The ion bombardment energy to the substrate is set at 100 eV at the substrate boundary. The grid resolution in both radial and axial directions is 1 mm. This grid size leads to approximately a total 2.5 million unknowns as considering 32 species, and this grid size has to perform via parallel computing to reduce running time within one day.

4.3.3 Spatial Profiles
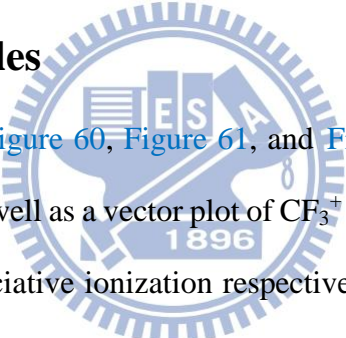
Figure 58, Figure 59, Figure 60, Figure 61, and Figure 62 show the 2-D spatial profiles for n_e, streamline as well as a vector plot of CF_3^+ flux and CF_3^+ density, T_e, CF_4, and production rate of dissociative ionization respectively. In Figure 58, it is obvious that the concentration of electron accumulates near the gas inlet as gas inlet port located upon the top roof of chamber ((c), (d) and (e)), or n_e is peaked on axis as the inlet ring located beside the chamber ((a), (b), (f) and (g)). Because the uniformity of n_e known as discharge region strongly affect those fluxes to the SiO_2 substrate, it can be predicted that the etching uniformity in case of (b) must be the smoothest since n_e is peaked with a more extended and flatter region from center to edge as comparing to others. In contrast, for the cases ((c), (d) and (e)) of the gas inlet port set upon the root, n_e are constrained near region of gas inlet port because it can be find that the negative ions are mainly produced in gas inlet region where the electron temperature is relatively low so that electrons have to follow the positive and negative ions out of the system to

82

maintain discharge, or the discharge will be collapsed. Later we will present that the discharge regions near the gas inlet port located upon the roof cause the etching uniformity rough in these case. In contrast, the discharge regions in the cases of dome-shaped reactor with gas inlet ring beside the chamber ((f) and (g)) are more extensive than the cases of typical cylindrical reactors ((a) and (b)), and they are deposited under similar power. Therefore, because of larger discharge region but the same power in series of dome-shaped reactor, we find that the plasma densities near the substrate in typical cylindrical reactors are richer than dome-shaped reactors. In this regard, it can predict that the etching rate of typical cylindrical reactors with side coils and top coils ((a) and (b)) will be higher than the etching rate of dome-shaped reactors ((f) and (g)). Before we show the comparison of etching uniformity and etching rate, we conclude that etching uniformity in case of (b) is must be the smoothest with relatively high etching rate. In the following, we will proof this point.

There are several effects that conspire to cause the density profile in Figure 58(b). To understand these effects better, consider first the profile of ion flux streamline in Figure 59. The streamlines of ion flux also show that the discharge region is the widest and smoothest in Figure 59(b) as comparing to other cases. It is evident that the ion flux to the substrate is flat because the discharge extends from center to almost edge of substrate. Second, in Figure 60(b), electron temperature is peaked near the quartz region where the power is depositing beside the chamber and hence electron heating takes place off axis, but the electron thermal conductivity is relatively high in low pressure so that the plasma near center could obtain enough energy from off-axis region to discharge. Moreover, electron temperature is strongly relating to the dissociative ionization rate constant $K(T_e)$ to affects the density profile. However, $K(T_e)$ is not the main reaction to make the discharge region so extended and smooth, because the

plasma discharge is strongly influenced by combination of $K(T_e)$, n_e, and background gas feeding CF_4. Next we will clearly discuss the spatial profile of CF_4 and production rate of dissociative ionization that is the combination of n_e, CF_4 and $K(T_e)$. In the Figure 61(b), the feedstock gas CF_4 flow from inlet ring into the chamber. Then, CF_4 is dissociated in the inlet region where the $K(T_e)$ is relatively high, whose production rate is shown as Figure 62(b). It is evident that the dissociative ionization tends to peak off-axis to affect CF_3^+ density profile most likely off-axis. In this case, the ion transport plays a more dominant role in determining the radial density profile. Now going back to the ion flux plot of Figure 59(b), it makes clear that ions born at large radius will preferentially flow to top and bottom surfaces of the reactor, thus making it difficult for ions to fill in the center of chamber.

On the contrary, Figures 59(c), 59(d) and 59(e) indicate that the discharge regions are constrained near the gas inlet, and the ion transport from discharge region to the SiO_2 is far and non-uniform. A reason that makes density profile in Figures 59(c), 59(d) and 59(e) first is the electron temperature is relatively low and CF_4 is relative high in that discharge region as comparing to other region, which are shown as Figures 60(c), 60(d) and 60(e). Negative ions tend to be generated in the low electron temperature from electron dissociatively attaching to CF_4. Therefore, more negative ions are produced, and these negative ions are difficult to transport in radial direction to extend the plasma discharge region. Another possible point is that the density of CF_4 fed from top inlet port (Figures 61(c), 61(d) and 61(e)) present higher approximately two order than those fed from side inlet ring (Figures 61(a), 61(b), 61(f) and 61(g)) under the same flow rate. Hence it is obvious that although $K(T_e)$ is relatively low, the concentrations of electron and CF_4 are relatively high to make production rate so higher near top gas inlet in Figures 62(c), 62(d) and 62(e).

On the other hand, for the cases of dome-shaped reactors with gas inlet ring beside chambers (cases of (f) and (g)), the streamlines in Figure 59 describe that the discharge regions in (f) and (g) are closer to substrate than those in (d) and (e). However, it is clear that the streamlines to the substrate show only the diffusion effect dominant in all dome-shaped reactors because the variation between positive and negative charged particles causes small electric field that can ignore the drift effect. The production rates in Figure 62(f) show higher rate than that in Figure 62(g) near the substrate. Therefore, it could be predicted that the etching rate of SiO_2 in dome-shaped reactor with elliptic roof is higher than that in dome-shaped reactor with spherical roof.

4.3.4 Fluxes, Coverage and Etching Rate

Figure 63 shows the radial profile of CF_3^+ fluxes to the substrate. It is clear that the CF_3^+ flux in (b) is really smoother than other cases and the flux only slightly drop down at end of substrate. In the case (a), the etching uniformity can be seen a little flat at central part but drops down gradually at middle substrate. In the case (c), as can be seen from the figure, it is dramatic decrease for the CF_3^+ flux from center to edge on substrate, and it proofs that the dramatic decrease will affect the etching uniformity to be rough. In contrast, the CF_3^+ fluxes in dome-shaped reactors are much lower than typical cylindrical reactors. Figure 64 presents the radial profile of F fluxes to the substrate. All of F fluxes have similar trends that smooth decrease from central axis to edge except for the case of (c). It is clear F flux in (c) drop down rapidly because the discharge is constrained in front of gas inlet port and is closed to substrate so that larger fluxes will flow to central substrate.

Figure 65 shows the radial profile of coverage of F atom on the substrate, and the coverage of F is strongly and nonlinearly depending on the flux of CF_3^+ and the flux of

85

F. First, all coverages rise from central substrate to edge except for (b). In the (b), the coverage decreases from center to edge on substrate but a climbing at edge because the CF_3^+ flux to substrate is flat and the F flux to the substrate is in a decrease so that F covers less but CF_3^+ etches more. In addition, it is appears that the coverages of F atom in dome-shaped reactors are relatively higher than typical cylindrical reactors since the CF_3^+ fluxes are less in those dome-shaped reactors.

Let us discuss the radial profile of etching rate shown as Figure 66. As expected, it is obvious that (b) shows the smoothest etching uniformity among all testing reactors. In the case (a), the etching rate almost higher than other cases except (c), but rougher than (b), and as smooth as (d), (e), (f) and (g). In the case (b), the etching uniformity is smoothest, and the etching rate is relatively higher than dome-shaped reactor because the discharge region shows off-axis. In the case (c), the etching rate is highest but roughest. In the dome-shaped reactor (d), (e), (f) and (g), the etching rates are not as high as in typical ICP reactors, and they have as smooth as etching uniformity in case (a). The etching rate is uniform in (b) because the CF_3^+ flux slightly rise before 12 cm but the F flux fall on substrate so that the F coverage fall among these testing reactor. Moreover, "ion-enhanced chemical etching by F" and "ion-enhanced chemical sputtering" make the coverage in (b) is relatively low. It is summarized that the case (b) has relatively valuable to be applied in etching SiO_2 for semiconductor manufacture due to perfect uniformity and relative high etching rate. The choices of coil position, reactor geometry, and gas inlet position lead to distinctly different etching property. These choices affect where the discharge region is so that these regions strongly influence the fluxes to the substrate. The fluxes to the substrate make the coverage different to obtain the different profiles of etching rate. It is obviously seen that the etching rates and uniformities strongly depend on plasma discharge region.
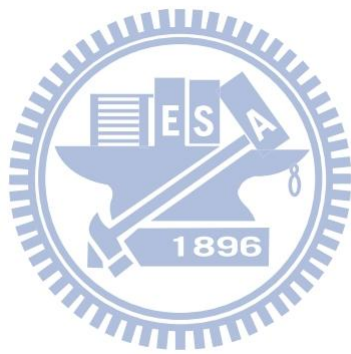
CHAPTER 5

CONCLUSION AND RECOMMENDATIONS

FOR FUTURE WORK

5.1 Summary

Major studies and findings of the current thesis can be summarized as follows:

1. We have succeeded in developing and validating a MPI-based parallel 2D-axisymmetric fluid modeling code, using domain decomposition and coupling with the Maxwell's equation solver and surface kinetic model, which can be used to simulate a future large-scale ICP source.

2. The developed parallel fluid modeling code can be scalable up to 26 processors on a PC cluster, IBM-1350 at NCHC of Taiwan, with a problem size of 122×179 grid points, 32 species, 96 gas reactions and 27 surface reactions for a CF4 ICP simulation. In addition, the combination of preconditioning and Krylov subspace iterative method using, respectively, the GMRES and the Block Jacobi algorithms with ILU as the sub-domain solver gives the best parallel performance for the fluid modeling code.

3. In all types of ICP reactors considered in this thesis (cylindrical-shaped, GECRC and dome-shaped), the numerical results indicate that plasma induced electric field is 10-15% of the coil-induced electric field near the coils (skin depth ~ 1 cm in thickness) in the chamber, which was ignored by Fukumoto et al. [26] using the analytical Biot-Savart's law in solving the Maxwell equation directly.

4. In all types of ICP reactors, simulations show that CF_3^+ is the most dominant charged species, followed by CF_3^+, CF_2^+ and CF^+, while the concentration of F^- is comparable to that of electron in the CF_4 ICP discharge. In addition, reactive F atom is the most dominant radical, followed by CF_3, CF_2 and CF alternatly.

5. Simulations show that F atom and CF_3^+ are the most dominant species of the radical and ion fluxes toward the SiO_2 substrate, respectively, followed by CF_3, CF_2 and CF, and CF_3^+, CF_2^+ and CF^+ in the order of decreasing amount.

6. Simulations show that etching of SiO_2 substrate proceeds in two steps. The substrate surface is first covered by radicals (F atom dominating up to 60% in GECRC and 80% in dome-shaped ICP reactos), followed by surface reactions with impinging ion fluxes (CF_3^+ dominating up to 90%) and then release etchng products into the plasma region. In addition, the major etching products from the SiO_2 substrate are found to be SiF_4, COF_2 and O_2 in.the order of increasing amount, which coincides with the experimental observations [45].

7. Comparison of etching profiles shows that proper arrangement of gas inlet location, geometry of chamber and coils position is critical in determining the etch rate and uniformity at the substrate surface. Results show that the combination of gas inlet ring located around top side wall and coils around the side wall performs the best in relatively high etch rate and good uniformity at the substrate surface.

5.2 Recommendations for Future Work

The recommendations for future works are summarized as follows:

1. To develop a time-dependent Maxwell's equation solver, such as finite-difference and time-domain method, which can be used for dual-frequency (or even triple-frequency) applications that have been often seen in several industrial applications.

2. To perform important parametric studies on various kinds of ICP sources such as cylindrical-shaped and dome-shaped reactors.

3. To apply the developed fluid modeling code and modify the surface kinetic model for properly simulating ICP sources using SiH_4 as the precursor in several experimental studies and comparing the data wherever is available.

4. To develop a numerical model for solving the full momentum equations of ions without the drift-diffusion approximation that fails in the nearly collisionless sheath.

5. To improve the fluid model using by incorporating a gas flow solver developed in our group that can provide the thermal and flow field under rarefied conditions using slip and jump boundary conditions for velocities and temperature fields..

REFERENCES

[1] R.J. Shul and S.J. Pearton, "Handbook of Advanced Plasma Processing Techniques", Springer, (2000)

[2] Francis F. Chen, "Introduction to plasma physics and controlled fusion. Volume 1, Plasma physics", Plenum Press, New York (1984)

[3] Michael A. Lieberman, and Alan J. Lichtenberg, "Principles of Plasma Discharges and Materials Processing , 2nd Edition", Wiley-Interscience (2005)

[4] Alexander A. Fridman, and Lawrence A. Kennedy, "Plasma Physics and Engineering", Taylor & Francis (2004)

[5] Rainer Hippler, Holger Kersten, Martin Schmidt, and Karl H. Schoenbach, "Low Temperature Plasmas: Fundamentals, Technologies and Techniques, 2nd Edition" WILEY-VCH (2008)

[6] A. Bogaerts, E, Neyts, R, Gijbels, and Joost van der Mullen, Spectrochimica Acta Part B **57**, 609 (2002)

[7] H. Treichel, G. Ruhl, P. Ansmann, R. Wure, Ch. Muller, and M. Dietlmeier, Microelectron. Eng. 40, 1 (1998)

[8] I. Morey and A. Asthana, Solid State Technol. 42, 71 (1999)

[9] S. Hamaguchi, IBM J. Res. Develop. 43, 199 (1999)

[10] Vipin Kumar, Ananth Grama, Anshul Gupta, George Karpis, "Introduction to Parallel Computing: Design and Analysis of Parallel Algorithms", Benjamin-Cummings Pub. Co. (1994)

[11] H. C. Kim, F. Iza, S. S. Yang, M. Radmilovic-Radjenovic and J. K. Lee, J. Phys. D: Appl. Phys. 38, R283 (2005)

[12] S. Hamaguchi, IBM J. Res. Develop. 43, 199 (1999)

[13] M. M. Turner, J. Phys. D: Appl. Phys. 42, 1 (2009)

[14] T. Makabe 2002 Advances in Low Temperature RF Plasmas: Basis for Porcess Design (Amsterdam: Elsevier)

[15] P. L. G. Ventzek, R. J. Hoekstra and M. J. Kushner, J. Vac. Sci. Technol. B 12, 461 (1993)

[16] R. A. Stewart, P. Vitello and D. B. Graves, J. Vac. Sci. Technol. B 12, 478 (1993)

[17] R. A. Stewart, P. Vitello, D. B. Graves, E. F. Jaeger and L. A. Berry, Plasma Sources Sci. Technol. 4, 36 (1995)

[18] D. P. Lymberopoulos, V. I. Kolobov and D. J. Economou, J. Vac. Sci. Technol. A 16, 564 (1997)

[19] C. C. Hsu, M. A. Nierode, J. W. Coburn and D. B. Graves, J. Phys. D: Appl. Phys. 39, 3272 (2006)

[20] F. Gas, S.-X. Zhao, X.-S. Li and Y.-N. Wang, Phys. Plasma 16, 113502 (2009)

[21] S.-X. Zhao, F. Gas and Y.-N. Wang, J. Phys. D: Appl. Phys. 42, 1 (2009)

[22] D. P. Lymberopoulos and D. J. Economou, IEEE Trans. Plasma Sci. 23, 573 (1995)

[23] B. Ramamurthi and D. J. Economou, J. Vac. Sci. Technol. A 20, 467 (2002)

[24] B. Ramamurthi and D. J. Economou, Plasma Source Sci. Technol. 11, 324 (2002)

[25] D. B. Hash, D. Bose, M. V. V. S. Rao, B. A. Cruden, M. Meyyappan and S. P. Sharma, J. Appl. Phys. **90**, 2148 (2001)

[26] H. Fukumoto, I. Fujikake, Y. Takao, K. Eriguchi and K. Ono, Plasma Source Sci. Technol. 18, 045027 (2009)

[27] R. B. Bird, Warren E. Stewart E. N. Lightfoot, "Transport Phenomena", 2nd Edition (Jone Wiley & Sons, Inc)

[28] P. L. G. Ventzek, R. J. Hoekstra and M. J. Kushner, J. Vac. Sci. Technol. B 12, 461 (1994)

[29] T. Kimura and K. Ohe, Plasma Sources Sci. Technol. 8, 553 (1999)

[30] T. Kimura and K. Ohe, J. Appl. Phys. **92**, 1780 (2002)

[31] T. Kimura and M. Noto, J. Appl. Phys. **100**, 63303 (2006)

[32] T. Kimura and K. Hanaki, Jpn. J. Appl. Phys. **47**, 8537 (2008)

[33] D. Bose, D. Hash, T. R. Govindan and M. Meyyappan, J. Phys. D: Appl. Phys. 34, 2742 (2001)

[34] M. W. Kiehlbauch and D. B. Graves, J. Appl. Phys. 89, 2047 (2001)

[35] K. N. Ostrikov, I. B. Denysenko, E. L. Tsakadze, S. Xu, and R. G. Storer, J. Appl. Phys. 92, 4935 (2002)

[36] J. W. Coburn, and H. F. Winters, J. Vac. Sci. Technol. 16, 391 (1979)

[37] J. W. Coburn, H. F. Winters, and T. J. Chuang, J. Appl. Phys. 48, 3532 (1977)

[38] Y. Hikosaka, M. Nakamura, and H. Sugai, Jpn. J. Appl. Phys. **33**, 2157 (1994)

[39] J. A. O'Neill and J. Singh, J. Appl. Phys. **77**, 497 (1995)

[40] C. J. Choi, O. S. Kwon, Y. S. Seol, Y. W. Kim, and I. H. Choi, J. Vac. Sci. Technol. B 18, 811 (2000)

[41] J. K. Olthoff and Y. Wang, J. Vac. Sci. Technol. A 17, 1552 (1999)

[42] H. Singh, J. W. Coburn, and D. B. Graves, J. Vac. Sci. Technol. A 19, 718 (2001)

[43] G. A. Hebner, J. Appl. Phys. **90**, 4938 (2001)

[44] G. A. Hebner, J. Appl. Phys. **89**, 900 (2001)

[45] B. A. Cruden, M. V. V. S. Rao, S. P. Sharma and M. Meyyappan, Plasma Sources Sci. Technol. **11**, 77 (2002)

[46] B. A. Cruden, M. V. V. S. Rao, S. P. Sharma, and M. Meyyappan, J. Appl. Phys. **91**, 8955 (2002)

[47] B. A. Cruden, M. V. V. S. Rao, S. P. Sharma, and M. Meyyappan, J. Appl. Phys. **93**, 5053 (2003)

[48] M. V. V. S. Rao, S. P. Sharma and M. Meyyappan, Plasma Sources Sci. Technol. **11**, 397 (2002)

[49] M. V. V. S. Rao, S. P. Sharma, B. A. Cruden and M. Meyyappan, Plasma Sources Sci. Technol. **11**, 69 (2002)

[50] B. Zhou,E. A. Joseph, L. J. Overzet, and M. J. Goeckner, J. Vac. Sci. Technol. A **24**, 114 (2005)

[51] D. Zhang and Mark J. Kushner, J. Appl. Phys. 87, 1060 (2000)

[52] M. Meyyappan and T. R. Govindan, J. Appl. Phys. **74**, 2250 (1993)

[53] E. W. McDaniel and E. A. Mason, "The mobility and diffusion of ions in gases", New York: Wiley (1973)

[54] E. Gogolidesa, P. Vauvert, G. Kokkoris, G. Turban and A. G. Boudouvis, J. Appl. Phys. **79**, 3718 (2000)

[55] G. Kokkoris, E. Gogolides, and A. G. Boudouvis, J. Appl. Phys. **91**, 2697 (2002)

[56] P. Ho, J. E. Johannes, and R. J. Buss, and E. Meeks, J. Vac. Sci. Technol. A **19**, 2344 (2001)

[57] L. G. Christophorou, J. K. Olthoff, and M. V. V. S. Rao, J. Phys. Chem. Ref. Data **25**, 1344 (1996)

[58] R. R. Laher, and F. R. Gilmore, J. Phys. Chem. Ref. Data **19**, 277 (1990)

[59] H. U. Poll, and J. Meichsner, Beitr. Plasmaphys. **27**, 359 (1987)

[60] V. Tarnovsky, P. Kurunczi, D. Rogozhinikov and K. Becker, Int. J. Mass Spectrom. Ion Processes **128**, 181 (1993)

[61] T. R. Hayes, R. C. Wetzel, and R. S. Freund, Phys. Rev. A **35**, 578 (1987)

[62] Y. Itikawa and A. Ichimura, J. Phys. Chem. Ref. Data **19**, 637 (1990)

[63] J. E. Land, J. Appl. Phys. **49**, 5716 (1976)

[64] P. C. Cosby, J. Chem. Phys. **98**, 7804 (1993)

[65] D. Rapp and P. Englander-Golden, J. Chem. Phys. **43**, 1464 (1965)

[66] G.J.M. Hagelaar and L.C. Pitchford, Plasma Sources Sci. Technol. **14**, 722 (2005)

[67] National Institute of Standards and Technology (NIST), http://www.nist.gov/index.html

[68] National Institute for Fusion Science (NIFS), http://dbshino.nifs.ac.jp/

[69] S. C. Chapra and R. Canale, "Numerical Methods for Engineers: With Software and Programming Applications", McGraw-Hill (2006)

[70] Z. Bai, Appl. Numer. Math **43**, 9 (2002)

[71] Y. Saad, "Iterative methods for sparse linear systems", SIAM (2003)

[72] S. Balay, W. D. Gropp, L. C. McInnes and B. F. Smith, "Efficient Management of Parallelism in Object Oriented Numerical Software Libraries", Birkh user Press (1997)

[73] W. Gropp, E. Lusk, and A. Skjellum, "Using MPI: Portable Parallel Programming with the Message Passing Interface.", MIT Press (1994)

[74] H. Fukumoto, K. Ono and K. Takahashi, International Symposium on Plasma Chemistry 17 (2005)

[75] Taylor and Francis Group, "CRC Handbook of Chemistry and Physics 92nd Edition", 2011

[76] J. P. Bouanich, J. Quant. Spectrosc. Radiat. Transfer 47, 243 (1992)

[77] A. Mandl, J. Chem. Phys. **59**, 3423 (1973)

[78] H. Tanaka, T. Ishikawa, T. Masai, T. Sagara, L. Boesten, M. Takekawa and Y. Itikawa, Phys. Rev. A **57**, 1798–1808 (1998)

[79] C.-T. Hung, Y.-M. Chiu, F.-N. Hwang, J.-S. Wu, Computer Physics Communications **182**, 161 (2011)

[80] V. Georgieva, A. Bogaerts, R Gijbels, J. Appl. Phys. **94**, 3748 (2003)
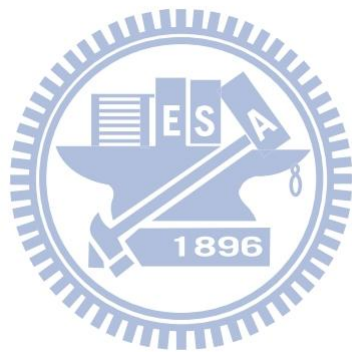
TABLES

Table 1: Summary of fluid model used for electropositive inductively coupled discharge.

	R. A. Stewart and D. B. Grave (1993)	R. A. Stewart D. B. Grave	D. P. Lymberopoulos and D. J. Economou	B. Ramamurthi and D. J. Economou	Y.-N. Wang (2009)
Electric field	Poisson	Poisson	Poisson	Flux balance	Poisson
Electron	Drift-diffusion	Drift-diffusion	Drift-diffusion	Flux balance	Drift-diffusion
	Continuity eq.	Continuity eq.	Continuity eq.	Quasi-neutral	Continuity eq.
	Energy eq.	Energy eq.	Energy eq.	Energy eq.	Energy eq.
Ions	Momentum eq.	Momentum eq.	Momentum eq.	Drift-diffusion with ambipolar	Momentum eq.
	Continuity eq.	Continuity eq.	Continuity eq.	Continuity eq.	Continuity eq.
Neutral	Background gas is uniform	Background gas is uniform	Continuity eq.	Continuity eq.	Continuity eq.
Maxwell's equation	Power profile is assumed	Maxwell's equation	Maxwell's equation	Maxwell's equation	Maxwell's equation
Annotation	Gas: Ar Typical reactor	Gas: Ar Typical reactor	Gas: Ar (1D) Typical reactor	Gas: Ar 10 kHz (pulse power) Typical reactor	EEDF (M.C.) Gas: Ar Typical reactor

Table 2: Summary of fluid model used for electronegative inductively coupled discharge.

	D. P. Lymberopoulos and D. J. Economou (1995)	B. Ramamurthi and D. J. Economou (2001)	D. B. Hash and M. Meyyappan (2001)	C. C. Hsu and D. B. Grave (2006)	H. Fukumoto and K. Ono (2009)
Electric field	Poisson	Flux balance	Flux balance	Flux balance	Flux balance
Electron	drift-diffussion	Flux balance	Flux balance	Flux balance	Flux balance
	Continuity eq.	Quasi-neutral	Quasi-neutral	Quasi-neutral	Quasi-neutral
	Energy eq.	Energy eq.	Energy eq.	Energy eq.	Energy eq.
Ions	drift-diffussion with effective electric field	Drift-diffusion with ambipolar	Drift-diffusion with ambipolar	Drift-diffusion with ambipolar	Drift-diffusion with ambipolar
	Continuity eq.	Continuity eq.	Continuity eq.	Continuity eq.	Continuity eq.
Neutral	Continuity eq.	Continuity eq.	Continuity eq.	Mass eq.	Continuity eq.
			Momentum eq.	Momentum eq.	
			Energy eq.	Energy eq.	
Maxwell's equation	Maxwell's eq.	Maxwell's eq.	Maxwell's eq.	Maxwell's equation	Maxwell's eq. (Bio-S.)
Annotation	Gas: Cl_2 Typical reactor	Gas: Cl_2 Pulsed power GECRC	(SEMS) Gas: CF_4 GECRC	Gas: Ar, Ar/Cl_2, Ar/O_2 Surface model	Gas: CF_4 Surface model Typical chamber

Table 3: Overview of the species included in the model and corresponding parameters for transport properties.

species	$\sigma(A)$ L.-J. parameter	$\varepsilon(K^o)$ L.-J. potential	$\alpha(A^3)$ polarizability	Reference
Electron	0	0	0	N/A
F^+	2.968	112.6	0.6	[33]
CF^+	3.635	94.2	1.8	[33]
CF_2^+	3.977	108	2.82	[33]
CF_3^+	4.32	121	2.82	[33]
O^+	3.04	103.85	0.802	[19]
O_2^+	3.433	113.0	1.5812	[19]
CO^+	3.59	110.0	1.95	[19]
SiF^+	3.662 [a]	95.8 [a]	4.62 [c]	[75]
SiF_2^+	3.803 [a]	133.1 [a]	4.62 [c]	[75]
SiF_3^+	3.943 [a]	170.3 [a]	4.62 [c]	[75]
F^-	2.968	112.6	0.6	[33]
O^-	3.04	103.85	0.802	[19]
F	2.968	112.6	0.6	[33]
CF	3.635	94.2	1.8	[33]
CF_2	3.977	108	2.82	[33]
CF_3	4.32	121	2.82	[33]
O	3.04	103.85	0.802	[19]
O_2	3.433	113.0	1.5812	[19]
$O(^1D)$	3.04	103.85	0.802	[19]
$O_2(a^1\Delta_g)$	3.433	113.0	1.5812	[19]
COF	3.941 [b]	195.2 [b]	1.95 [b]	Estimated
COF_2	3.941 [b]	195.2 [b]	1.95 [b]	Estimated
CO	3.59	110.0	1.95 [b]	[75][76]
CO_2	3.941	195.2	1.95 [b]	[75][76]
Si	2.91	93.6231	5.38	[75]
SiF	3.662 [a]	95.8 [a]	5.38	[75]
SiF_2	3.803 [a]	133.1 [a]	5.38	[75]
SiF_3	3.943 [a]	170.3 [a]	5.38	[75]
SiF_4	4.084 [a]	207.6 [a]	5.45	[75]
F_2	3.357	112.6	0.9	[75]
CF_4	4.662	134	2.82	[33]

[a] Estimate based on SiH_x analogy.

[b] Estimate based on CO or CO_2.

[c] Estimate based on SiH_x^+ analogy.

Table 4: Reactions of electron-impact with CF_x (x=1~4) and relative gas-phase reactions.

Index	Reaction	Threshold energy (eV)	Rate constant (m^3s^{-1})	Ref.
F00	$e + CF_4 \rightarrow CF_4 + e$	0	EEDF(σ)	[56]
F01	$e + CF_3 \rightarrow CF_3^+ + 2e$	9.09	EEDF(σ)	[57] [68]
F02	$e + CF_2 \rightarrow CF_2^+ + 2e$	11.5	EEDF(σ)	[57] [68]
F03	$e + CF \rightarrow CF^+ + 2e$	9.17	EEDF(σ)	[57] [68]
F04	$e + F \rightarrow F^+ + 2e$	17.5	EEDF(σ)	[61] [68]
F05	$e + CF_4 \rightarrow CF_3^+ + F + 2e$	14.8	EEDF(σ)	[56]
F06	$e + CF_4 \rightarrow CF_2^+ + 2F + 2e$	20.8	EEDF(σ)	[56]
F07	$e + CF_4 \rightarrow CF^+ + 3F + 2e$	23.9	EEDF(σ)	[56]
F08	$e + CF_3 \rightarrow CF_2^+ + F + 2e$	15.2	EEDF(σ)	[57]
F09	$e + CF_3 \rightarrow CF^+ + 2F + 2e$	18.2	EEDF(σ)	[57]
F10	$e + CF_2 \rightarrow CF^+ + F + 2e$	14.6	EEDF(σ)	[57]
F11	$e + CF_4 \rightarrow CF_3 + F + e$	5.67	EEDF(σ)	[56]
F12	$e + CF_4 \rightarrow CF_2 + 2F + e$	9.32	EEDF(σ)	[56]
F13	$e + CF_4 \rightarrow CF + 3F + e$	14.7	EEDF(σ)	[56]
F14	$e + CF_3 \rightarrow CF_2 + F + e$	3.65	EEDF(σ)	[57]
F15	$e + CF_3 \rightarrow CF + 2F + e$	9.04	EEDF(σ)	[57]
F16	$e + CF_2 \rightarrow CF + F + e$	5.39	EEDF(σ)	[57]
F17	$e + F_2 \rightarrow F + F + e$	1.65	EEDF(σ)	[25]
F18	$e + CF_3^+ \rightarrow CF_2 + F$	-5.44	6.0×10^{-14}	[25]
F19	$e + CF_2^+ \rightarrow CF + F$	-6.1	6.0×10^{-14}	[25]
F20	$e + CF_3^+ \rightarrow CF_3$	-8.5	4.0×10^{-14}	[25]
F21	$CF_3 + F_2 \rightarrow CF_4 + F$	0	1.5×10^{-20}	[25][67]
F22	$CF_2 + F_2 \rightarrow CF_3 + F$	0	8.3×10^{-20}	[25] [67]
F23	$CF_4 + CF_3 + F \rightarrow 2CF_4$	0	1.47×10^{-40}	[25] [67]
F24	$CF_4 + CF_2 + F \rightarrow CF_3 + CF_4$	0	1.42×10^{-41}	[25] [67]
F25	$CF + F \rightarrow CF_2$	0	1.0×10^{-19}	[26] [67]
F26	$F^+ + CF_3 \rightarrow F + CF_3^+$	0	6.0×10^{-15}	[25][68]
F27	$F^+ + CF_4 \rightarrow F_2 + CF_3^+$	0	6.0×10^{-15}	[25] [68]

Table 5: Reactions including negative charge F⁻.

Index	Reactions	Threshold energy	Rate constant $(m^3 s^{-1})$	Ref.
FN01	$e + CF_4 \rightarrow CF_3 + F^-$	2.21	EEDF(σ)	[57]
FN02	$e + CF_3 \rightarrow CF_2 + F^-$	0.18	EEDF(σ)a	[25]
FN03	$e + CF_2 \rightarrow CF + F^-$	1.93	EEDF(σ)[a]	[25]
FN04	$e + F_2 \rightarrow F + F^-$	-1.82	EEDF(σ)[a]	[25]
FN05	$e + CF_4 \rightarrow CF_3^+ + F^- + e$	11.3	EEDF(σ)	[57]
FN06	$e + CF_3 \rightarrow CF_2^+ + F^- + e$	11.7	EEDF(σ)	[25]
FN07	$e + F^- \rightarrow F + 2e$	3.47	EEDF(σ)[a]	[25]
FN08	$CF_3 + F^- \rightarrow CF_4 + e$	-2.21	5.0×10^{-16}	[77]
FN09	$CF_2 + F^- \rightarrow CF_3 + e$	-0.18	5.0×10^{-16}	[77]
FN10	$CF + F^- \rightarrow CF_2 + e$	-1.93	5.0×10^{-16}	[77]
FN11	$F + F^- \rightarrow F_2 + e$	1.82	1.39×10^{-16}	[77]
FN12	$CF_3^+ + F^- \rightarrow CF_3 + F$	0	8.8×10^{-13}	[25]
FN13	$CF_2^+ + F^- \rightarrow CF_2 + F$	0	8.8×10^{-13}	[25]
FN14	$CF^+ + F^- \rightarrow CF + F$	0	8.8×10^{-13}	[25]
FN15	$F^+ + F^- \rightarrow 2F$	0	4.0×10^{-13}	[25]
FN16	$CF_3^+ + F^- \rightarrow CF_4$	0	5.0×10^{-14}	[25]

Table 6: Electron-impact reaction for corresponding oxygen-contain species.

Index	Reactions	Threshold energy (eV)	Rate constant (m^3s^{-1})	Ref.
Ox01	$e + O \rightarrow O^+ + 2e$	13.62	EEDF(σ)	[62]
Ox02	$e + O \rightarrow O(^1D) + e$	1.97	EEDF(σ)	[62]
Ox03	$e + O(^1D) \rightarrow O^+ + 2e$	11.65	EEDF(σ)	[62]
Ox04	$e + O_2 \rightarrow O_2^+ + 2e$	12.1	EEDF(σ)	[62]
Ox05	$e + O_2 \rightarrow O_2(v=1) + e$	0.19	EEDF(σ)	[62]
Ox06	$e + O_2 \rightarrow O_2(v=2) + e$	0.38	EEDF(σ)	[62]
Ox07	$e + O_2 \rightarrow O_2(v=3) + e$	0.57	EEDF(σ)	[62]
Ox08	$e + O_2 \rightarrow O_2(v=4) + e$	0.75	EEDF(σ)	[62]
Ox09	$e + O_2 \rightarrow O_2(Ryd) + e$	4.5	EEDF(σ)	[62]
Ox10	$e + O_2 \rightarrow O_2(a^1\Delta_g) + e$	0.977	EEDF(σ)	[62]
Ox11	$e + O_2(a^1\Delta_g) \rightarrow O_2^+ + e$	11.16	EEDF(σ)	[19]
Ox12	$e + O_2(a^1\Delta_g) \rightarrow O^- + O$	2.66	EEDF(σ)	[19]
Ox13	$e + O_2(a^1\Delta_g) \rightarrow O_2 + e$	-0.977	EEDF(σ)	[19]
Ox14	$e + O_2(a^1\Delta_g) \rightarrow 2O + e$	4.19	EEDF(σ)	[19]
Ox15	$e + O_2(a^1\Delta_g) \rightarrow O + O^+ + 2e$	17.7	EEDF(σ)	[19]
Ox16	$e + O_2 \rightarrow 2O + e$	5.17	EEDF(σ)	[67]
Ox17	$e + O_2 \rightarrow O + O(^1D) + e$	7.13	EEDF(σ)	[19]
Ox18	$e + O_2 \rightarrow O^- + O^+ + e$	17.32	EEDF(σ)	[19]
Ox19	$e + O_2 \rightarrow O^- + O$	3.64	EEDF(σ)	[19]
Ox20	$e + O_2 \rightarrow O^+ + O + 2e$	18.84	EEDF(σ)	[19]
Ox21	$e + O_2^+ \rightarrow 2O$	-6.97	Assumed	[19]
Ox22	$e + O^- \rightarrow O + 2e$	1.53	Assumed	[19]

Ox23	$O^- + O \rightarrow O_2 + e$	-3.64	$3.0\times10^{-16}\times(300.0/T_g)^{0.5}$	[19]
Ox24	$O^- + O^+ \rightarrow 2O$	0	$2.7\times10^{-13}\times(300.0/T_g)^{0.5}$	[19]
Ox25	$O^- + O_2^+ \rightarrow O + O_2$	0	$1.5\times10^{-13}\times(300.0/T_g)^{0.5}$	[19]
Ox26	$e + CO_2 \rightarrow CO + O + e$	6.1	EEDF(σ)	[78]
Ox27	$e + COF_2 \rightarrow COF + F + e$	6.0	EEDF(σ)	[78]
Ox28	$e + CO \rightarrow CO^+ + 2e$	14.0	EEDF(σ)	[63][64][65]
Ox29	$CF_3 + O \rightarrow COF_2 + F$	0	3.1×10^{-17}	[67]
Ox30	$CF_3 + O \rightarrow COF + F$	0	1.4×10^{-17}	[67]
Ox31	$CF_2 + O \rightarrow CO + 2F$	0	4.0×10^{-18}	[67]
Ox32	$COF + O \rightarrow CO_2 + F$	0	9.3×10^{-17}	[67]
Ox33	$COF + F \rightarrow COF_2$	0	8.0×10^{-19}	[67]
Ox34	$COF + CF_2 \rightarrow CF_3 + CO$	0	3.1×10^{-19}	[67]
Ox35	$COF + CF_2 \rightarrow COF_2 CF$	0	3.1×10^{-19}	[67]
Ox36	$COF + CF_3 \rightarrow CF_4 + CO$	0	1.0×10^{-17}	[67]
Ox37	$COF + CF_3 \rightarrow COF_2 + CF_2$	0	1.0×10^{-17}	[67]
Ox38	$COF + COF \rightarrow COF_2 + CO$	0	1.0×10^{-17}	[67]
Ox39	$CF + O \rightarrow CO + F$	0	3.0×10^{-17}	[67]
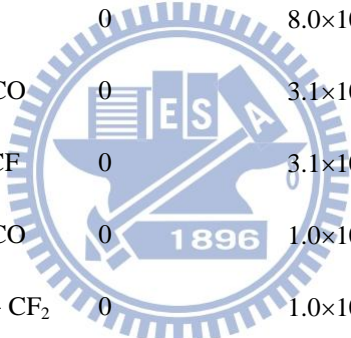
Table 7: Electron-impact and gas-phase reactions for etching products SiF$_x$.

Index	Reactions	Threshold energy (eV)	Rate constant (m^{3}s^{-1})	Ref.
SF01	$e + SiF_4 \rightarrow SiF_3^+ + F + 2e$	16.0	EEDF(σ)	[61]
SF02	$e + SiF_4 \rightarrow SiF_2^+ + 2F + 2e$	23.4	EEDF(σ)	[61]
SF03	$e + SiF_4 \rightarrow SiF^+ + 3F + 2e$	25.1	EEDF(σ)	[61]
SF04	$e + SiF_3 \rightarrow SiF_3^+ + 2e$	9.6	EEDF(σ)	[61]
SF05	$e + SiF_2 \rightarrow SiF_2^+ + 2e$	10.8	EEDF(σ)	[61]
SF06	$e + SiF \rightarrow SiF^+ + 2e$	7.26	EEDF(σ)	[61]
SF07	$e + SiF_4 \rightarrow F^- + SiF_3$	3.8	EEDF(σ)	[61]
SF08	$e + SiF_3^+ \rightarrow SiF_3$	8.5	$\sim 10^{14}$	[56]
SF09	$e + SiF_4 \rightarrow SiF_3 + F + e$	7.25	EEDF(σ)	[61]
SF10	$e + SiF_4 \rightarrow SiF_2 + 2F + e$	11.9	EEDF(σ)	[61]
SF11	$e + SiF_4 \rightarrow SiF + 3F + e$	18.6	EEDF(σ)	[61]
SF12	$SiF_3^+ + F^- \rightarrow SiF_4$	0	$\sim 10^{-14}$	[56]
SF13	$SiF_3 + F \rightarrow SiF_4$	0	1.0×10^{-16}	[26] [56]
SF14	$SiF_2 + F \rightarrow SiF_3$	0	1.0×10^{-16}	[26] [56]
SF15	$SiF + F \rightarrow SiF_2$	0	1.0×10^{-16}	[26] [56]
SF16	$Si + F \rightarrow SiF$	0	1.0×10^{-16}	[26] [56]

Table 8: Reactions of etching processes on SiO_2 substrate in CF_4 discharge.

No.	Reaction	Process	Flux dependency	Surface coverage	Rate coefficient
Physical sputtering					
S1	$SiO_2(s) \rightarrow Si(g)+2O(g)$	Physical sputtering	Γ_{ion}	$1-\theta_{TOT}$	y_{SP}
Reactions with F atoms					
S2	$SiO_2(s)+2F(g) \rightarrow$ $SiO_2F_2(s)$	Adsorption	Γ_F	$1-\theta_{TOT}$	S_F
S3	$SiO_2F_2(s)+2F(s) \rightarrow$ $SiF_4(g)+O_2(g)$	Ion-enhanced chemical etching by F	Γ_{ion}	θ_F	β'_F
S4	$SiO_2F_2(s) \rightarrow$ $SiF_2(g)+O_2(g)$	Ion-enhanced chemical sputtering	Γ_{ion}	θ_F	$\beta'_F b$
S5	$SiO_2F_2(s)+2F(g) \rightarrow$ $SiF_4(g)+O_2(g)$	Thermal etching by F	Γ_F	$1-\theta_{CFx}-\theta_P$	$K(T)$
Reactions with CFx (x=1~3)					
S6	$SiO_2(s)+CF_x(g) \rightarrow$ $SiO_2CF_x(s)$	Chemisorption	Γ_{CFx}	$1-\theta_{TOT}$	S_{CFx}
S7	$2SiO_2CF_x(s) \rightarrow$ $SiF_x(g)+2CO(g)+SiO_2F_x(s)$	Ion-enhanced chemical etching by CF_x radicals	Γ_{ion}	θ_{CFx}	β_{CFx}
S8	$2SiO_2CF_x(s) \rightarrow$ $Si(s)+2COF_x(g)+SiO_2(s)$	C sputtering	Γ_{ion}	θ_{CFx}	y_C
S9	$SiO_2CF_x(s)+F(g) \rightarrow$ $SiO_2(s)+CF_{x+1}(g)$	Recombination of CF_x with F	Γ_F	θ_{CFx}	k_{REC}

Reactions of polymer production of loss

S10	$CF_x^+(g) \rightarrow P$	Direct ion deposition	Γ_{ion}	1	y_d
S11	$SiO_2CF_x(s) \rightarrow P$	Ion-enhanced deposition of sorbed radicals	Γ_{ion}	θ_{CFx}	β_S
S12	$P\text{-}F(s) \rightarrow$ etching of P	Ion-enhanced etching of polymer by F atoms	Γ_{ion}	$\theta_P\theta_{F/P}$	$\beta_{F/P}$
S13	$P\text{-}CF_x(s) \rightarrow$ more P	Ion-enhanced deposition of sorbed radicals	Γ_{ion}	$\theta_P\theta_{CFx/P}$	β_S

Reactions with F atoms on polymer surfaces

S14	$P+2F(g) \rightarrow P\text{-}F_2(s)$	Adsorption	Γ_F	$\theta_P(1-\theta_{TOT/P})$	$S_{F/P}$
S15	$P\text{-}F_2(s)+2F(s) \rightarrow CF_4(g)+O_2(g)$	Ion-enhanced chemical etching by F	Γ_{ion}	$\theta_P\theta_{F/P}$	$\beta_{F/P}$

Reactions with fluorocarbon radicals on polymer surfaces

S16	$P(s)+CF_x(g) \rightarrow P\text{-}CF_x(s)$	Chemisorption	Γ_{CFx}	$\theta_P(1-\theta_{TOT/P})$	$S_{CFx/P}$
S17	$2P\text{-}CF_x(s) \rightarrow 2P(s)+2CF_x(g)$	C sputtering	Γ_{ion}	$\theta_P\theta_{CFx/P}$	y_C
S18	$PCF_x(s)+F(g) \rightarrow P(s)+CF_{x+1}(g)$	Recombination of CF_x with F	Γ_F	$\theta_P\theta_{CFx/P}$	k_{REC}

Table 9: Wall sticking reactions on the metal surface.

No	Reactions	Reaction probability	Ref.
	Reactions of fluorocarbons		
W1	$F^+(g) \rightarrow F(g)$	1.0	[26]
W2	$CF^+(g) \rightarrow CF(g)$	1.0	[26]
W3	$CF_2^+(g) \rightarrow CF_2(g)$	1.0	Assumed
W4	$CF_3^+(g) \rightarrow CF_3(g)$	1.0	[26]
W5	$CF_3(g) \rightarrow CF_3(w)$	0.05	[26]
W6	$F(g) \rightarrow F(w)$	0.02	[26]
W7	$F_2(g) \rightarrow F_2(w)$	0	Assumed
W8	$CF(g) \rightarrow CF(w)$	0.2	[26]
W9	$CF_2(g) \rightarrow CF_2(w)$	0.05	[26]
W10	$CF_3(g) \rightarrow CF_3(w)$	0.05	[26]
W11	$CF_4(g) \rightarrow CF_4(w)$	0	Assumed
	Reactions of oxygen-containing species		
W12	$O^+(g) \rightarrow O(g)$	1.0	[19]
W13	$O_2^+(g) \rightarrow O_2(g)$	1.0	[19]
W14	$CO^+(g) \rightarrow CO(g)$	1.0	[19]
W15	$O(g) \rightarrow 0.5O_2(g)$	0.4	[19]
W16	$O_2(g) \rightarrow O_2(w)$	0	Assumed
W17	$O(^1D) \rightarrow O(g)$	1.0	Assumed
W18	$O_2(a^1\Delta_g)(g) \rightarrow O_2(g)$	0.007	Assume
W19	$CO(g) \rightarrow CO(w)$	0.01	Assume
W20	$CO_2(g) \rightarrow CO_2(w)$	0.01	Assume
W21	$COF(g) \rightarrow COF(w)$	0.01	Assume

W22	$COF_2(g) \rightarrow COF_2(w)$	0.01	Assume

Reactions of silicon fluorides

W23	$SiF^+(g) \rightarrow SiF(g)$	1.0	[26]
W24	$SiF_2^+(g) \rightarrow SiF_2(g)$	1.0	[26]
W25	$SiF_3^+(g) \rightarrow SiF_3(g)$	1.0	[26]
W26	$Si(g) \rightarrow Si(w)$	0.2	[26]
W27	$SiF(g) \rightarrow SiF(w)$	0.2	[26]
W28	$SiF_2(g) \rightarrow SiF_2(w)$	0.02	[26]
W29	$SiF_3(g) \rightarrow SiF_3(w)$	0.05	[26]
W30	$SiF_4(g) \rightarrow SiF_4(w)$	0	Assumed

Table 10: A list of conditions studied by Fukumoto *et al.* [26].

Pressure	10 mTorr	Initial pumping rate	200 L/s
Average power	200 W	Initial current	20 A
Frequency	13.56 MHz	Gas feedstock flow rate	200 sccm
Ion temperature	0.026 eV	Size of grids	32×47 (1,504)
Gas temperature	400		

Table 11: The consuming time for testing parallel efficiency under a condition of ~700,000 unknown in 2000 time steps.

# of processors	GMRES (sec.)		
	ASM	Block Jacobi	SOR
1	8369.46	7971.88	7127.92
2	4184.73	3985.94	3563.96
4	2458.29	2361.78	2469.02
8	979.14	875.44	847.24
16	440.43	410.65	442.28
24	324.01	288.46	311.6
32	309.57	279.59	311.99

Table 12: The estimate of Reynolds number, Peclet number and Kundsen number for gas inlet ring (side) and gas inlet port (up)

	Gas inlet ring (side)	Gas inlet port (up)
Kundsen number (Electron)	0.05	0.1
Kundsen number (CF_4)	0.01	0.06
Peclet number	0.09	0.2
Reynolds number	1230	2954
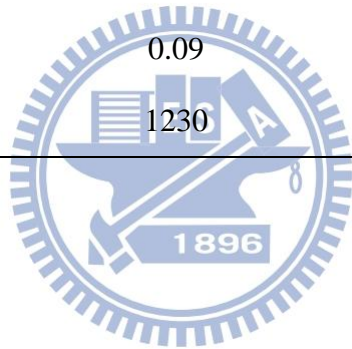
FIGURES
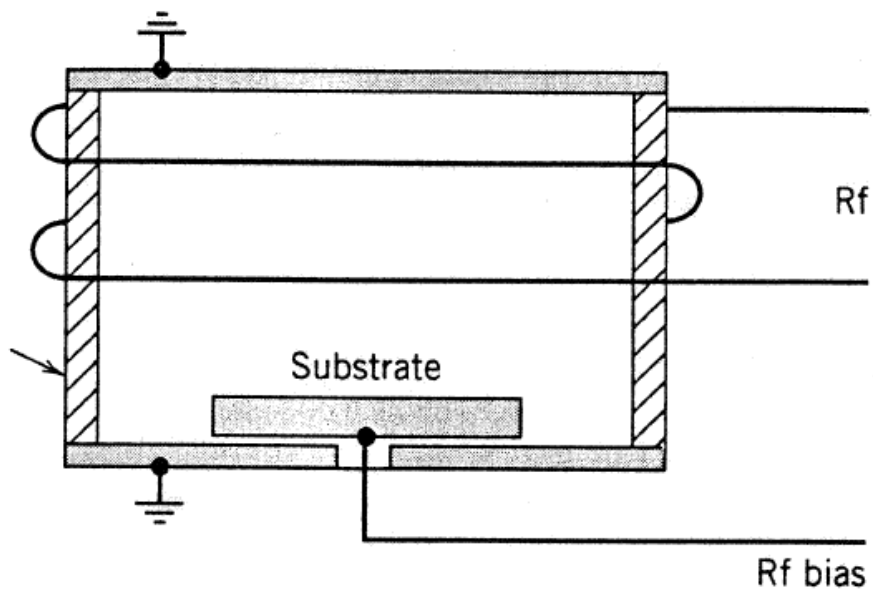
Figure 1: Schematic of inductively driven sources with coil type of cylindrical.

Source: [3]
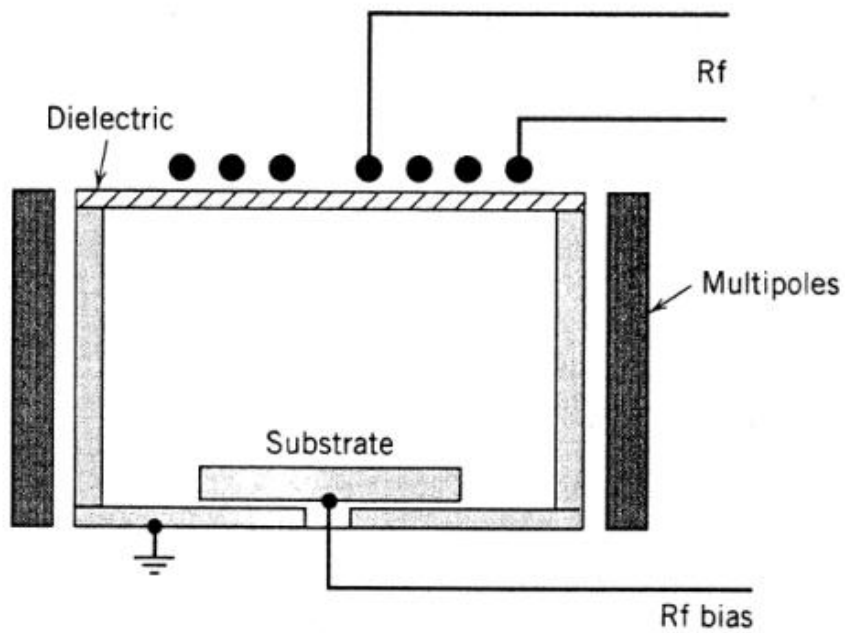
Figure 2: Schematic of inductively driven sources with coil type of planar.

Source: [3]
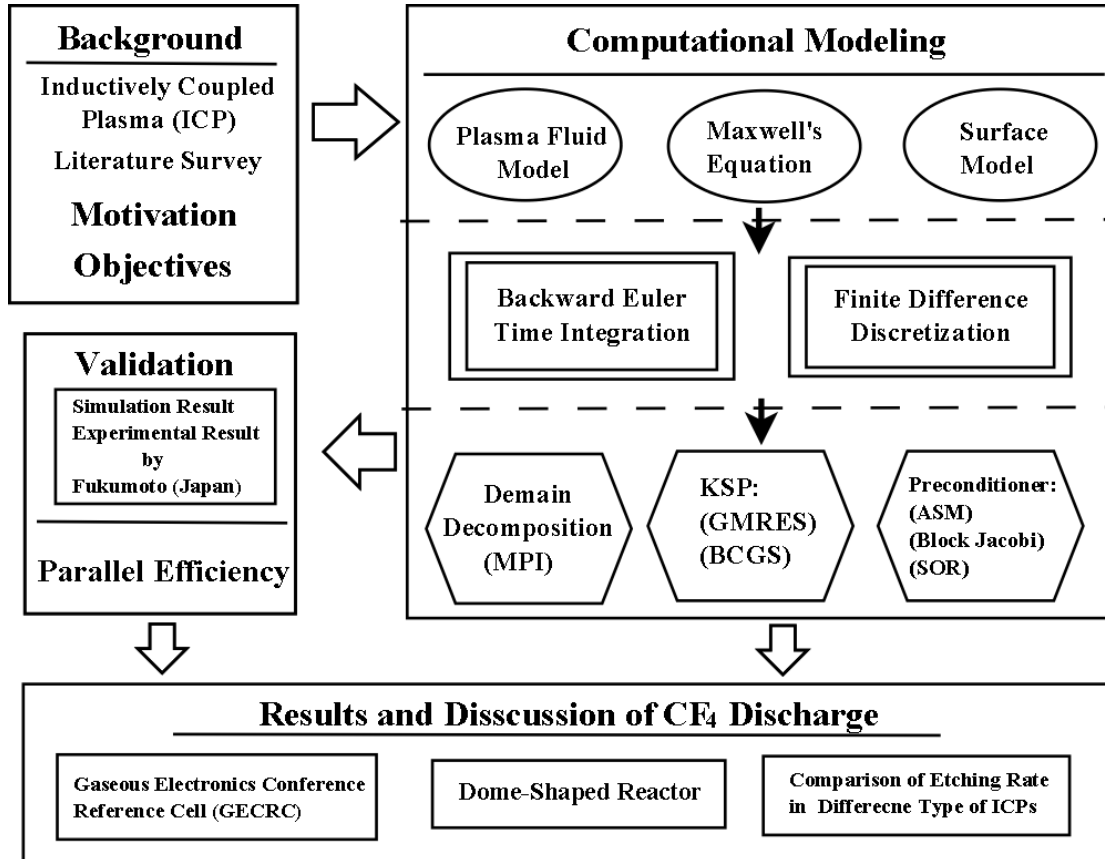
Figure 3: Research framework of this thesis.
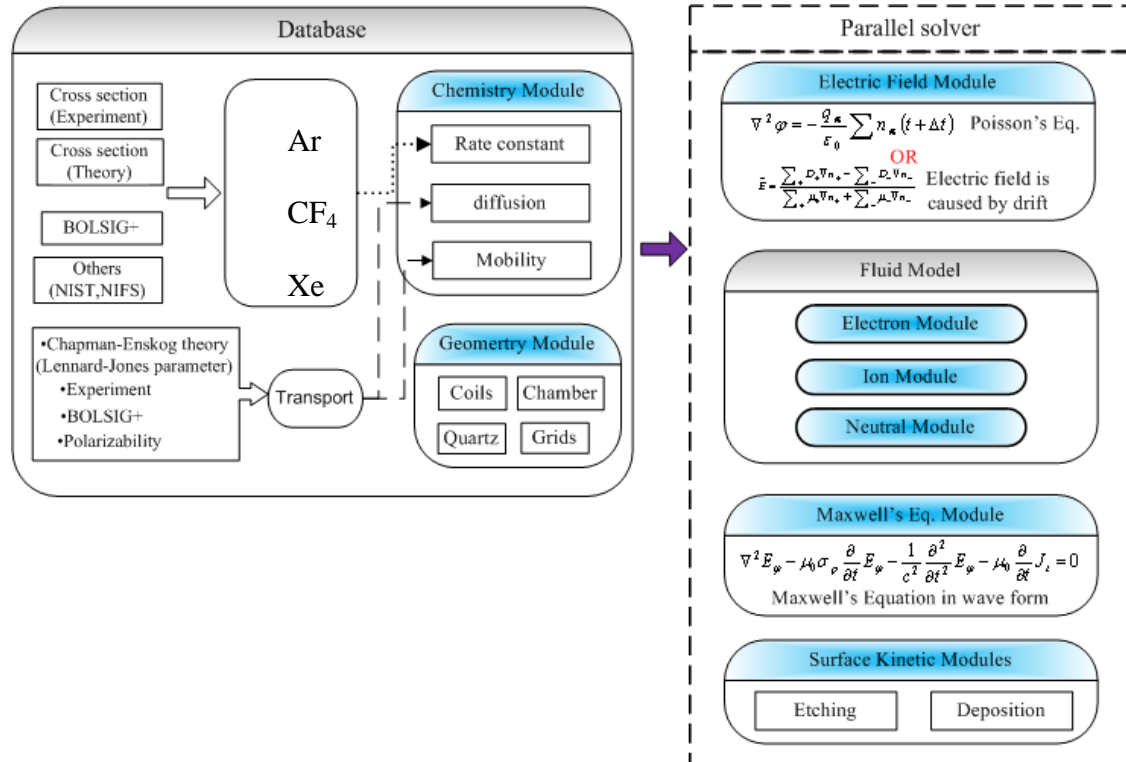
Figure 4: Structure of our developed simulation tools
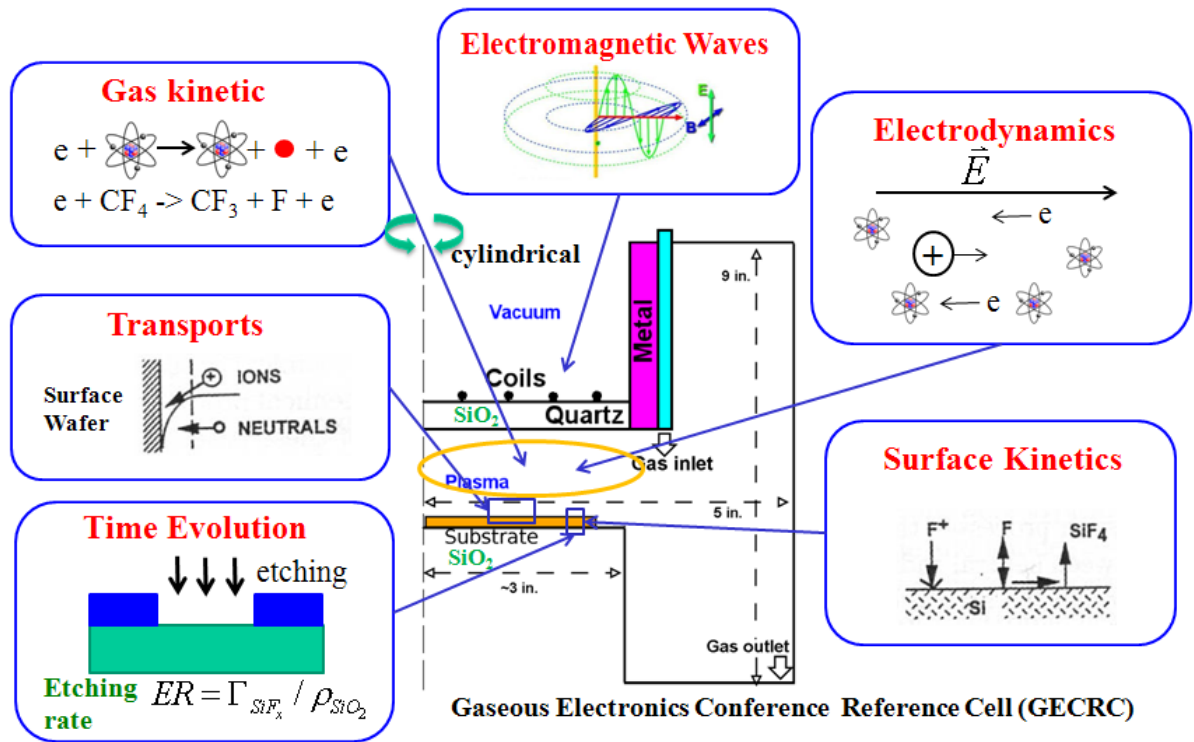
Figure 5: Schematic of dominant processes in a CF$_4$ discharge for etching process
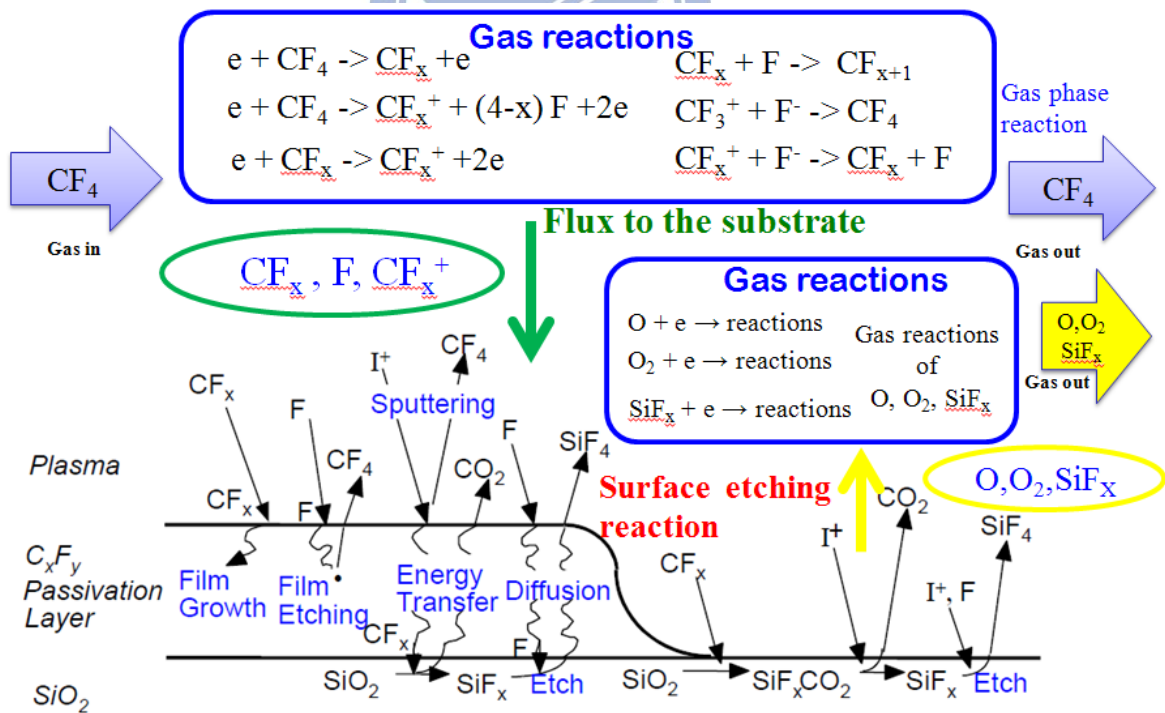
Figure 6: Summary of CF$_4$ gas-phase reactions and surface reactions

Start

Electric field from ambipolar diffusion

$$\vec{E}_{r,z} = \frac{\sum_+ D_+ n_+ - \sum_- D_- n_-}{\sum_+ \mu_+ n_+ + \sum_- \mu_- n_-}$$

$\vec{E}(t + \Delta t)$

Continuity equation for ions and neutral

$$\frac{\partial n_I}{\partial t} + \frac{1}{r}\frac{\partial(r\Gamma_r)}{\partial r} + \frac{\partial(\Gamma_z)}{\partial z} = S$$

$$\Gamma_i = n_i \vec{v}_i = -D_i \nabla n_i \pm s_i \mu_i n_i \vec{E}$$

$$\Gamma_\alpha = -D_\alpha \nabla n_\alpha$$

$n_i(t + \Delta t)$
$n_\alpha(t + \Delta t)$

Electron concentration

$$\sum_+ n_+ = \sum_- n_- \qquad \sum_+ \Gamma_+ = \sum_- \Gamma_-$$

$n_e(t + \Delta t)$
$\Gamma_e(t + \Delta t)$

Maxwell equation

$$\begin{cases} \nabla^2 E_R - \mu_0 \omega \sigma_{p,I} E_R + \mu_0 \omega \sigma_{p,R} E_I + \dfrac{\omega^2}{c^2} E_R = 0 \\ \nabla^2 E_I - \mu_0 \omega \sigma_{p,I} E_I - \mu_0 \omega \sigma_{p,R} E_R + \dfrac{\omega^2}{c^2} E_I - \mu_0 \omega J_R = 0 \end{cases}$$

$$\sigma_p = \frac{\varepsilon_0 \omega_{pe}^2}{(\upsilon_m + \omega j)} \quad \omega_{pe} = \sqrt{\frac{e^2 n_e}{\varepsilon_0 m_e}} \quad P_{abs} = \mathrm{Re}\{\tilde{\sigma}\tilde{E}e^{i\omega t}\}\mathrm{Re}\{\tilde{E}e^{i\omega t}\}$$

P_{abs}

Energy equation for electron

$$\frac{\partial}{\partial t}\left(\frac{3}{2}n_e T_e\right) + \nabla \cdot Q = -e\vec{\Gamma}_e \cdot \vec{E} - \varepsilon_{loss} + P_{ind}$$

$$Q_{i,j} = \frac{5}{2}T_e \vec{\Gamma}_{e(i,j)} - \frac{5}{2}n_e D_e \nabla T_e$$

$T_e(t + \Delta t)$

Surface site balance

$$\theta_F, \theta_{CFx}, \theta_P, \theta_{F/P}, \theta_{CFx/P}$$

Rate coefficient & transport

$$K_e(t + \Delta t), D_e(t + \Delta t), \mu_e(t + \Delta t)$$

Quasi-steady solutions

Figure 7: Flow diagram of solving fluid model coupled with Maxwell's equation and surface kinetic model
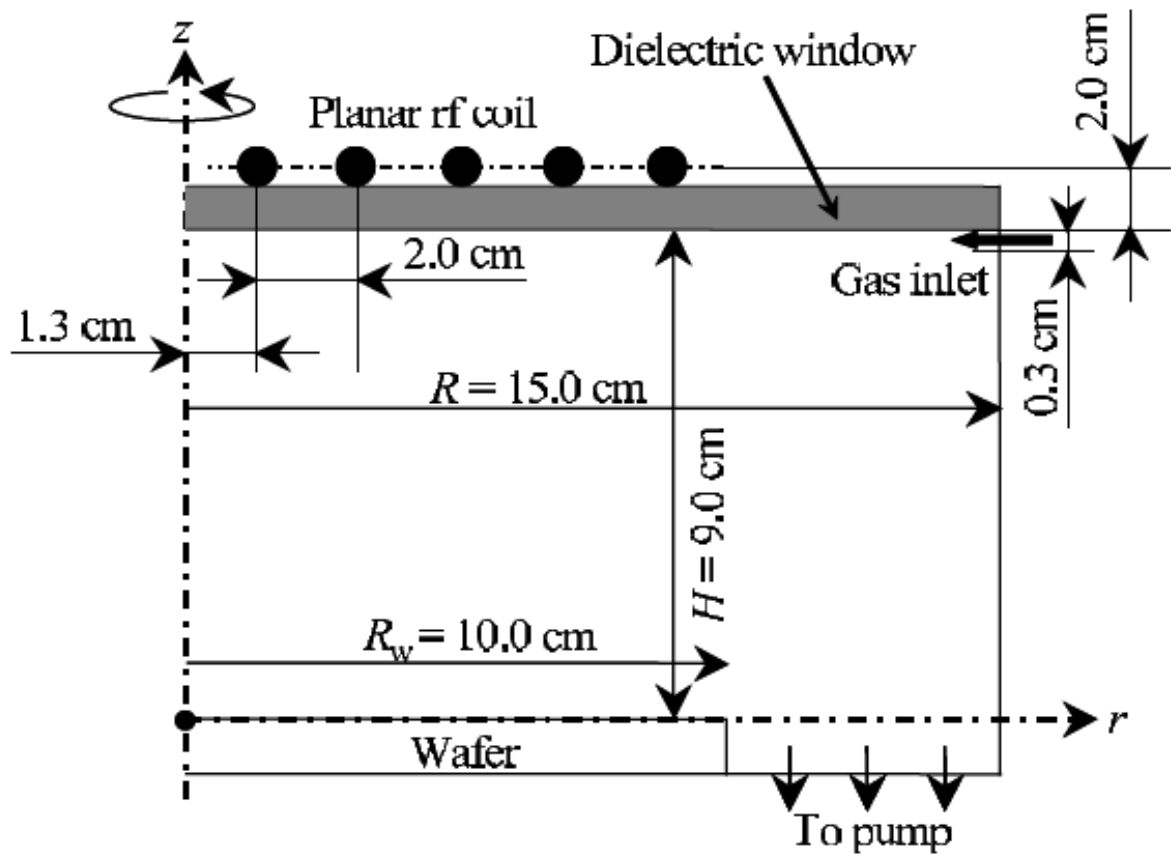
Figure 8: Schematic of the typical ICP reactor was applied in CF4 plasma by H. Fukumoto *et al.* [26].
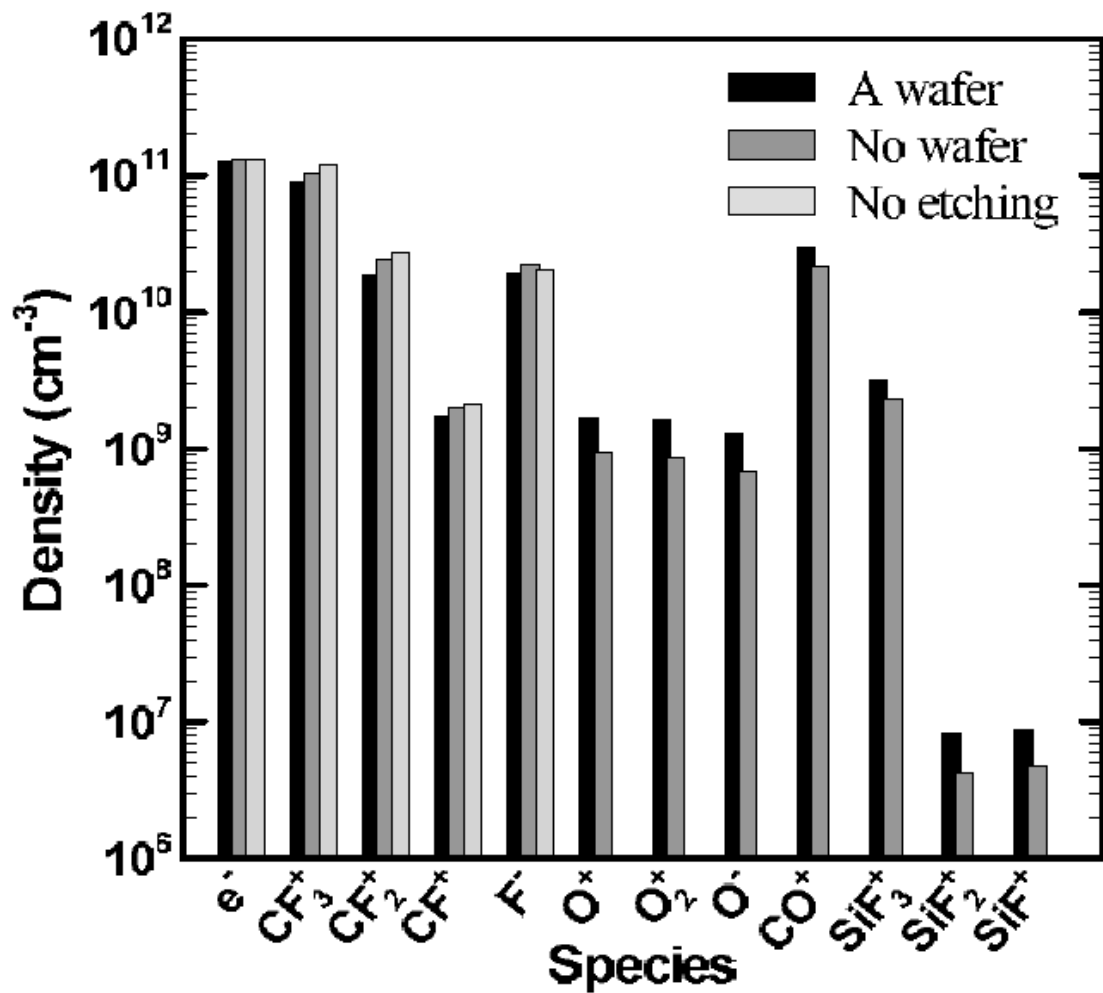
Figure 9: **Chemical compositions of charged species averaged over the entire region of the reactor chamber in three cases of 'a wafer', 'no wafer' and 'no etching' [26].**
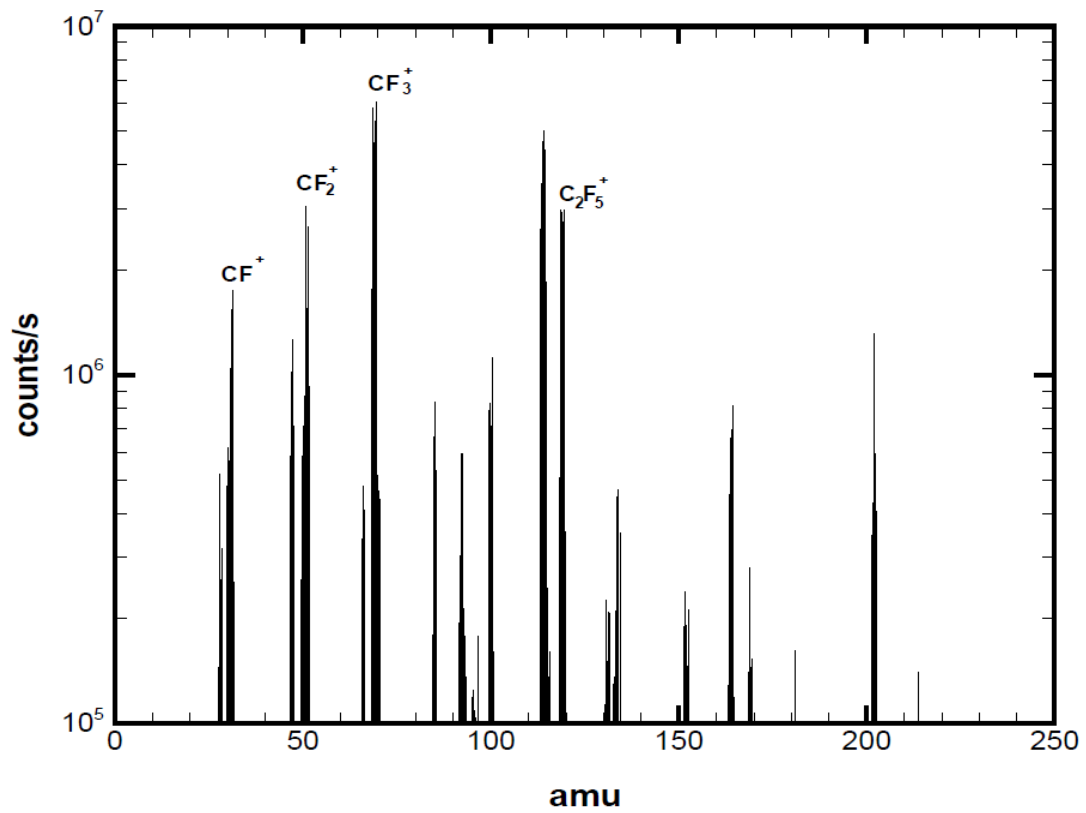
Figure 10: Mass spectrum done by Fukumoto *et al.* [74] for ICP CF4 plasmas at a pressure of 20 mTorr, and an ICP power of 280 W.
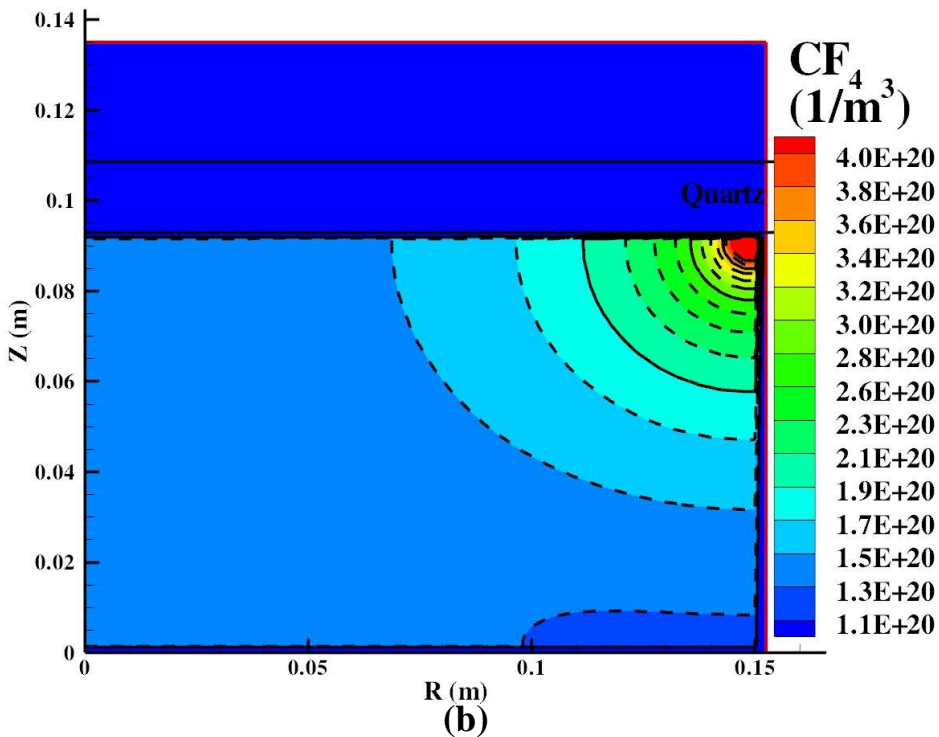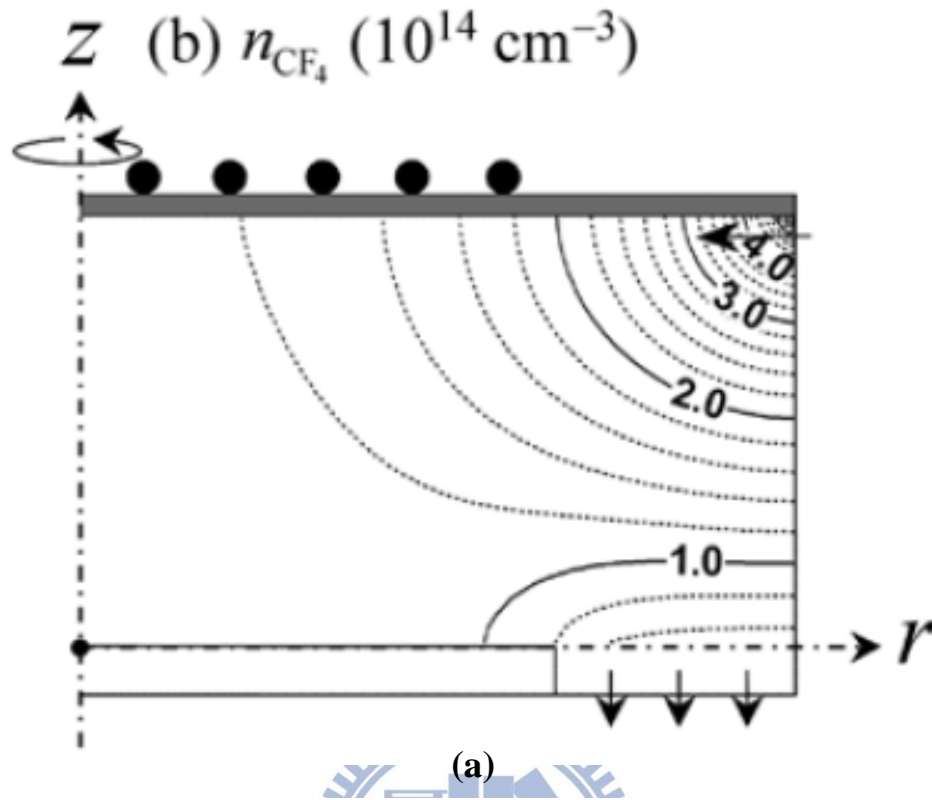
Figure 11: Two-dimensional distributions of CF₄ density (a) done by Fukumoto *et al.* [26] (b) our validation under the standard conditions: a gas pressure of 10mTorr, a feedstock CF4 flow rate of 200 sccm, a total power deposition of 250W and an ion bombardment energy of 100 eV on substrate surfaces of temperatureTs = 300 K.
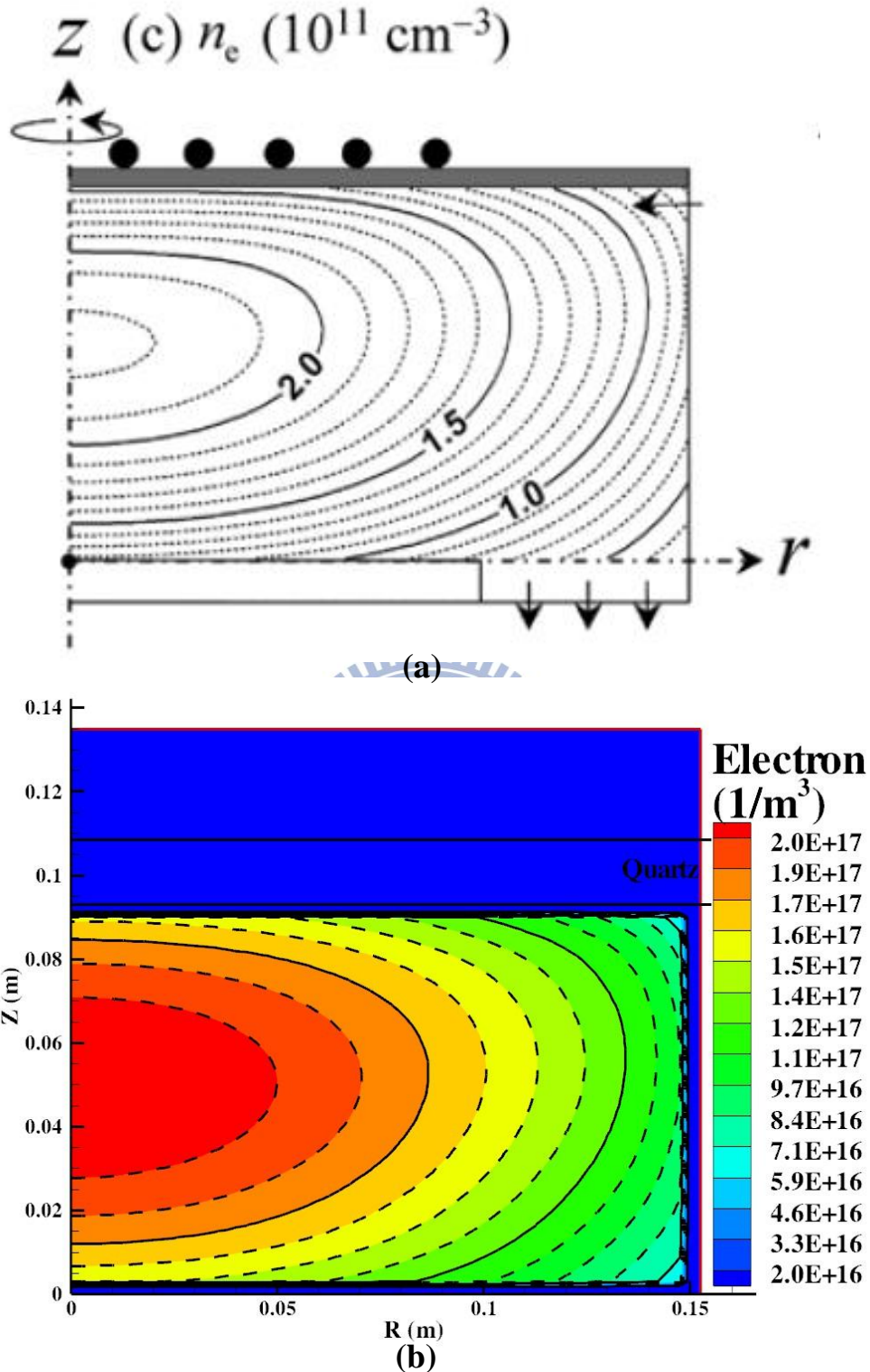
Figure 12: Two-dimensional distributions of electron density (a) Fukumoto *et al.*
[26] (b) our simulating result under the standard conditions: a gas
pressure of 10mTorr, a feedstock CF4 flow rate of 200 sccm, a total
power deposition of 250W and an ion bombardment energy of 100 eV
on substrate surfaces of temperatureTs = 300 K.
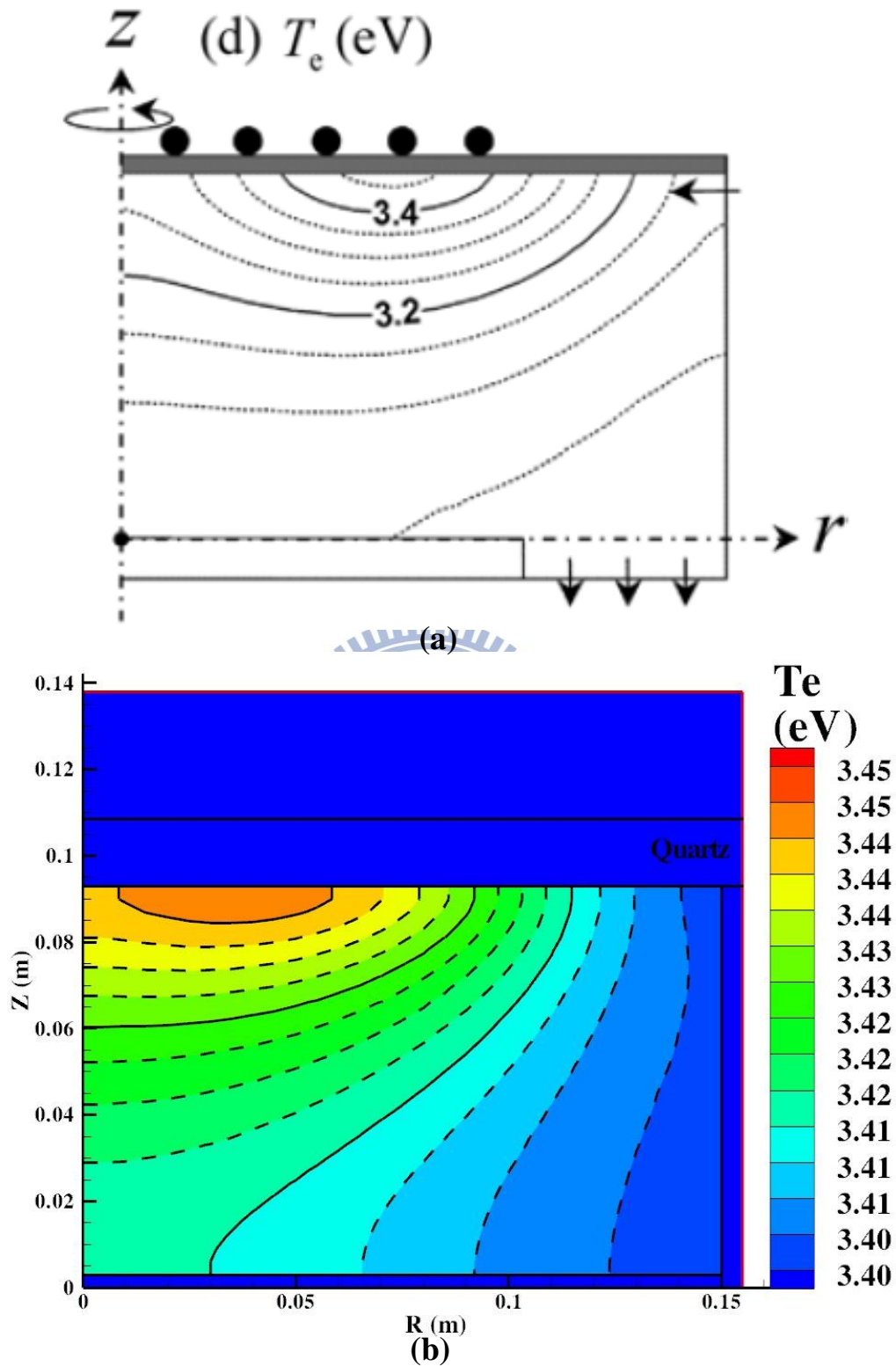
Figure 13: Two-dimensional distributions of Te (a) Fukumoto _et al._ [26] (b) our simulating result under the standard conditions: a gas pressure of 10mTorr, a feedstock CF4 flow rate of 200 sccm, a total power deposition of 250W and an ion bombardment energy of 100 eV on substrate surfaces of temperatureTs = 300 K.
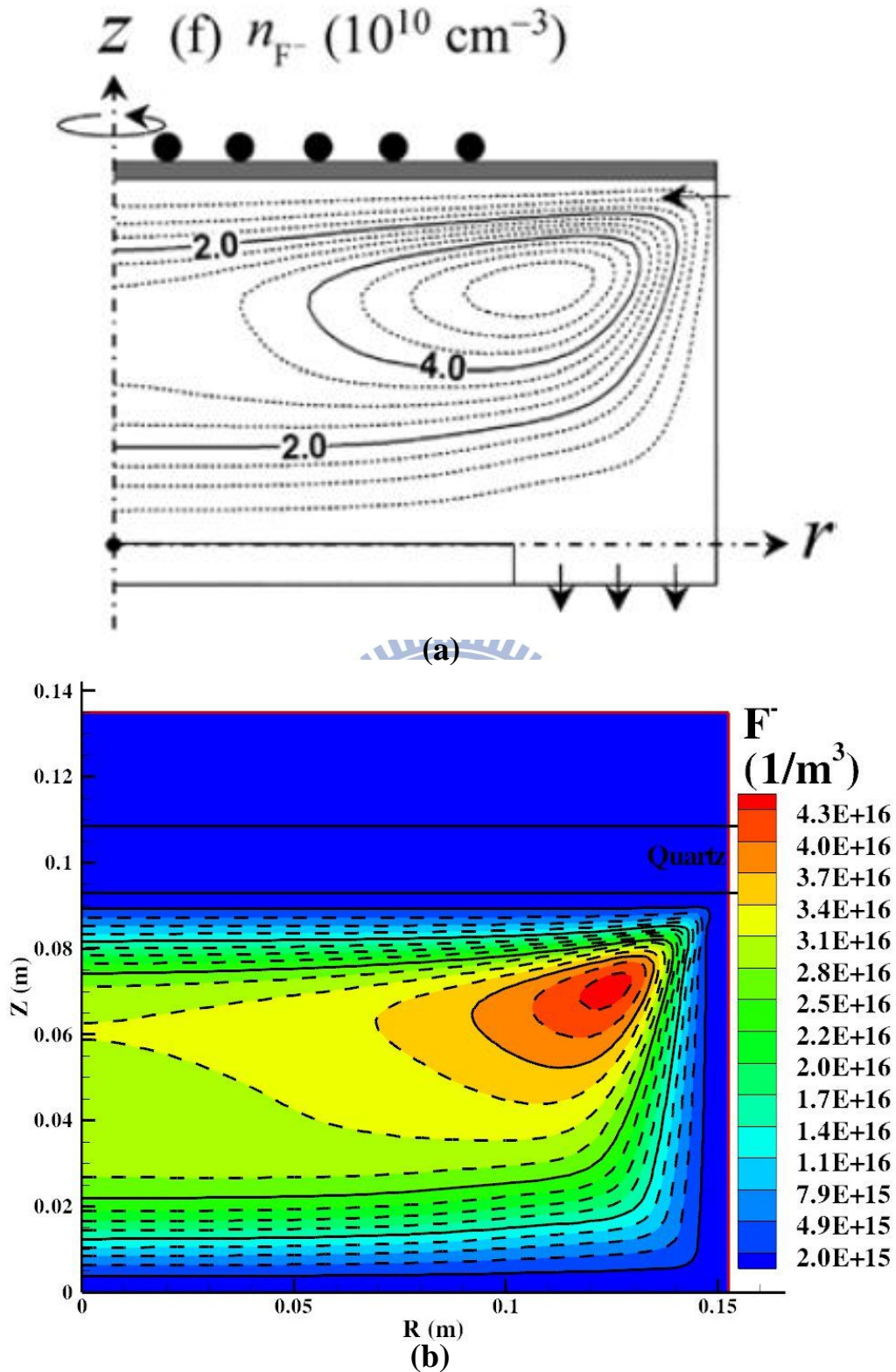
Figure 14: Two-dimensional distributions of F⁻ density (a) Fukumoto *et al.* [26] (b) our simulating result under the standard conditions: a gas pressure of 10mTorr, a feedstock CF4 flow rate of 200 sccm, a total power deposition of 250W and an ion bombardment energy of 100 eV on substrate surfaces of temperatureTs = 300 K.
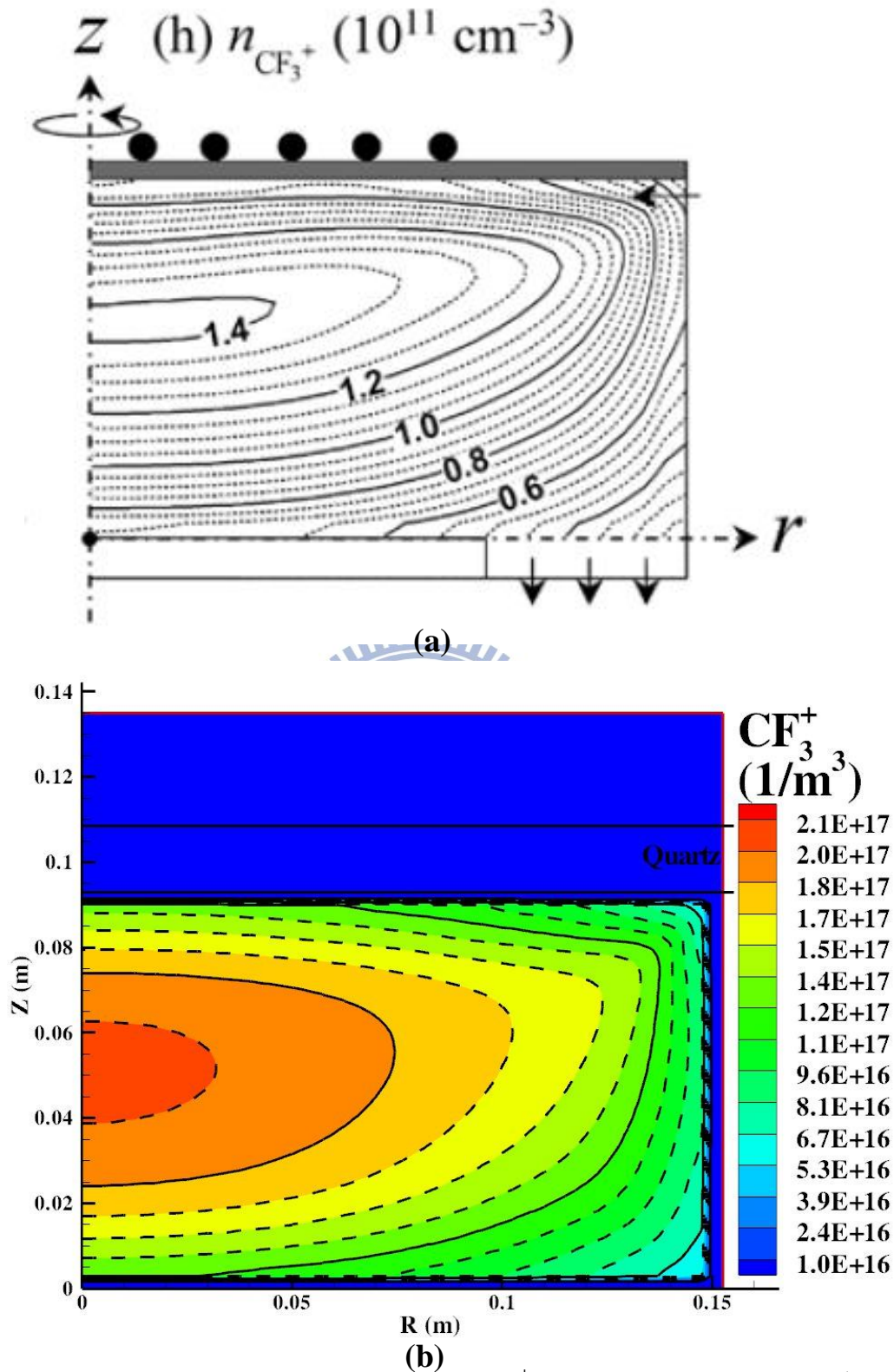
Figure 15: Two-dimensional distributions of CF$_3^+$ density (a) Fukumoto *et al.* [26] (b) our simulating result under the standard conditions: a gas pressure of 10mTorr, a feedstock CF4 flow rate of 200 sccm, a total power deposition of 250W and an ion bombardment energy of 100 eV on substrate surfaces of temperatureTs = 300 K.
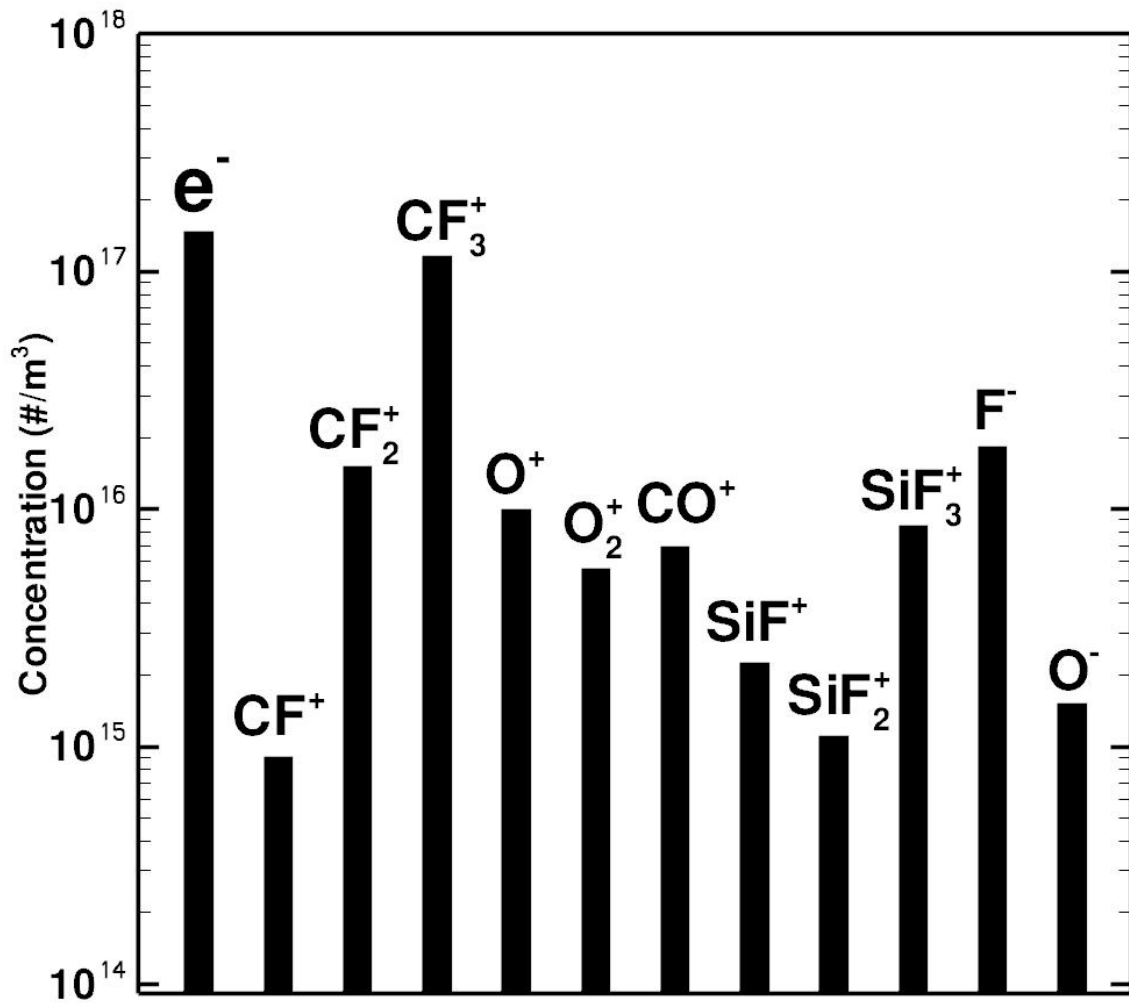
Figure 16: Results validation and comparison to the experiment by Fukumoto *et al*. [26] via bar chart for chemical compositions of ion species averaged over the entire region.
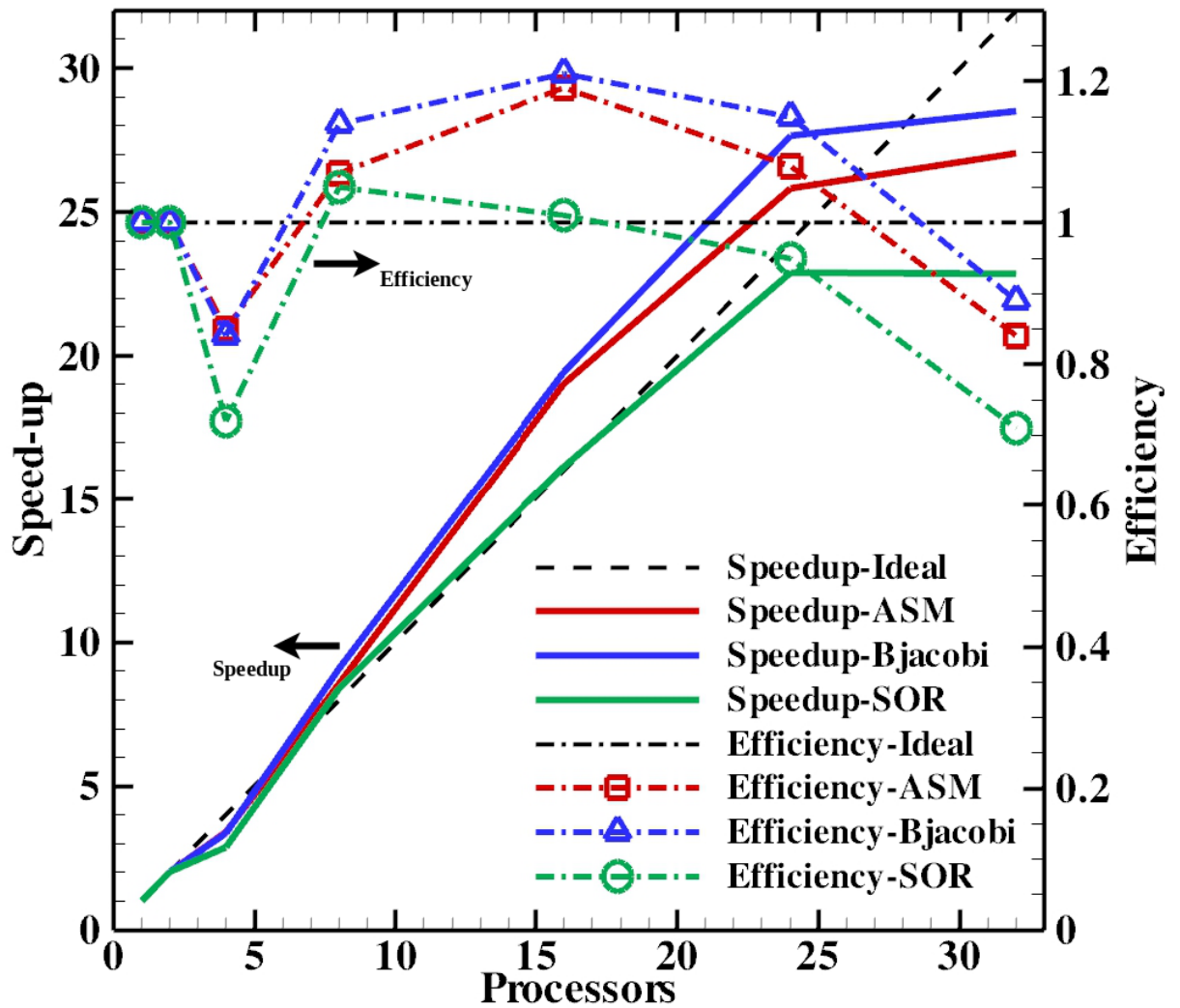
Figure 17: Increased speed and parallel efficiency as a function of processor with preconditioners of ASM, Block Jacobi, SOR based on the matrix solver of GMRES.
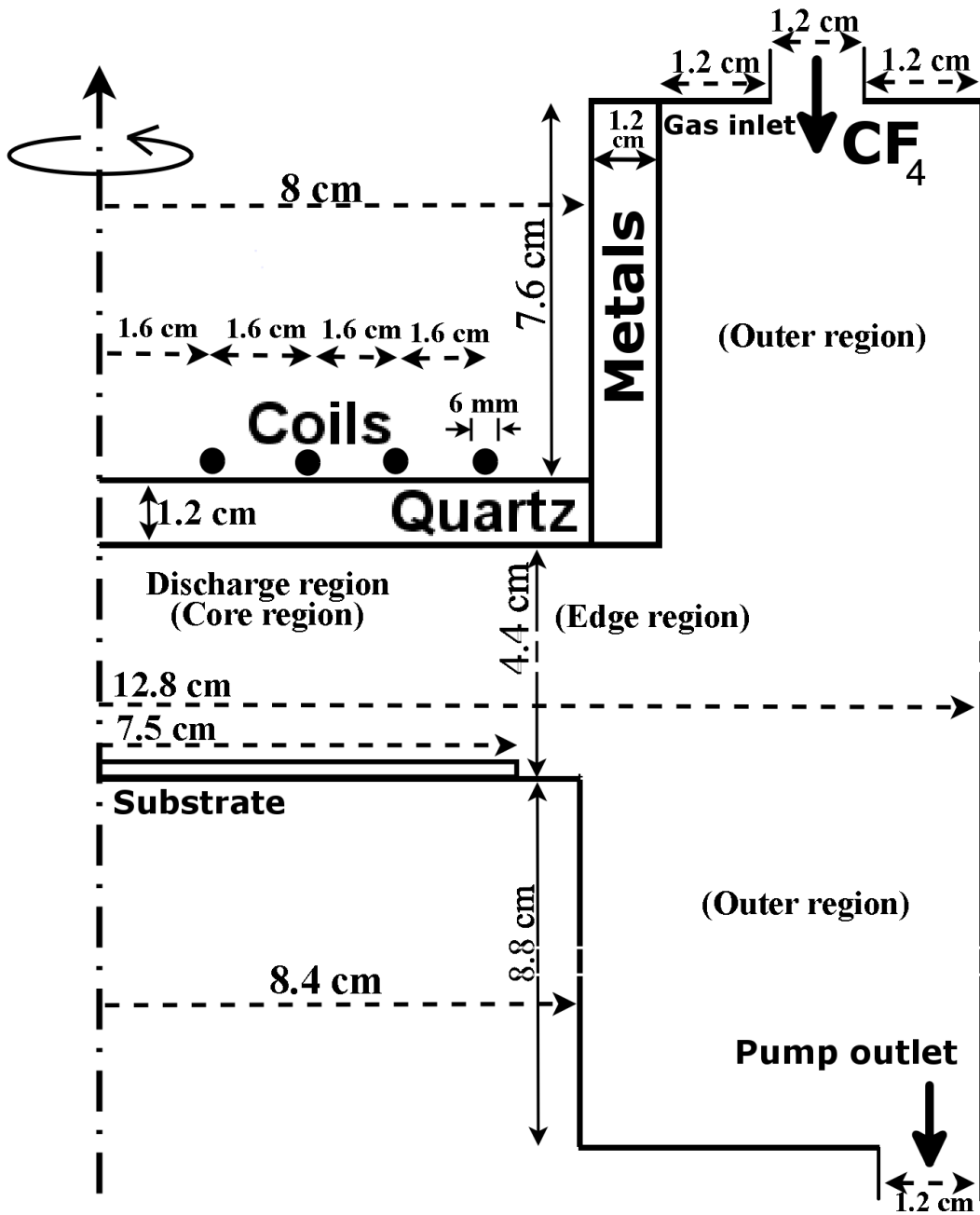
Figure 18: Schematics of the cylindrical gaseous electronics conference reference cell (GECRC) reactor for etching SiO₂.
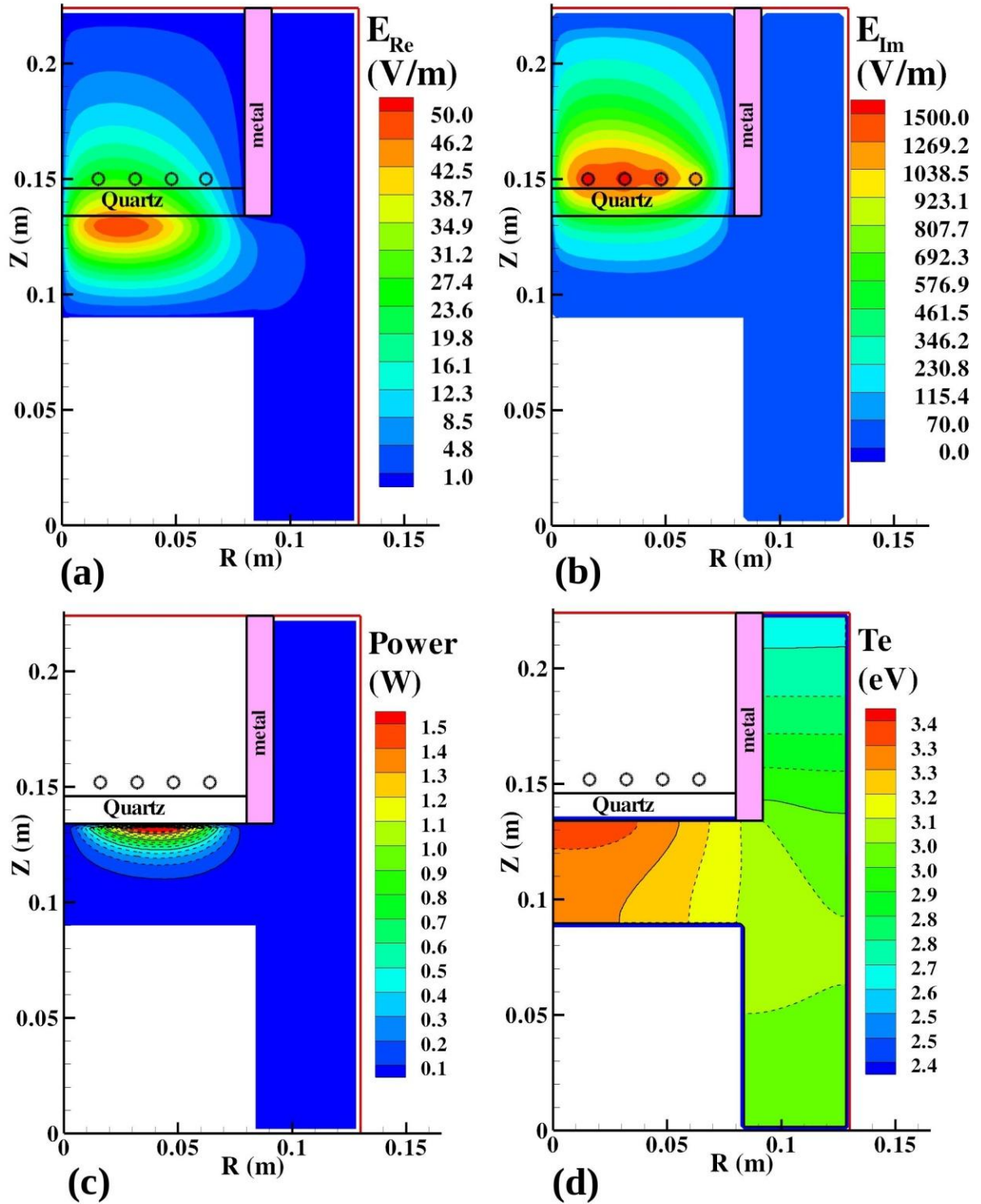
Figure 19: Two-dimensional contour of (*a*) the real part of the induced electric field, (*b*) the imaginary part of the induced electric field, (*c*) the electron temperature T_e and (*d*) the power density at a power absorption of 150 W and a pressure of 30 mTorr.
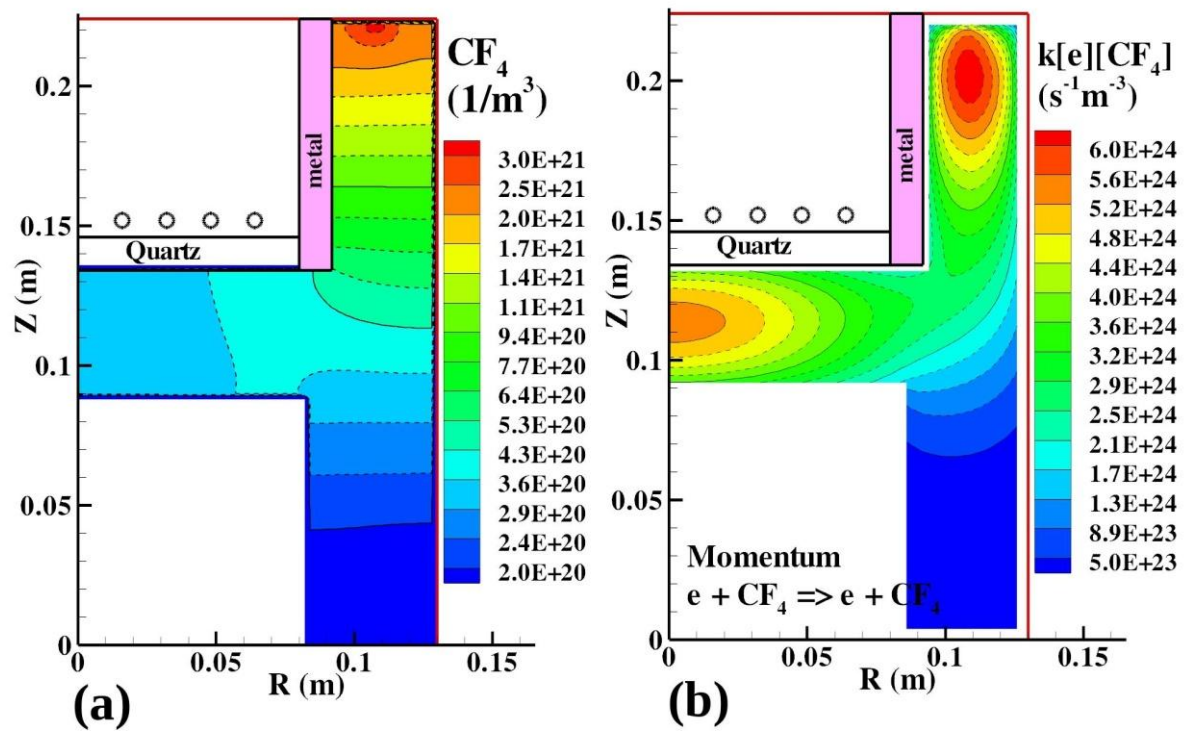
Figure 20: Two-dimensional contour of (*a*) the feeding gas CF_4 in a unit of m^{-3} and (*b*) the production rate for momentum transfer reaction (F00) in unit of $m^{-3}s^{-1}$ at a power absorption of 150 W and a pressure of 30 mTorr.
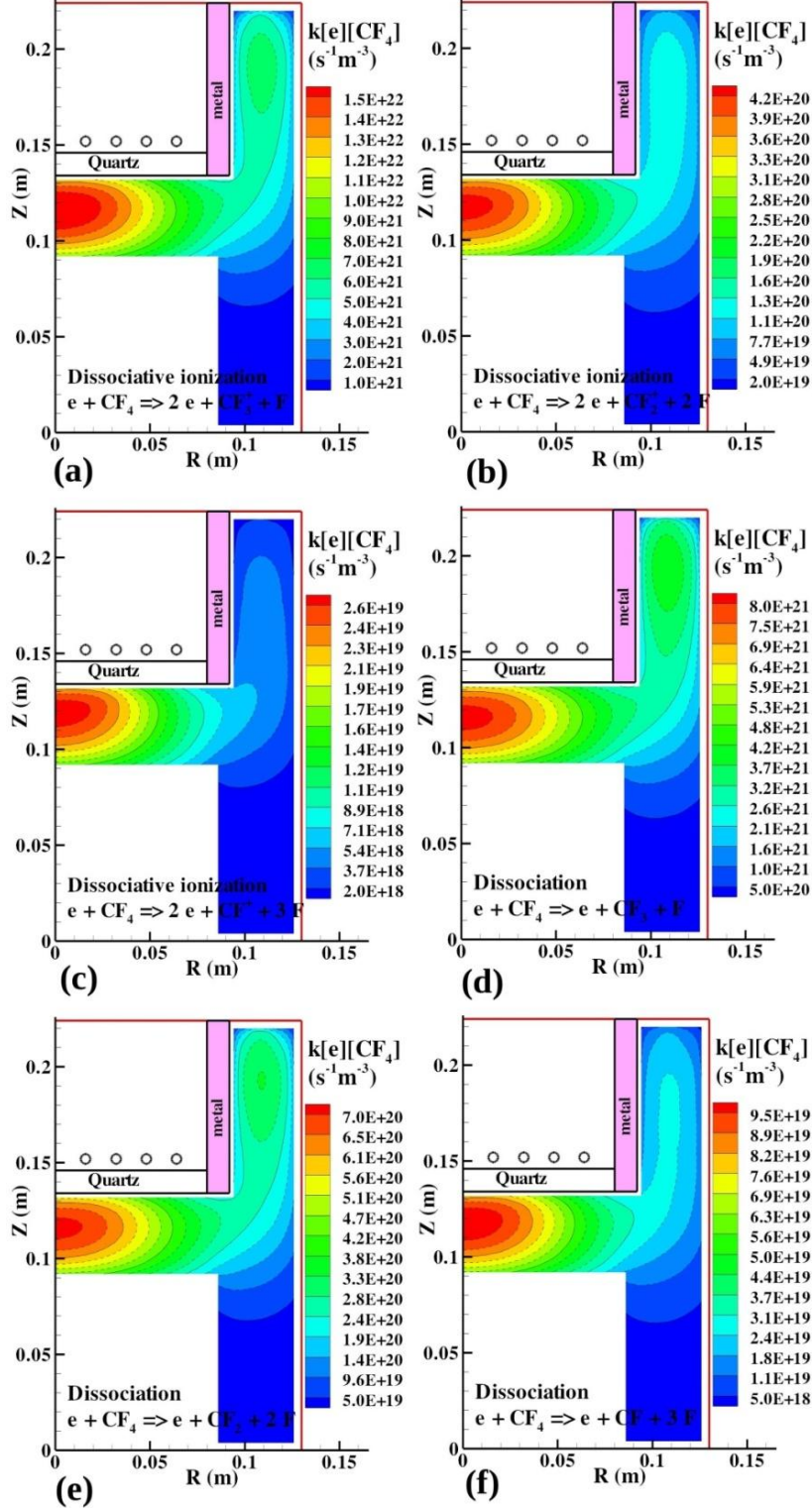
Figure 21: **Two-dimensional contour of the production rate (m^{-3}s^{-1}) of (*a*) dissociative ionization** e + CF$_4$ → CF$_3^+$ + F + 2e **(F05), (*b*) dissociative ionization** e + CF$_4$ → CF$_2^+$ + 2F + 2e **(F06), (*c*) dissociative ionization** e + CF$_4$ → CF$^+$ + 3F + 2e **(F07), (*d*) dissociation** e + CF$_4$ → CF$_3$ + F + e **(F11), (*e*) dissociation** e + CF$_4$ → CF$_2$ + 2F + e **(F12) and (*f*) dissociation** e + CF$_4$ → CF + 3F + e **(F13) at a power absorption of 150 W and a pressure of 30 mTorr.**
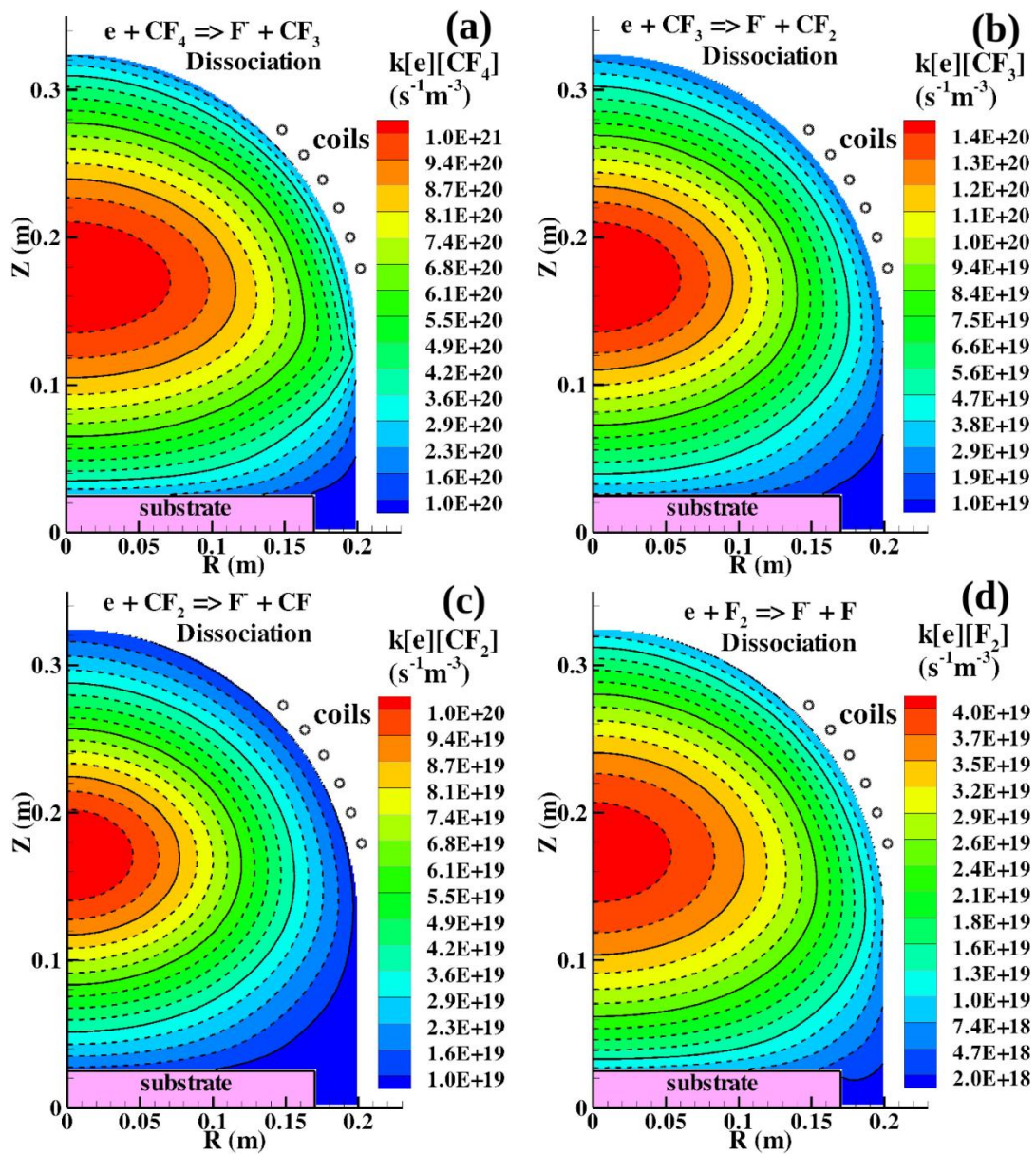
129
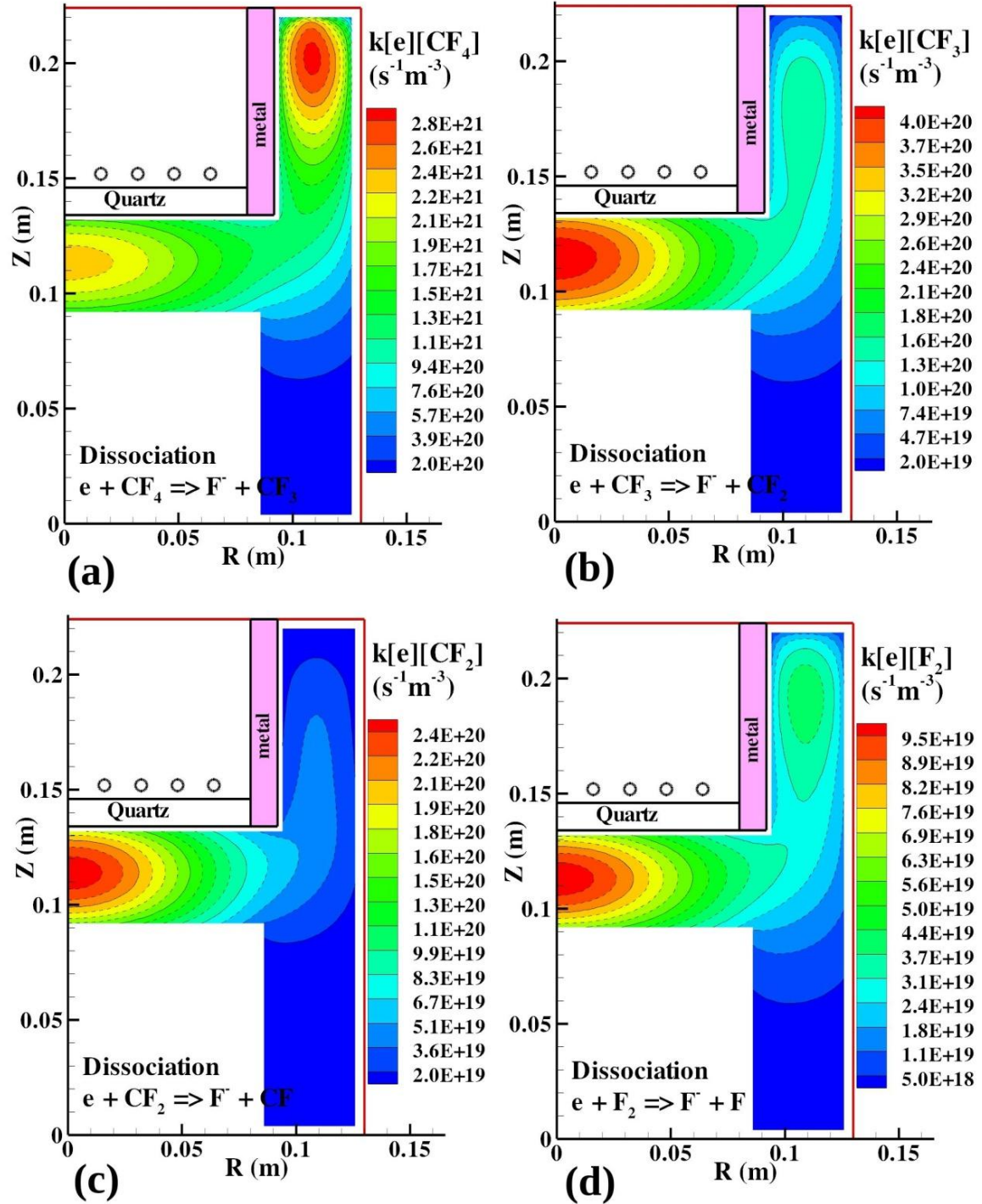
Figure 22: Two-dimensional contour of the production rate $(m^{-3}s^{-1})$ of (*a*) dissociative attachment $e + CF_4 \rightarrow CF_3 + F^-$ (**FN01**), (*b*) dissociative attachment $e + CF_3 \rightarrow CF_2 + F^-$ (**FN02**), (*c*) dissociative attachment $e + CF_2 \rightarrow CF + F^-$ (**FN03**) and (*d*) dissociative attachment $e + F_2 \rightarrow F + F^-$ (**FN04**) at a power absorption of 150 W and a pressure of 30 mTorr.

130
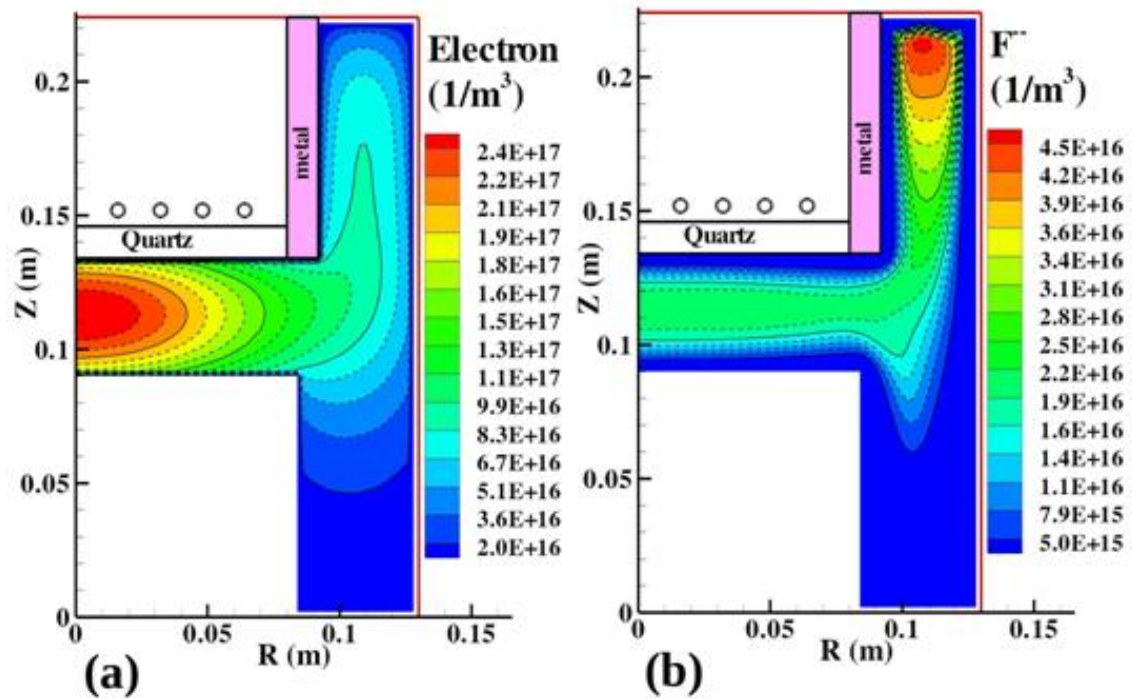
Figure 23: Two-dimensional contour of the (a) electron and (b) F⁻ concentrations at a power absorption of 150 W and a pressure of 30 mTorr.
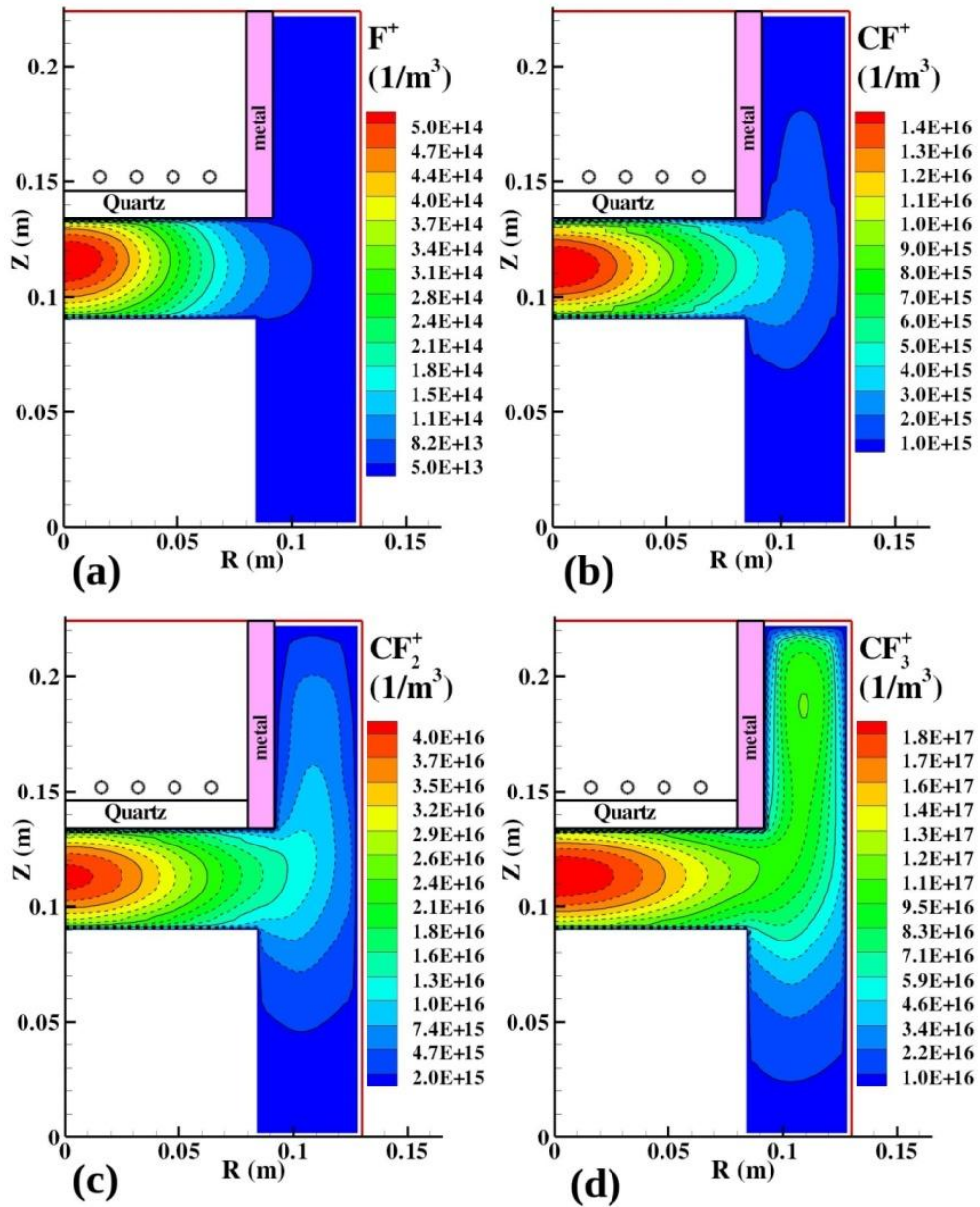
Figure 24: Two-dimensional contour of the (a) F^+, (b) CF^+, (c) CF_2^+ and (d) CF_3^+ concentrations at a power absorption of 150 W and a pressure of 30 mTorr.
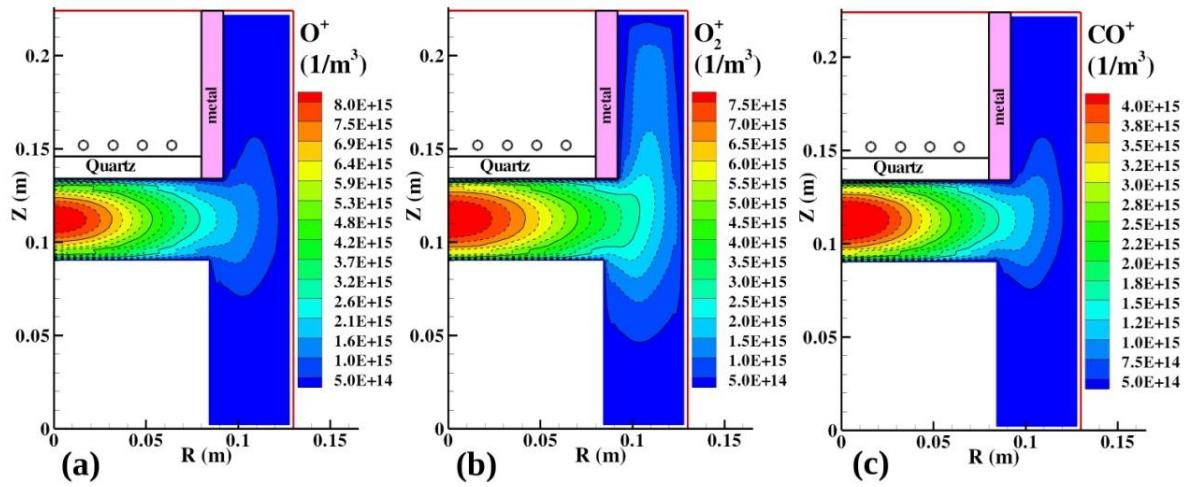
Figure 25: Two-dimensional contour of the (*a*) O^+, (*b*) O_2^+ and (*c*) CO^+ concentrations at a power absorption of 150 W and a pressure of 30 mTorr.
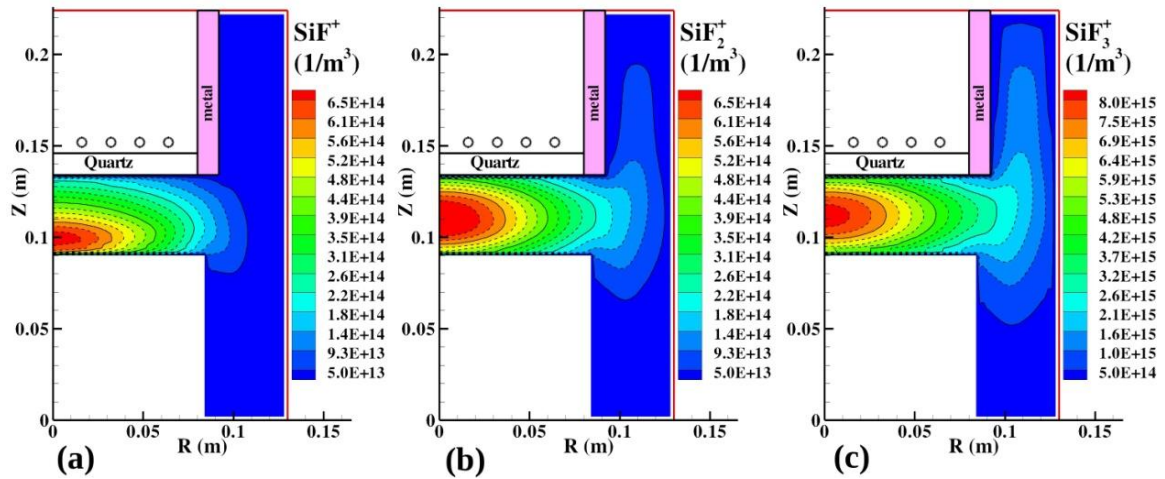
Figure 26: Two-dimensional contour of the (*a*) SiF^+, (*b*) SiF_2^+ and (*c*) SiF_3^+ concentrations at a power absorption of 150 W and a pressure of 30 mTorr.
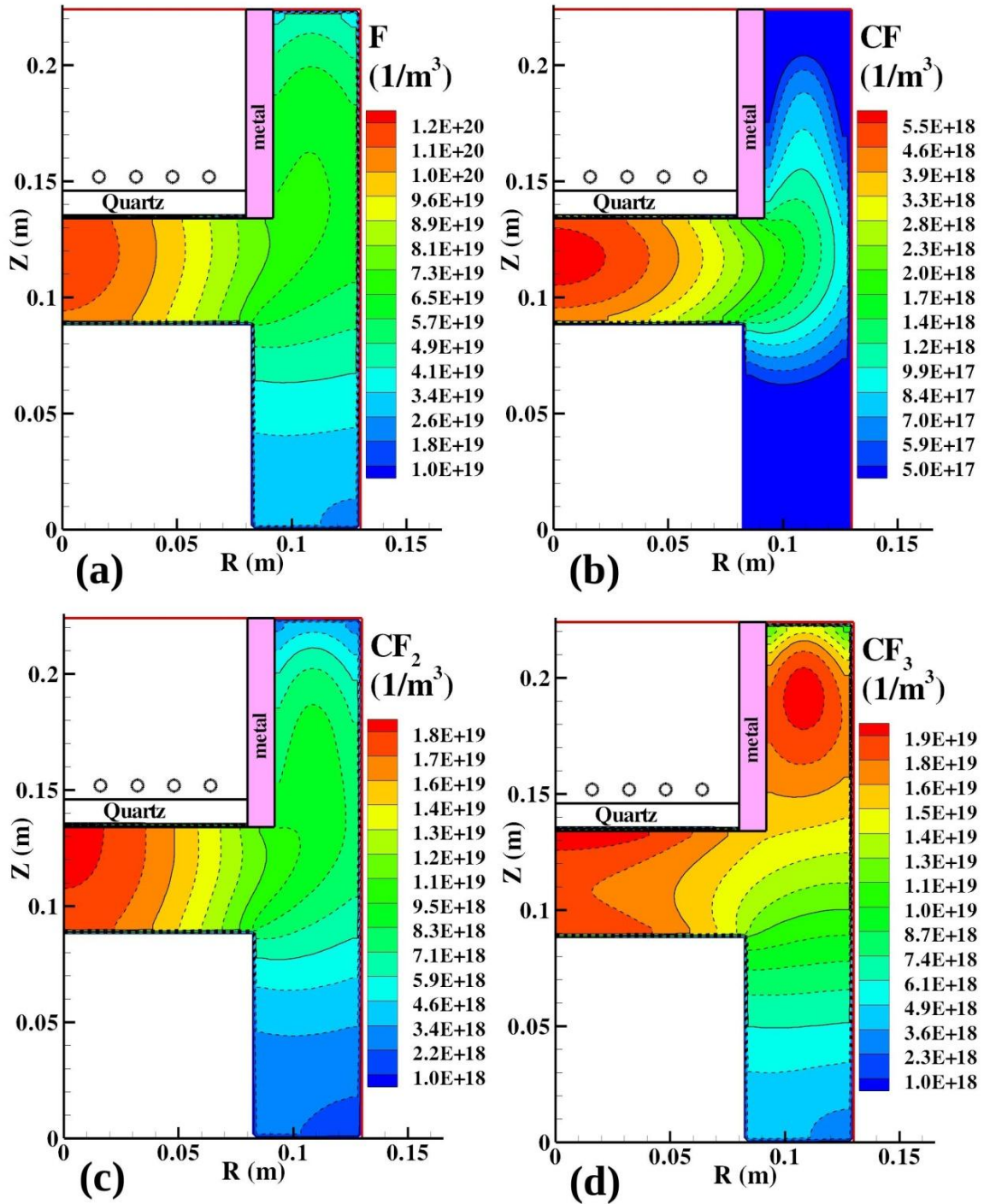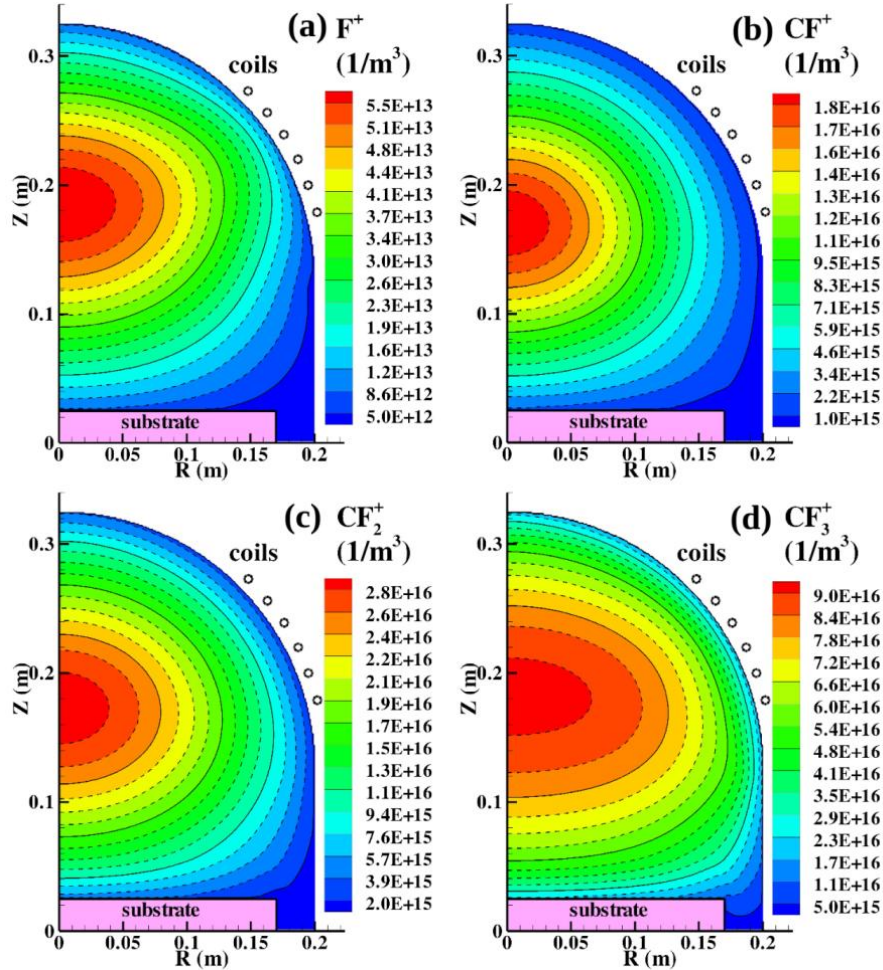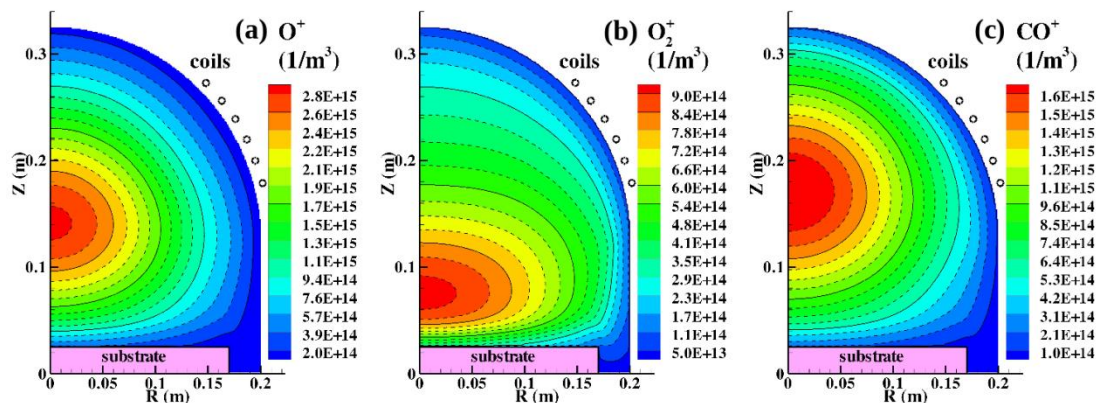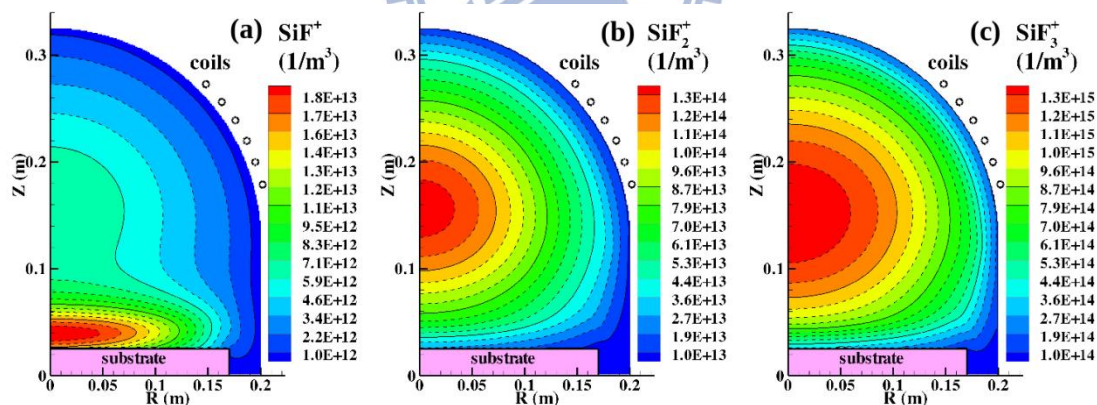
Figure 27: Two-dimensional contour of the (*a*) F, (*b*) CF, (*c*) CF$_2$ and (*d*) CF$_3$ concentrations at a power absorption of 150 W and a pressure of 30 mTorr.
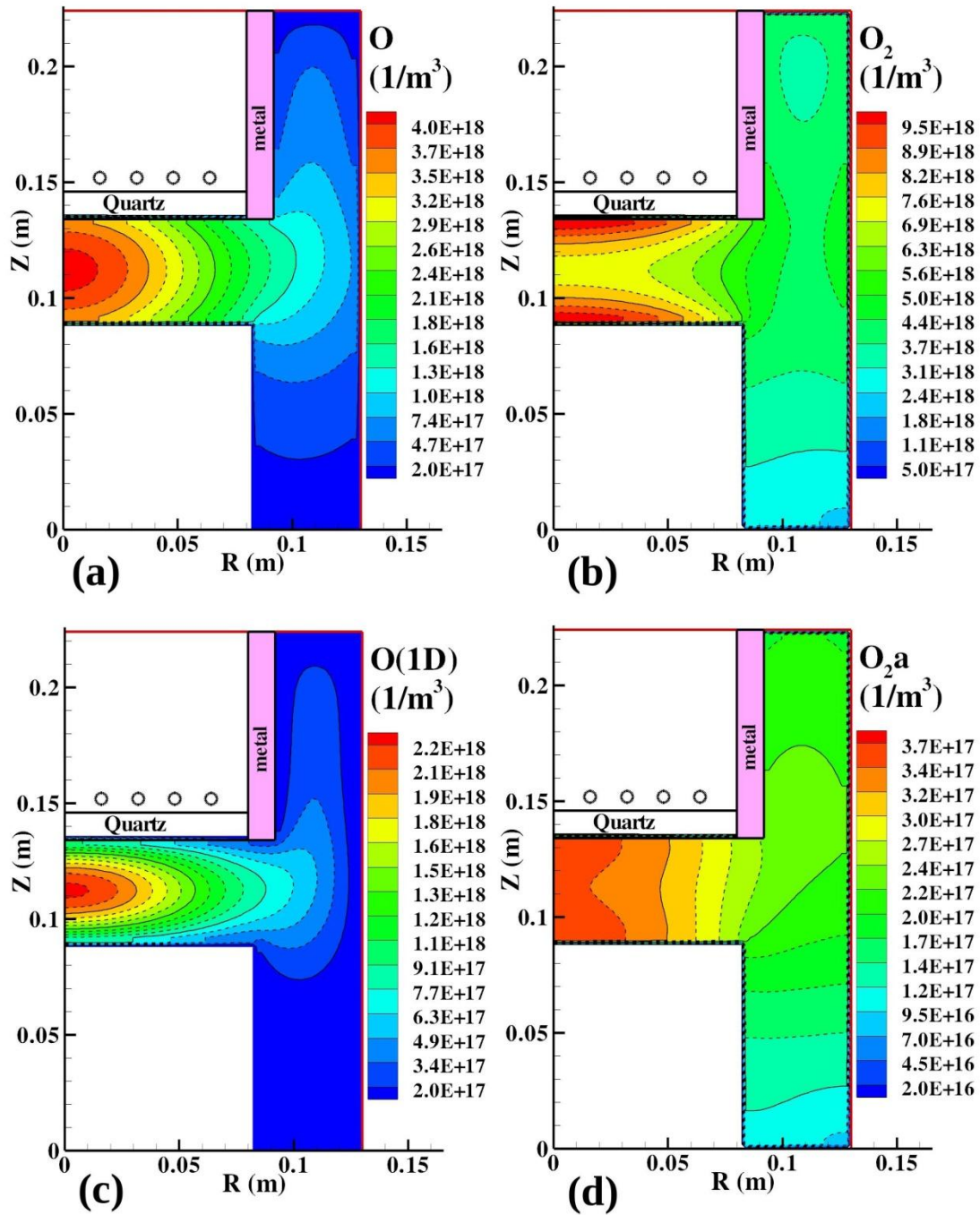
Figure 28: Two-dimensional Contour of (*a*) O, (*b*) O$_2$, (*c*) O(^{1}D) and (*d*) O$_2$(a$^1\Delta_g$) concentrations at a power absorption of 150 W and a pressure of 30 mTorr.
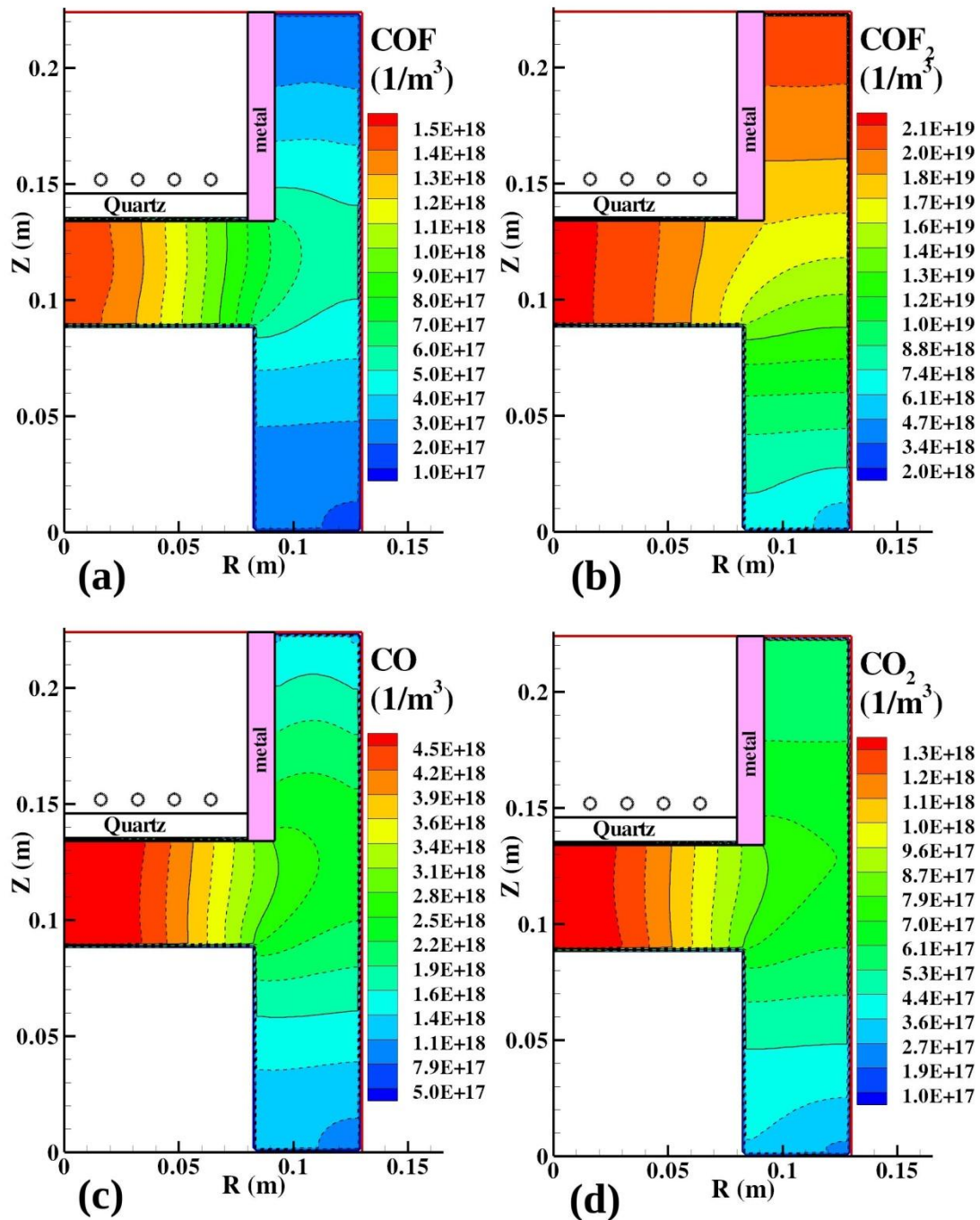
Figure 29: Two-dimensional contour of (*a*) COF, (*b*) COF$_2$, (*c*) CO and (*d*) CO$_2$ concentrations at a power absorption of 150 W and a pressure of 30 mTorr.
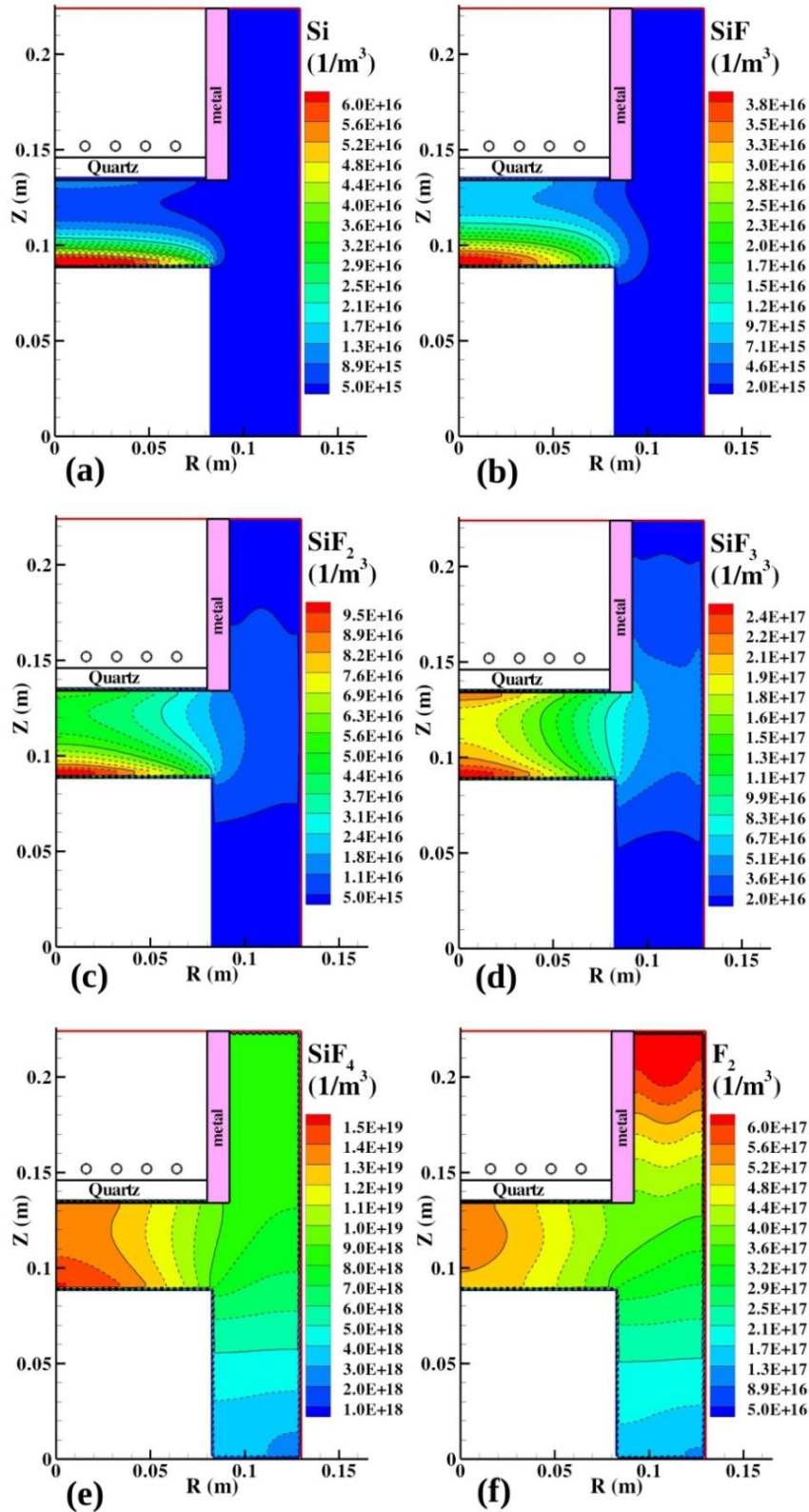
Figure 30: Two-dimensional contour of (*a*) Si, (*b*) SiF, (*c*) SiF_2, (*d*) SiF_3, (*e*) SiF_4 and (*f*) F_2 concentrations at a power absorption of 150 W and a pressure of 30 mTorr.
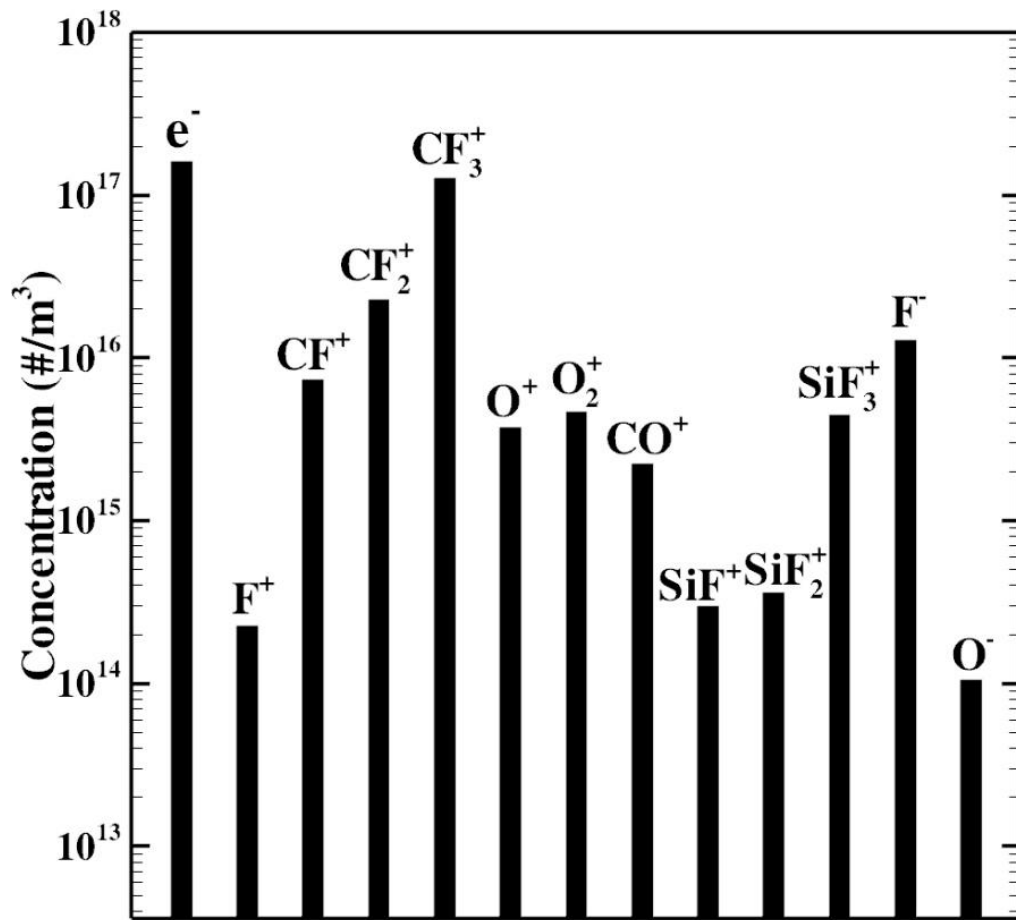
Figure 31: Chemical ingredients of charged species averaged over the core region of the reactor chamber.
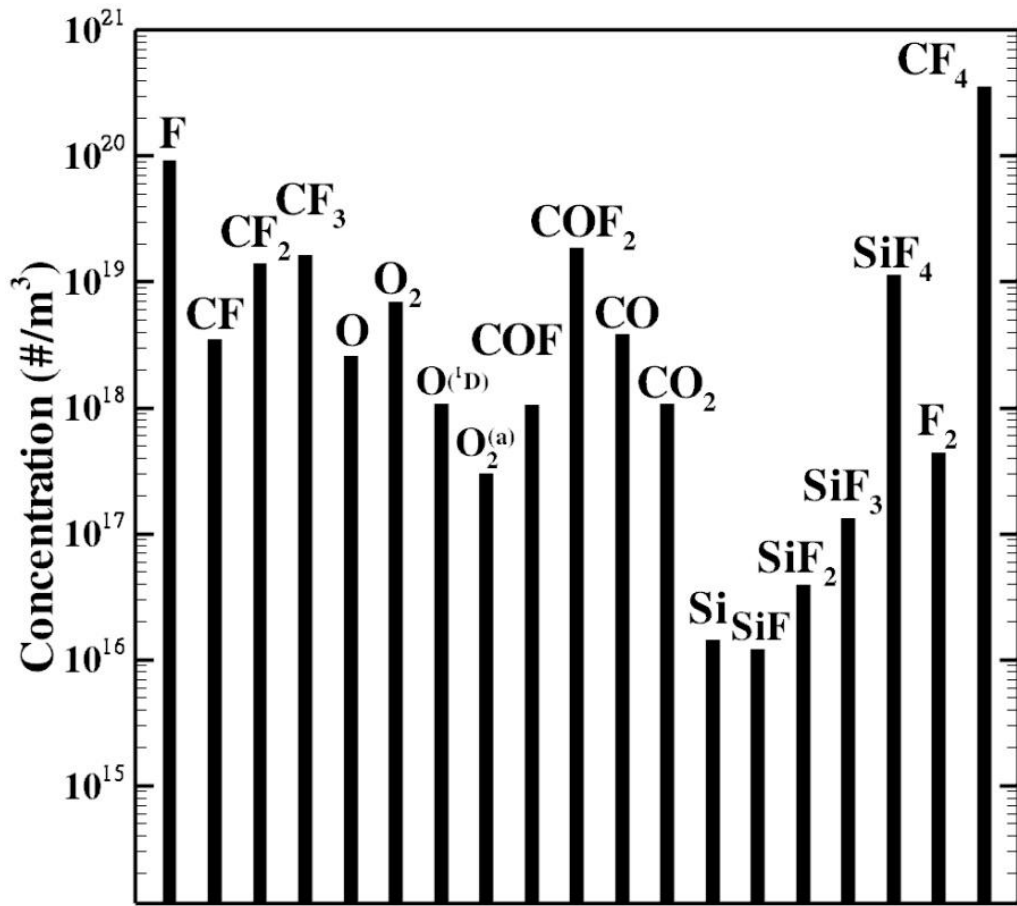
Figure 32: Chemical ingredients of neutral species averaged over the core region of the reactor chamber.
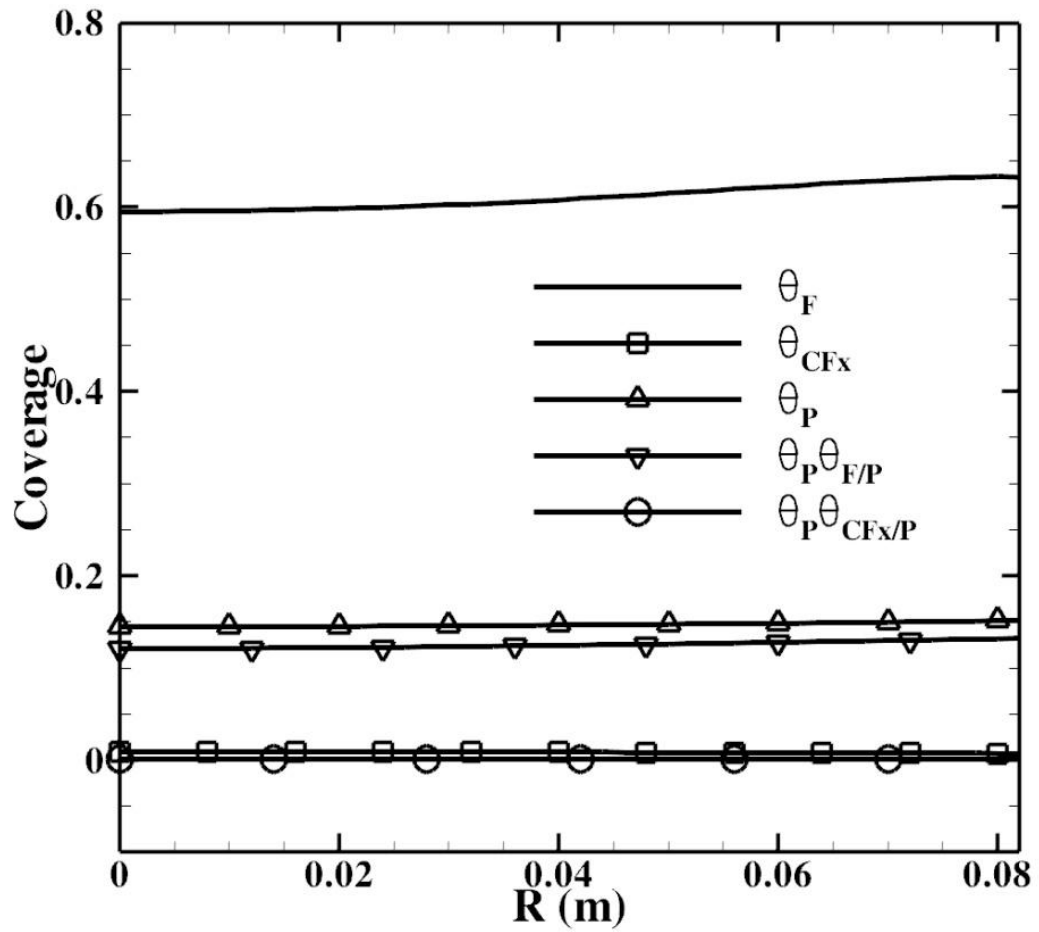
Figure 33: Surface coverages as a function of radial distance on the substrate.
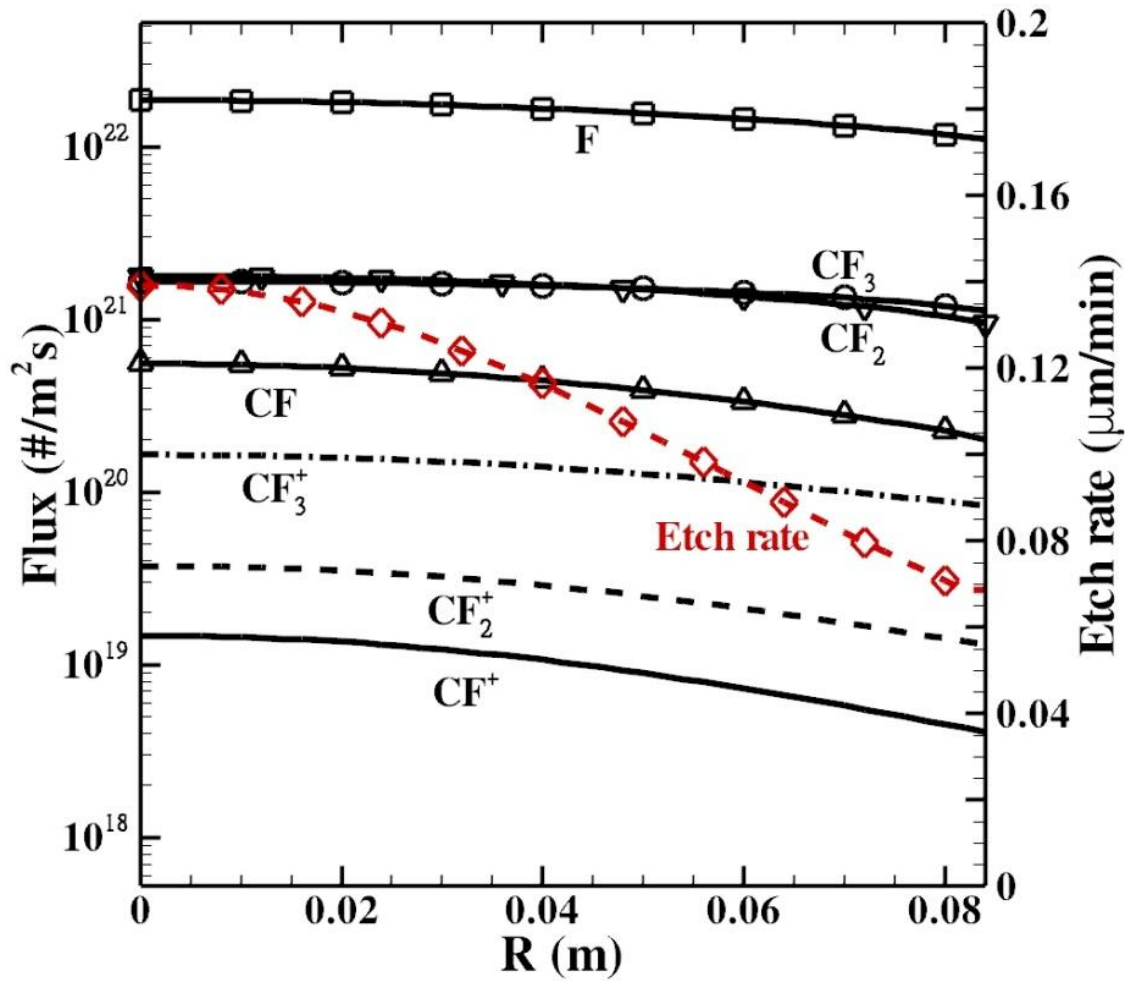
Figure 34: Etch rate, radical fluxes and CF_x^+ ion fluxes as functions of radial distance on the substrate surface.
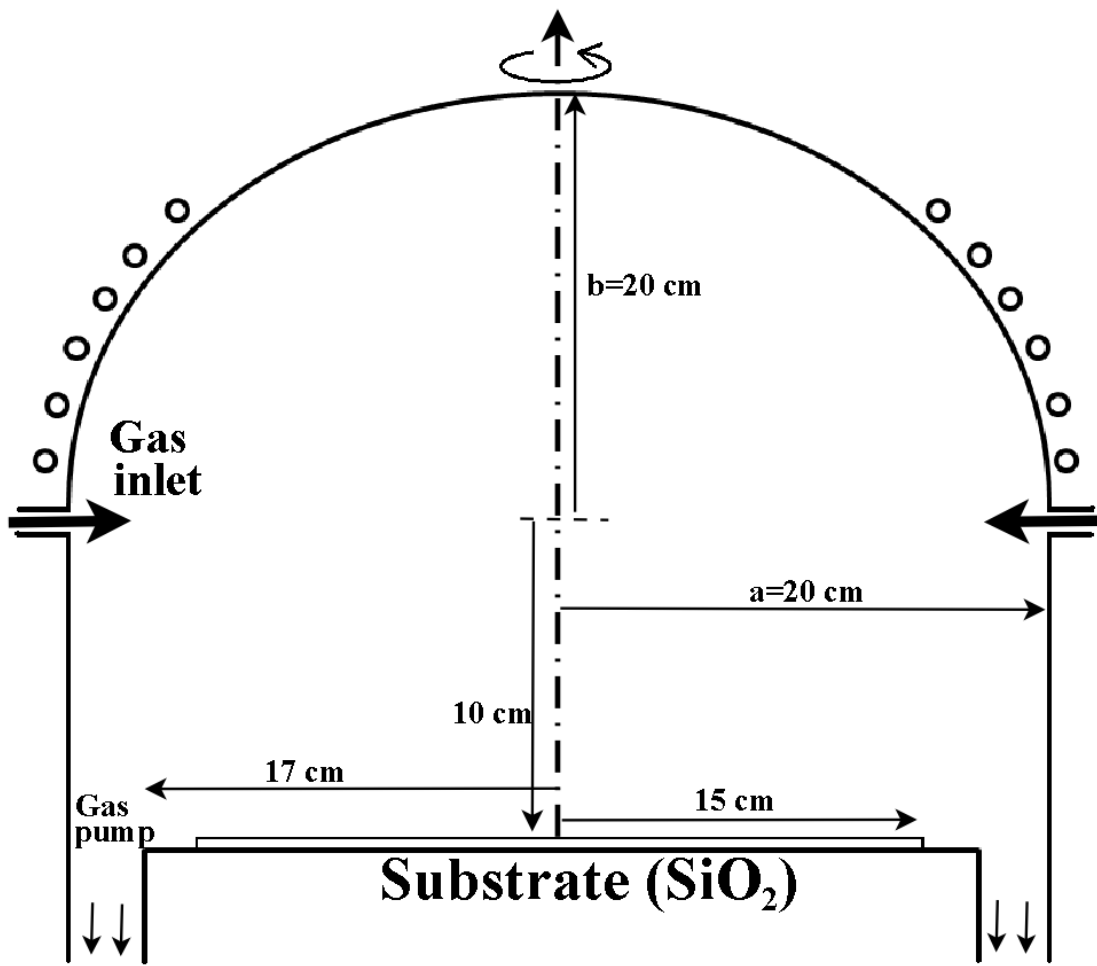
Figure 35: Schematics of the cylindrical dome-shaped reactor for etching SiO₂.
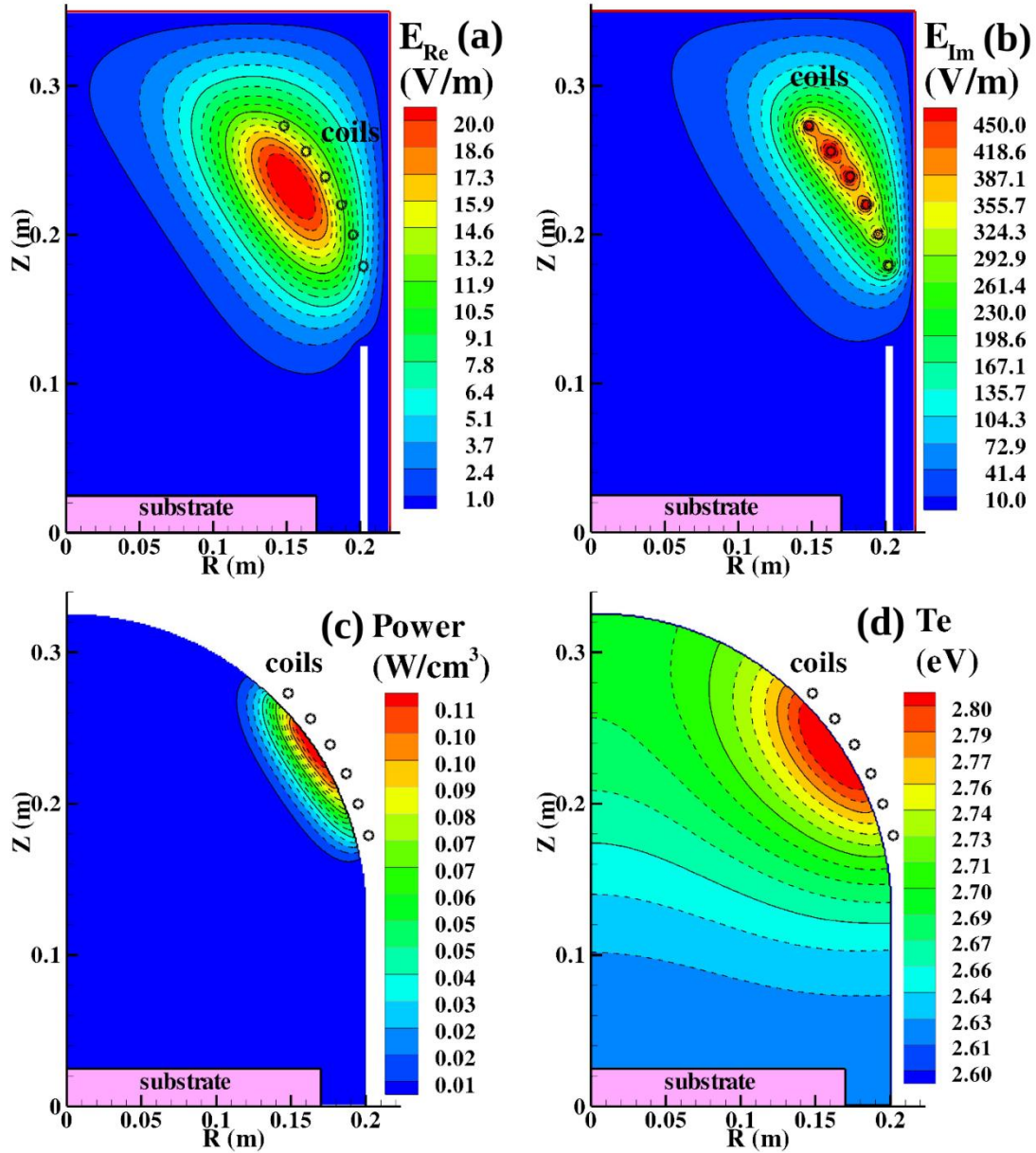
Figure 36: Two-dimensional contour of (*a*) the real part of the induced electric field, (*b*) the imaginary part of the induced electric field, (*c*) the electron temperature T_e and (*d*) the power density in dome-shaped reactor with a power absorption of 150 W and a pressure of 30 mTorr.
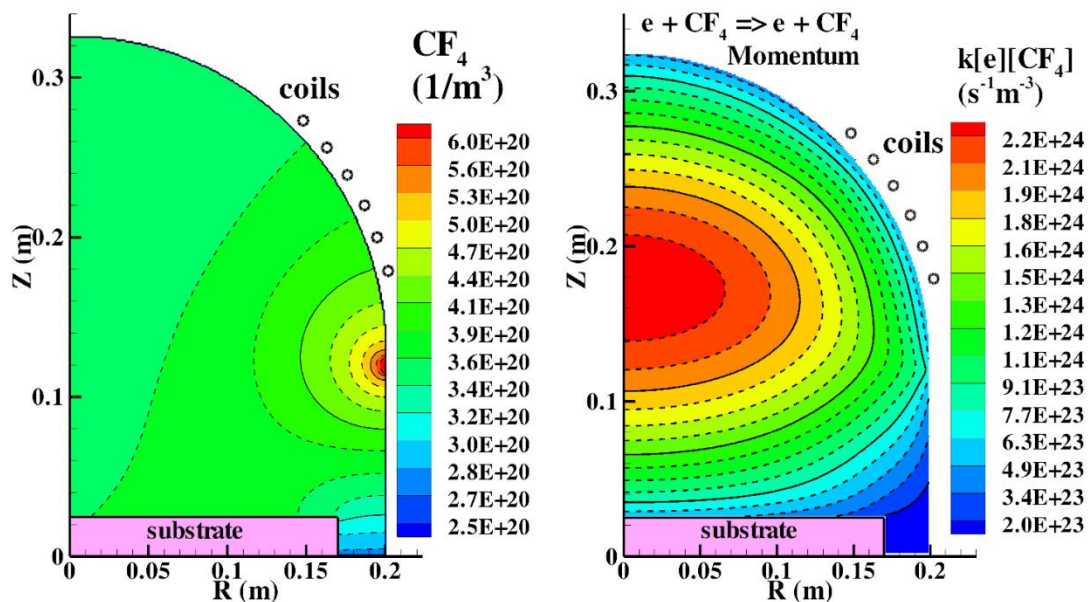
Figure 37: Two-dimensional contour of (*a*) the feeding gas CF₄ in a unit of m⁻³ and (*b*) the production rate for momentum transfer reaction (F00) in unit of m⁻³s⁻¹ (dome-shaped reactor with a power of 200 W and a pressure of 20 mTorr)
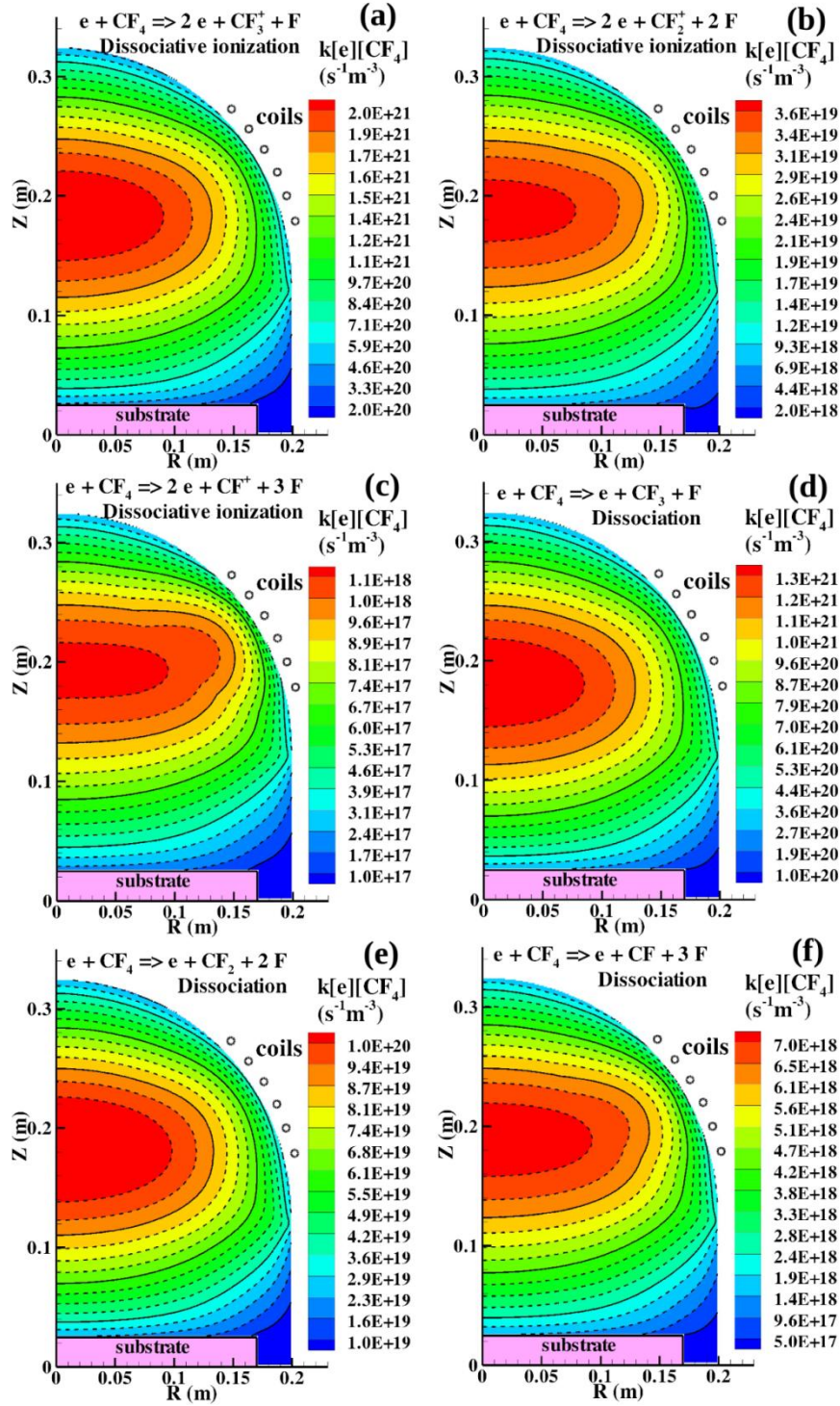
Figure 38: Two-dimensional contour of the production rate ($m^{-3}s^{-1}$) of (*a*) dissociative ionization $e + CF_4 \rightarrow CF_3^+ + F + 2e$ (F05), (*b*) dissociative ionization $e + CF_4 \rightarrow CF_2^+ + 2F + 2e$ (F06), (*c*) dissociative ionization $e + CF_4 \rightarrow CF^+ + 3F + 2e$ (F07), (*d*) dissociation $e + CF_4 \rightarrow CF_3 + F + e$ (F11), (*e*) dissociation $e + CF_4 \rightarrow CF_2 + 2F + e$ (F12) and (*f*) dissociation $e + CF_4 \rightarrow CF + 3F + e$ (F13) in dome-shaped reactor with a power absorption of 200 W and a pressure of 20 mTorr.

Figure 39: Two-dimensional contour of the production rate ($m^{-3}s^{-1}$) of (*a*) dissociative attachment $e + CF_4 \rightarrow CF_3 + F^-$ (**FN01**), (*b*) dissociative attachment $e + CF_3 \rightarrow CF_2 + F^-$ (**FN02**), (*c*) dissociative attachment $e + CF_2 \rightarrow CF + F^-$ (**FN03**) and (*d*) dissociative attachment $e + F_2 \rightarrow F + F^-$ (**FN04**) at a power absorption of 150 W and a pressure of 30 mTorr.
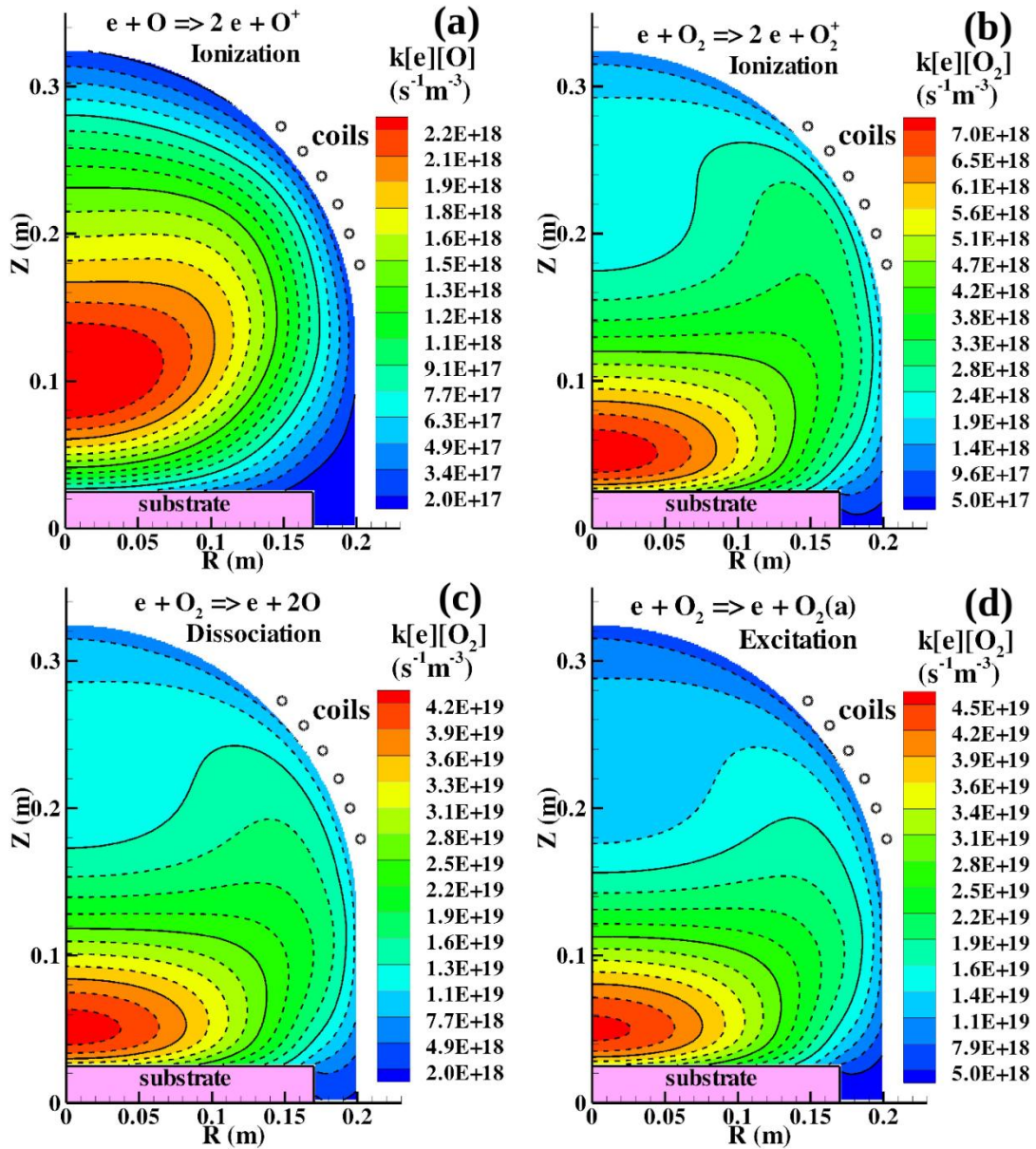
Figure 40: Two-dimensional contour of the production rate (m⁻³s⁻¹) of (*a*) ionization of oxygen atom (F05 $e + O \rightarrow O^+ + 2e$), (*b*) ionization of oxygen molecule (F06 $e + O_2 \rightarrow O_2^+ + 2e$), (*c*) dissociation of oxygen molecule (F07 $e + O_2 \rightarrow 2O + e$), (*d*) excitation of oxygen molecule (F11 $e + O_2 \rightarrow O_2$ (a) + F + e), in dome-shaped reactor with a power absorption of 200 W and a pressure of 20 mTorr.
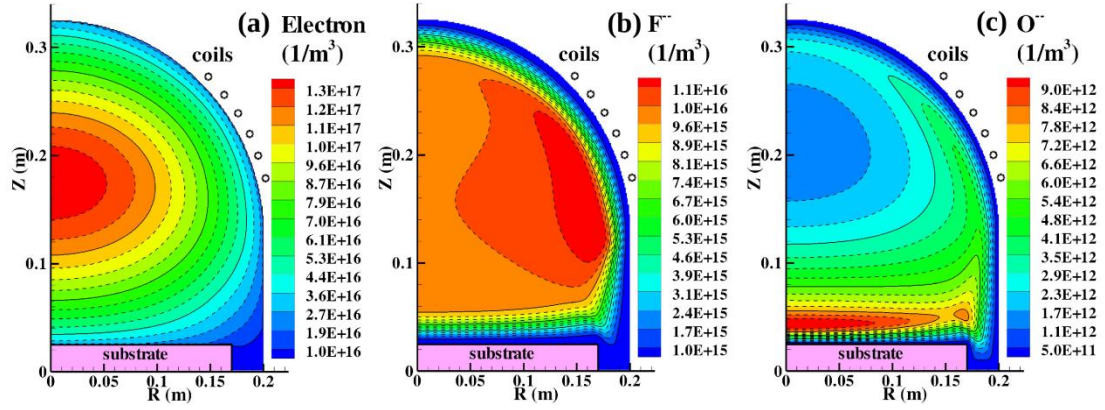
Figure 41 Two-dimensional contour of the (a) electron, (b) F⁻ and (c) O⁻ concentrations in dome-shaped with a power absorption of 200 W and a pressure of 20 mTorr.

Figure 42: Two-dimensional contour of the (*a*) F^+, (*b*) CF^+, (*c*) CF_2^+ and (*d*) CF_3^+ concentrations at a power absorption of 150 W and a pressure of 30 mTorr.

Figure 43: Two-dimensional contour of the (*a*) O⁺, (*b*) O₂⁺ and (*c*) CO⁺ concentrations at a power absorption of 150 W and a pressure of 30 mTorr.

Figure 44: Two-dimensional contour of the (*a*) SiF⁺, (*b*) SiF₂⁺ and (*c*) SiF₃⁺ concentrations in dome-shaped reactor with a power absorption of 200 W and a pressure of 20 mTorr.
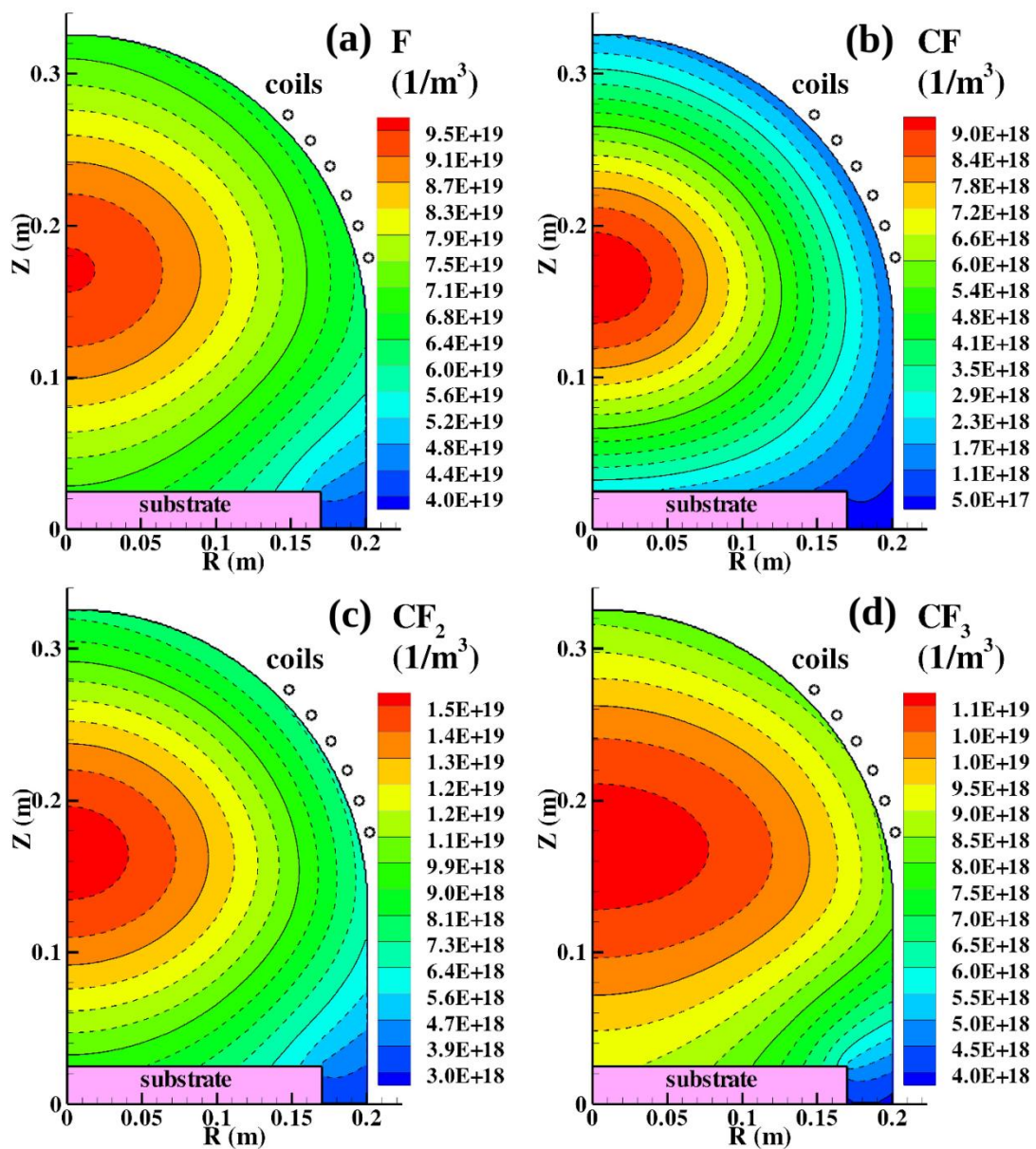
Figure 45: Two-dimensional contour of the (*a*) F, (*b*) CF, (*c*) CF_2 and (*d*) CF_3 concentrations in dome-shaped reactor with a power absorption of 200 W and a pressure of 20 mTorr.
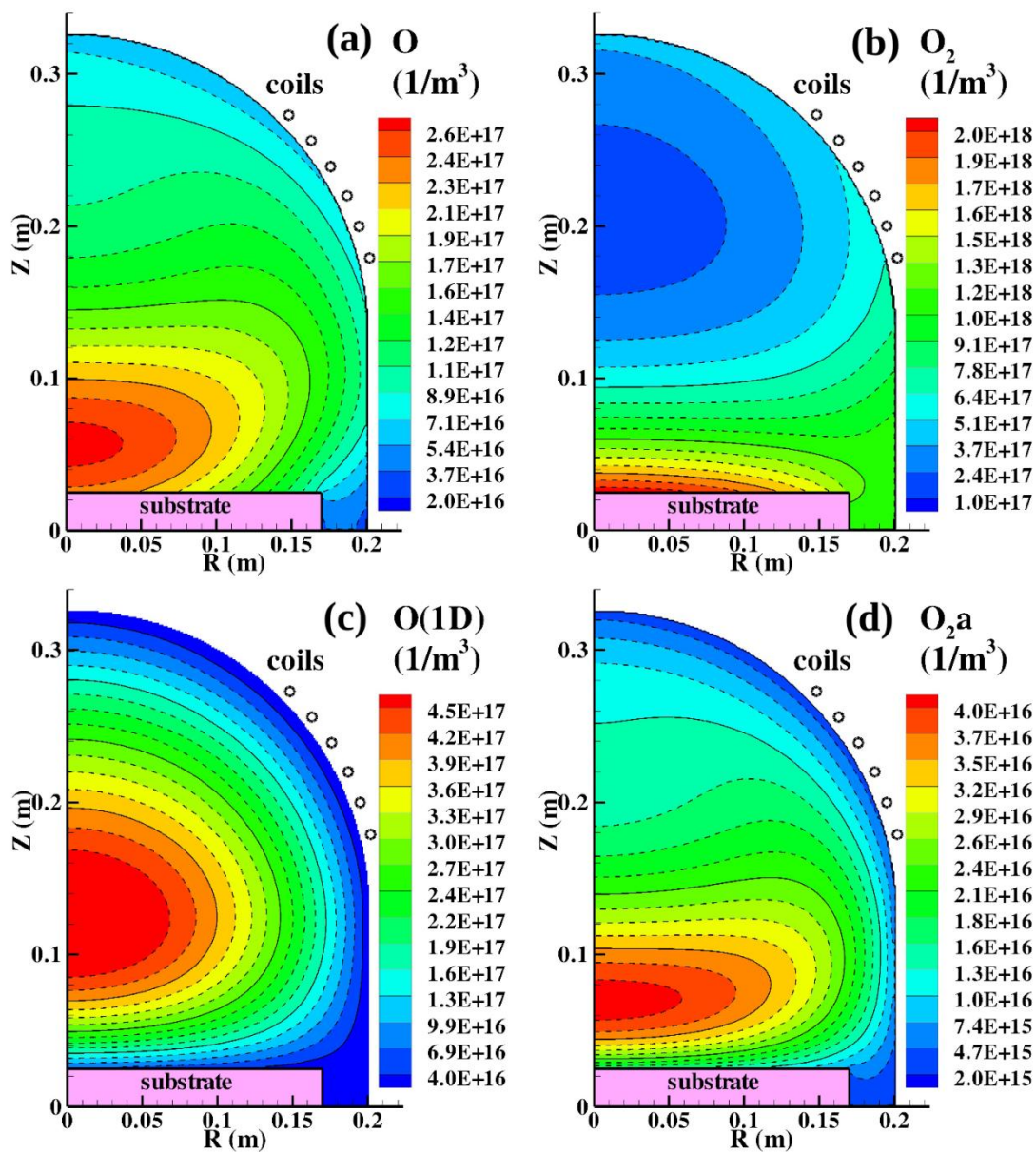
Figure 46: Two-dimensional Contour of (*a*) **O,** (*b*) **O₂,** (*c*) **O(^{1}D) and** (*d*) **O₂(a$^1\Delta_g$)**
concentrations at a power absorption of 150 W and a pressure of 30
mTorr.
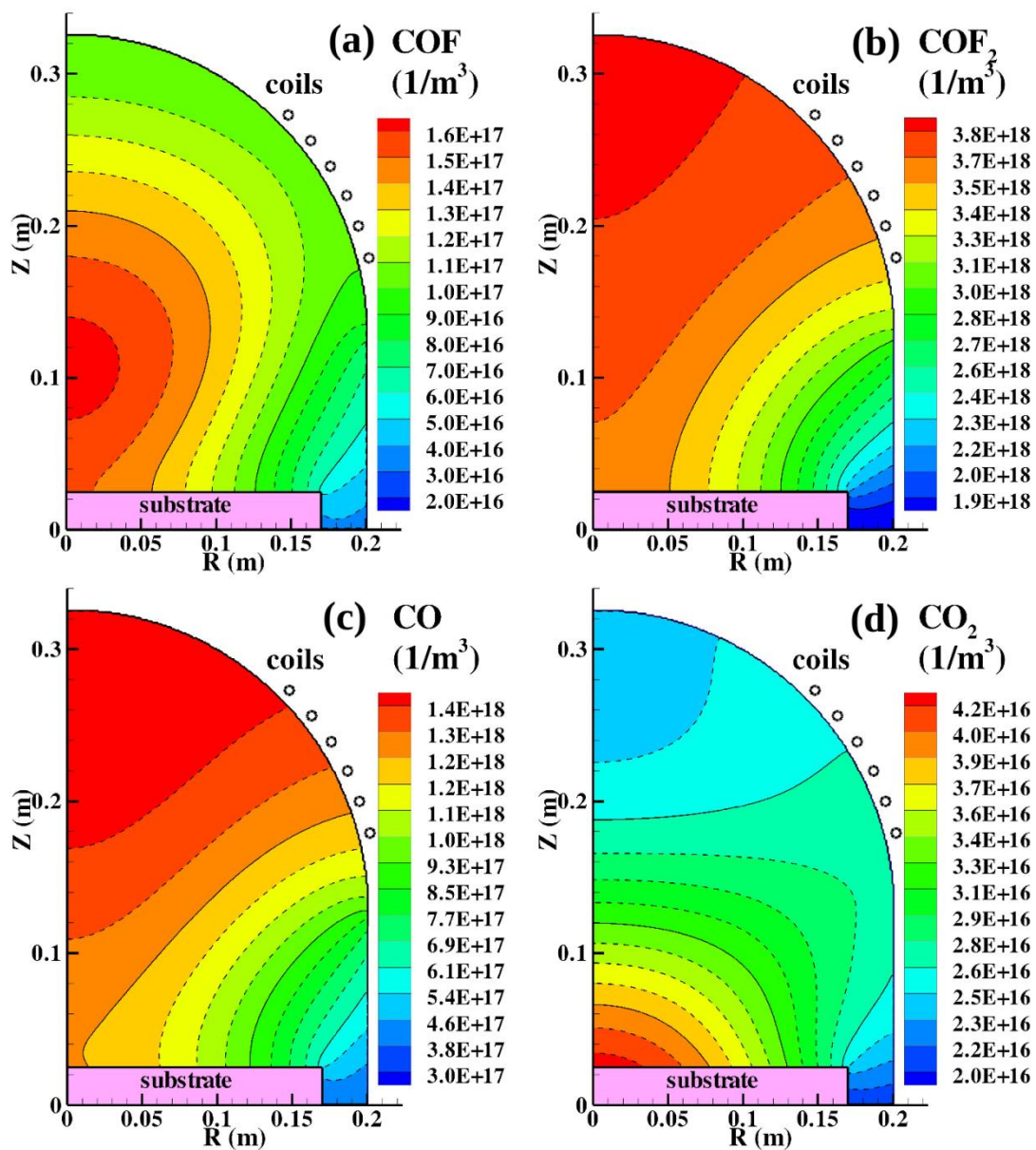
Figure 47: Two-dimensional contour of (*a*) COF, (*b*) COF_2, (*c*) CO and (*d*) CO_2 concentrations in dome-shaped reactor with a power absorption of 200 W and a pressure of 20 mTorr.
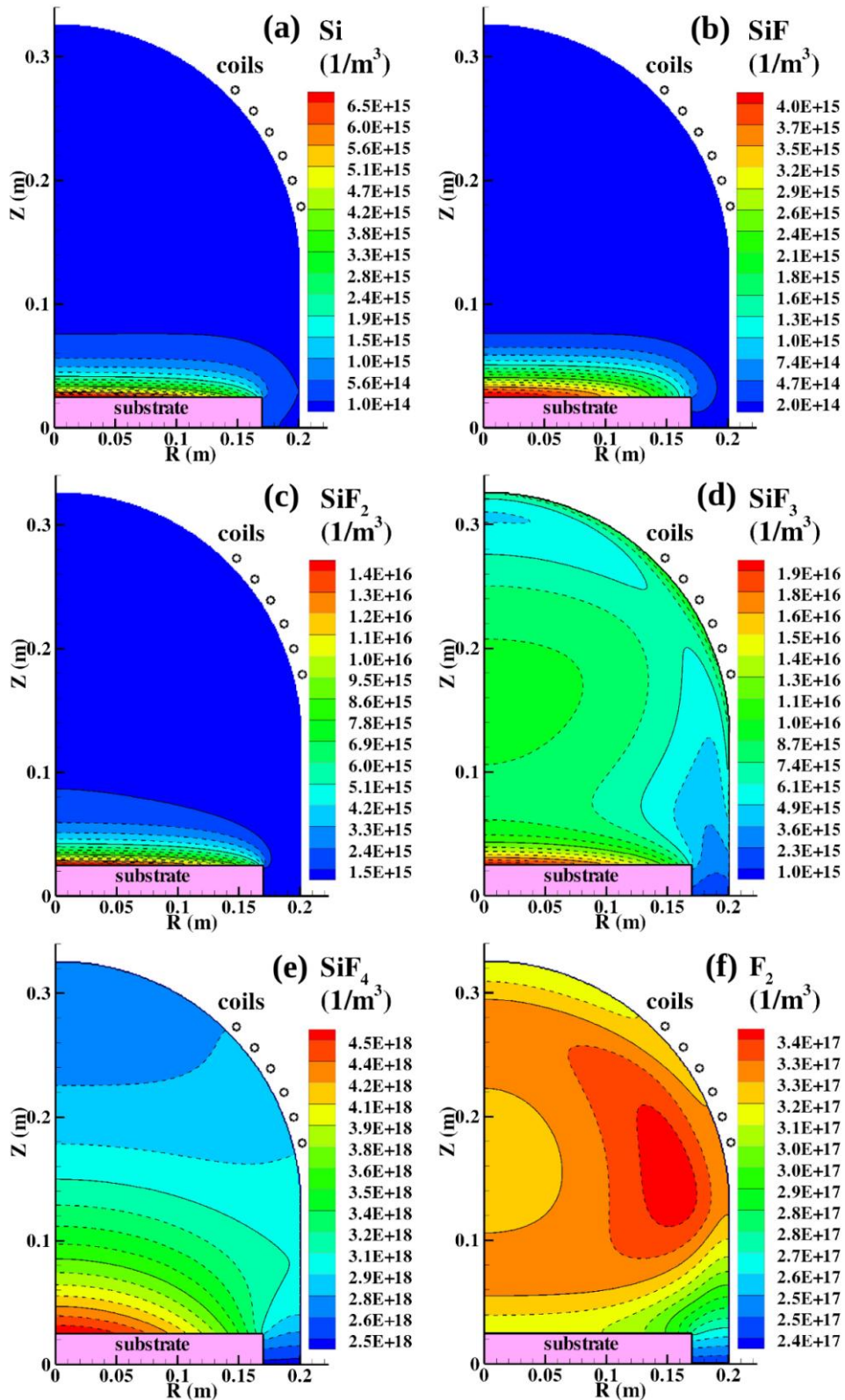
Figure 48: Two-dimensional contour of (*a*) Si, (*b*) SiF, (*c*) SiF$_2$, (*d*) SiF$_3$, (*e*) SiF$_4$ and (*f*) F$_2$ concentrations in the dome-shaped with a power absorption of 200 W and a pressure of 20 mTorr.
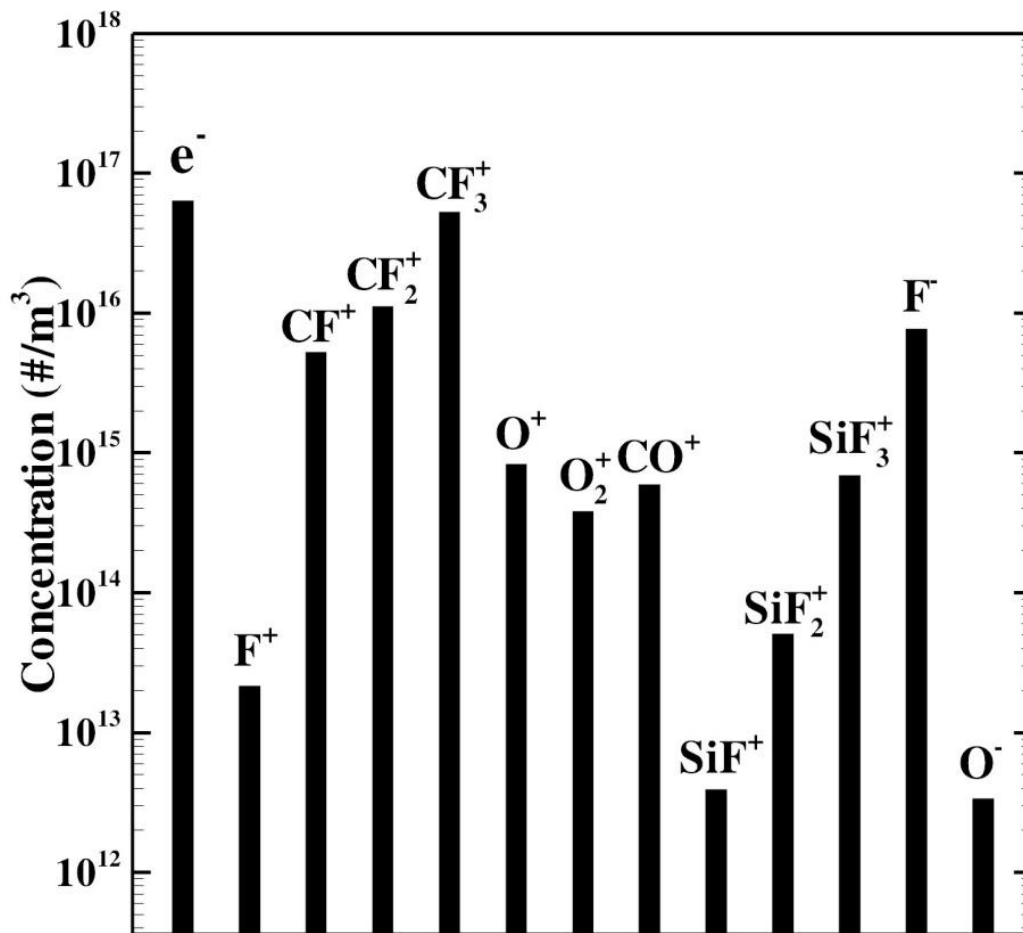
Figure 49: Chemical ingredients of charged species averaged over the entire reactor chamber.
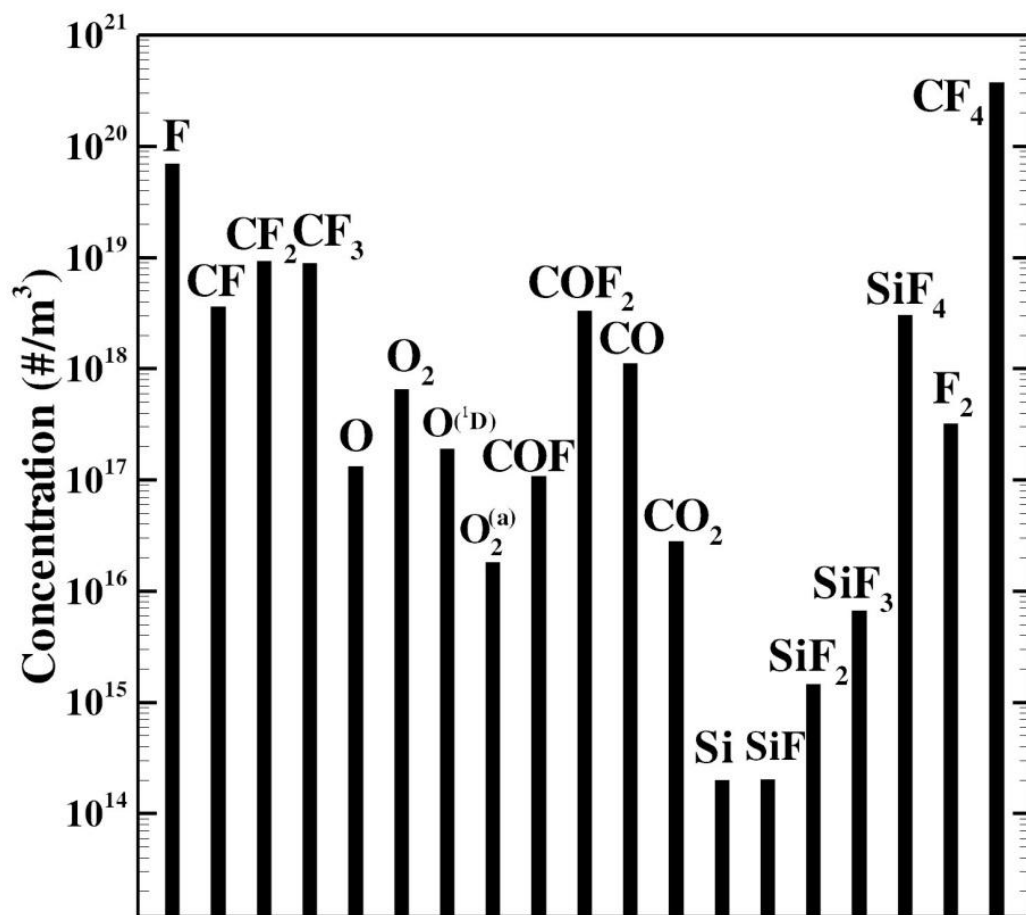
Figure 50: Chemical ingredients of neutral species averaged over the entire reactor chamber.
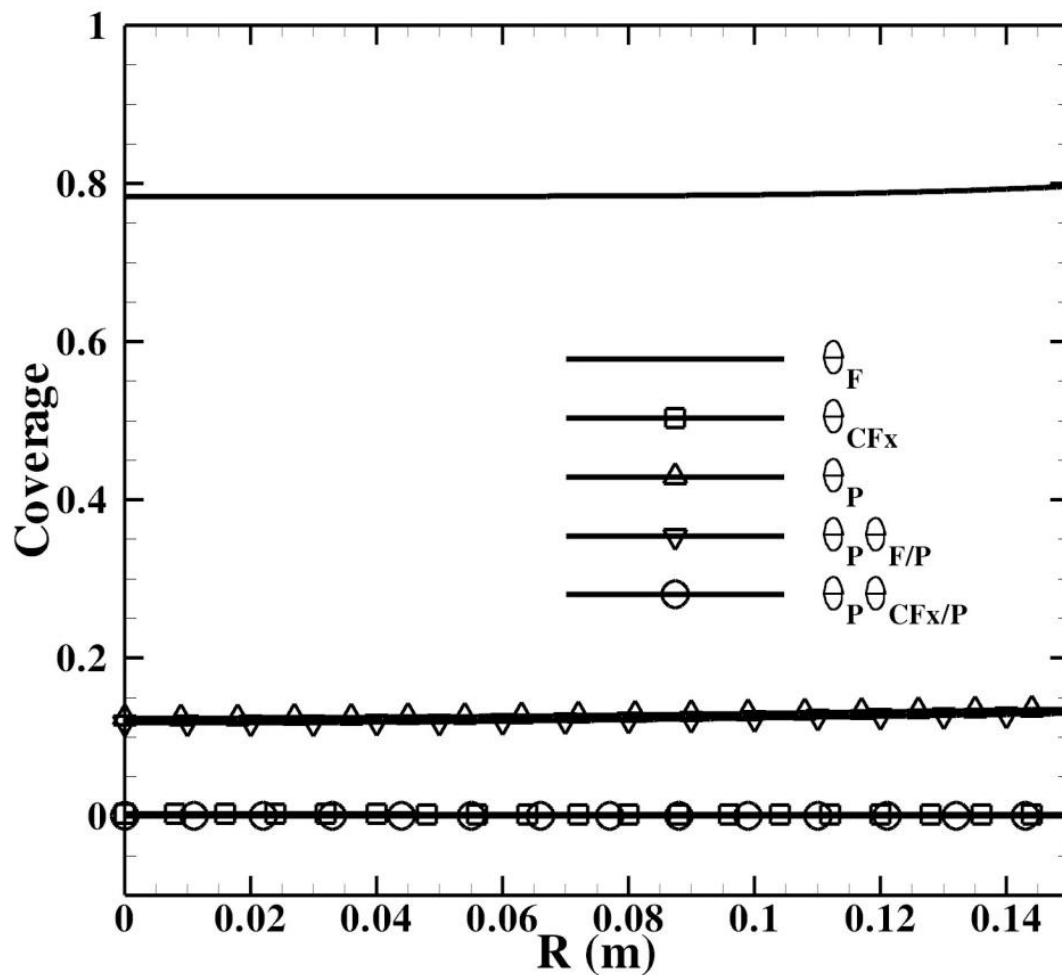
Figure 51: Surface coverages as a function of radial distance on the substrate in dome-shaped reactor.
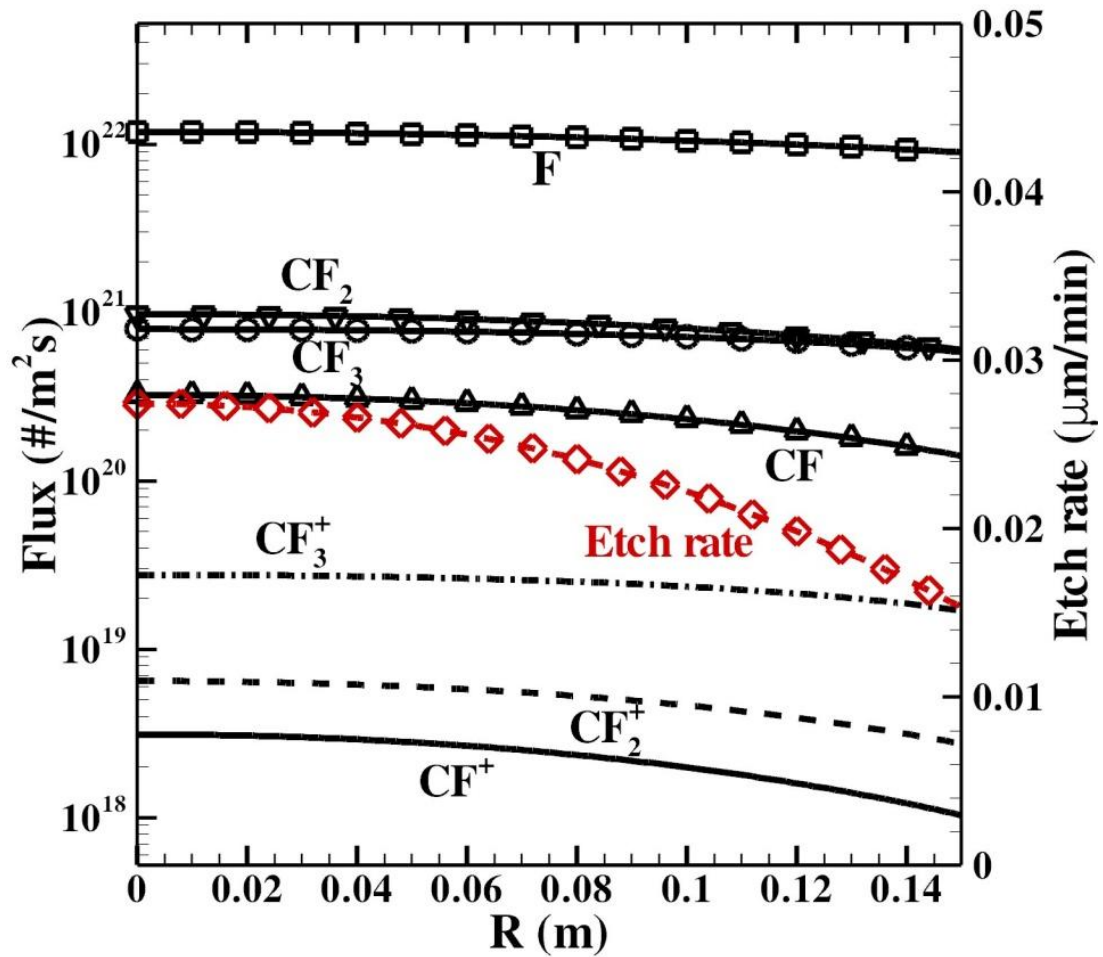
Figure 52: Etch rate, radical fluxes and CF_x^+ ion fluxes as functions of radial distance on the substrate surface in dome-shaped reactor.

157
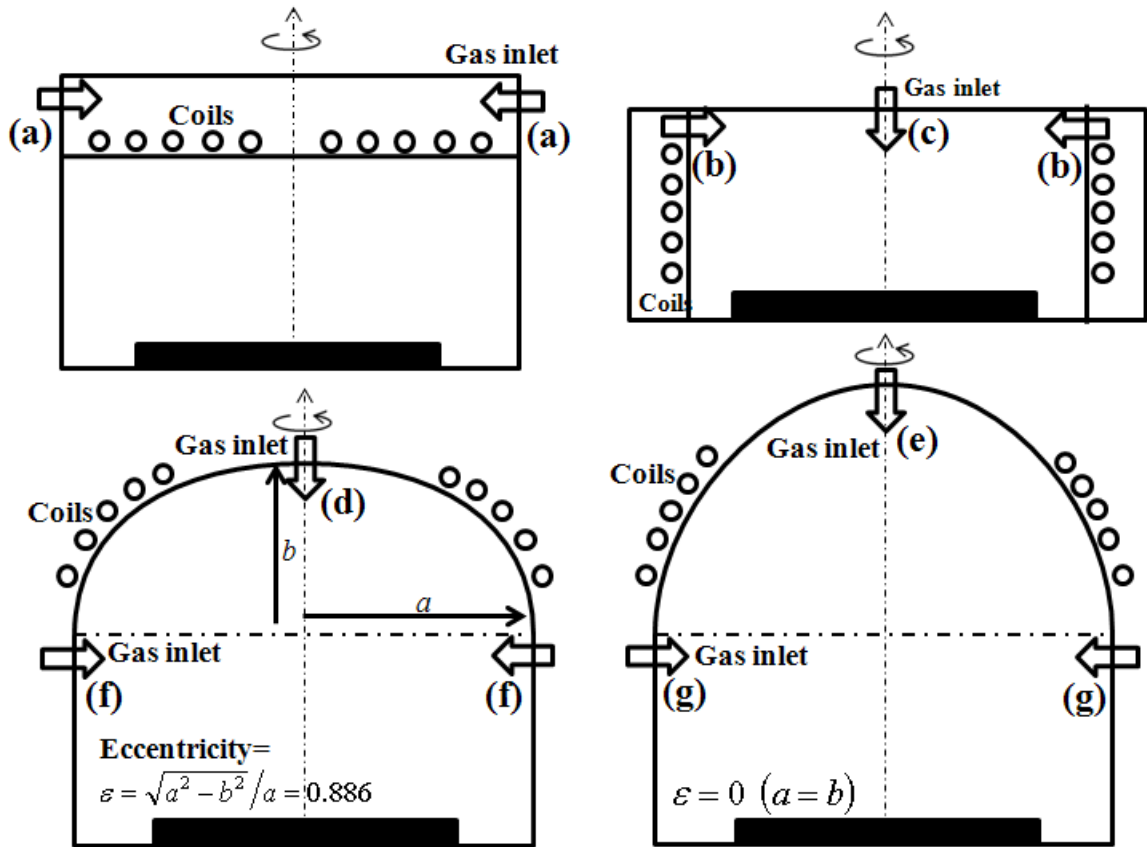
Figure 53: The geometries of CF$_4$ ICP reactors for etching SiO$_2$, coil configurations, and configuration of gas inlet position considered in this paper. (a) gas inlet ring beside typical cylindrical ICP chamber with planar coils, (b) gas inlet ring beside typical cylindrical ICP chamber with cylindrical coils (side), (C) gas inlet port upon typical cylindrical ICP chamber with cylindrical coils (side), (d) gas inlet port upon dome-shaped ICP reactor of elliptic roof, (e) gas inlet port upon dome-shaped ICP reactor of spherical roof, (f) gas inlet ring beside dome-shaped ICP reactor of elliptic roof, and (g) gas inlet ring beside dome-shaped ICP reactor of spherical roof.
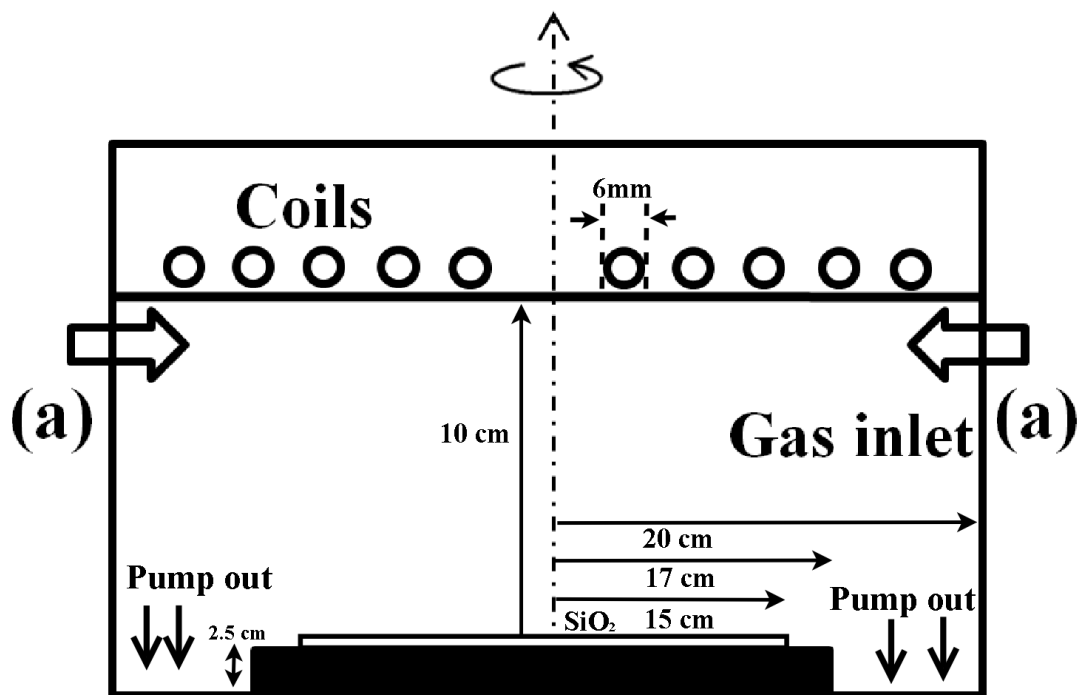
Figure 54: The schematic of typical cylindrical reactor with top coils and beside gas inlet ring.
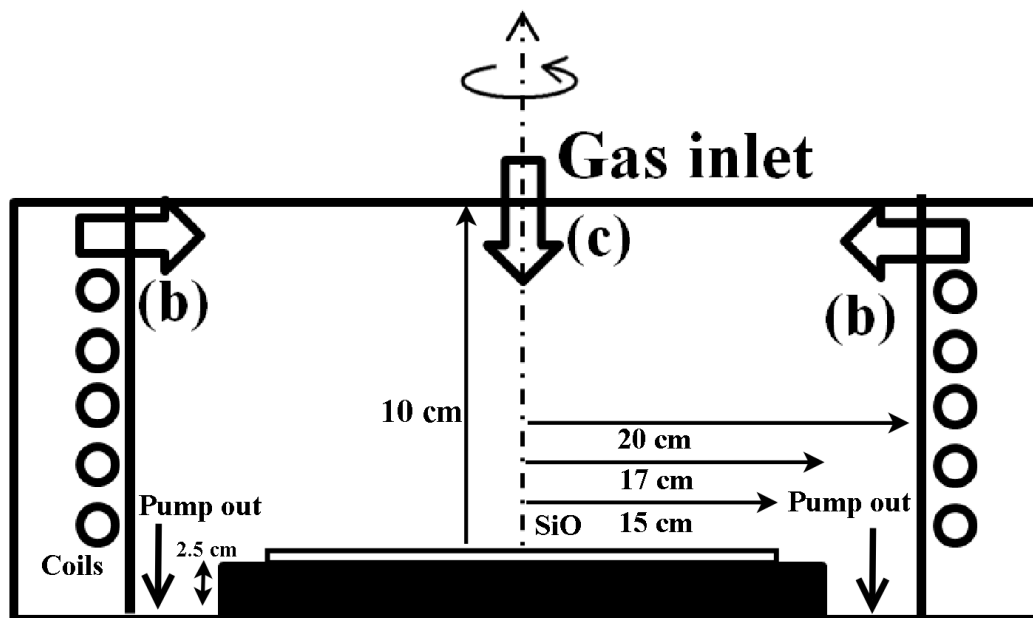
Figure 55: The schematic of typical cylindrical reactor with cylindrical (side) coils and with side or top gas inlet ring.
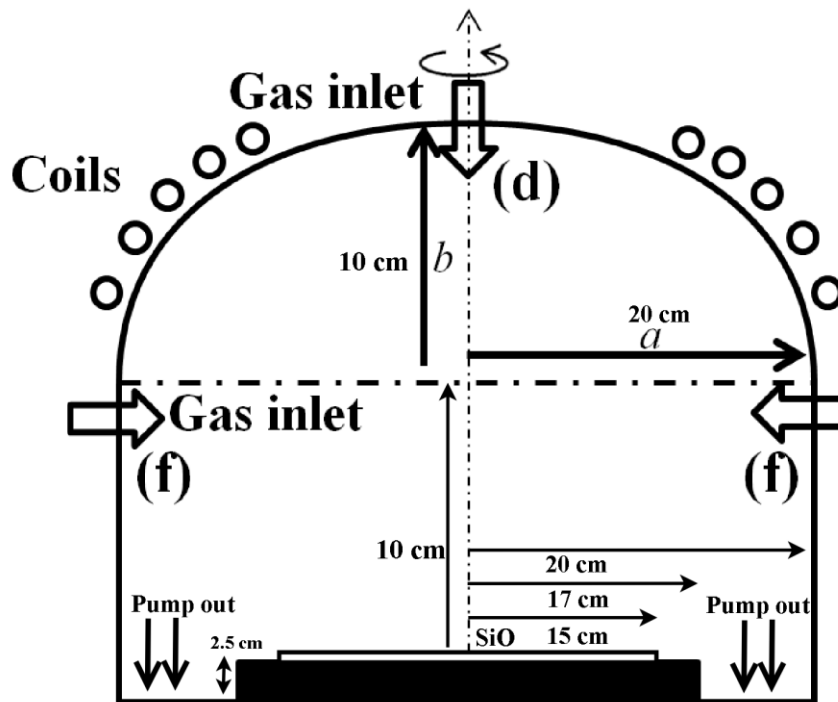
Figure 56: The schematic of dome-shaped reactor (elliptic) with top coil and with side or top gas inlet ring.
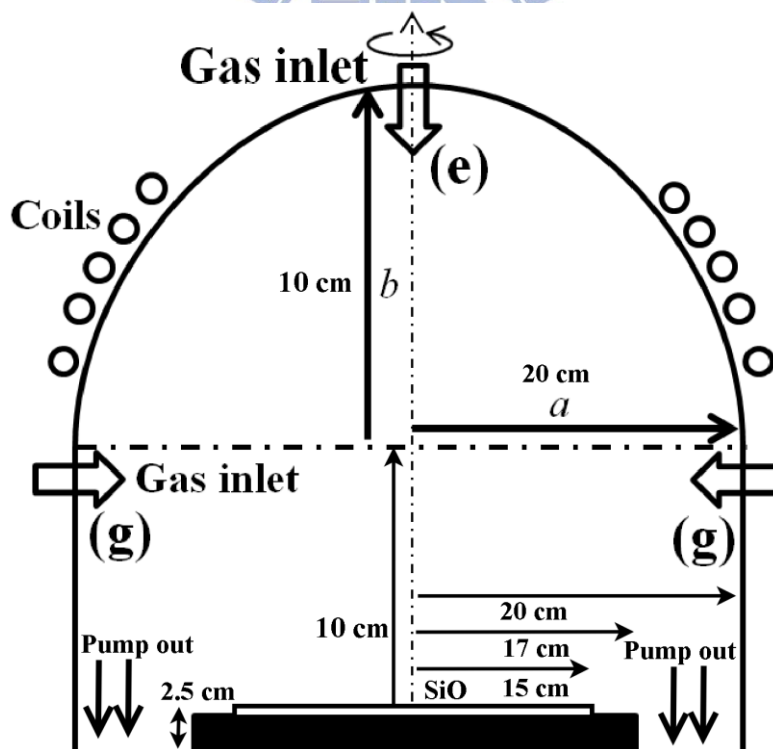
Figure 57: The schematic of dome-shaped reactor (spherical) with top coil and with side or top gas inlet ring.
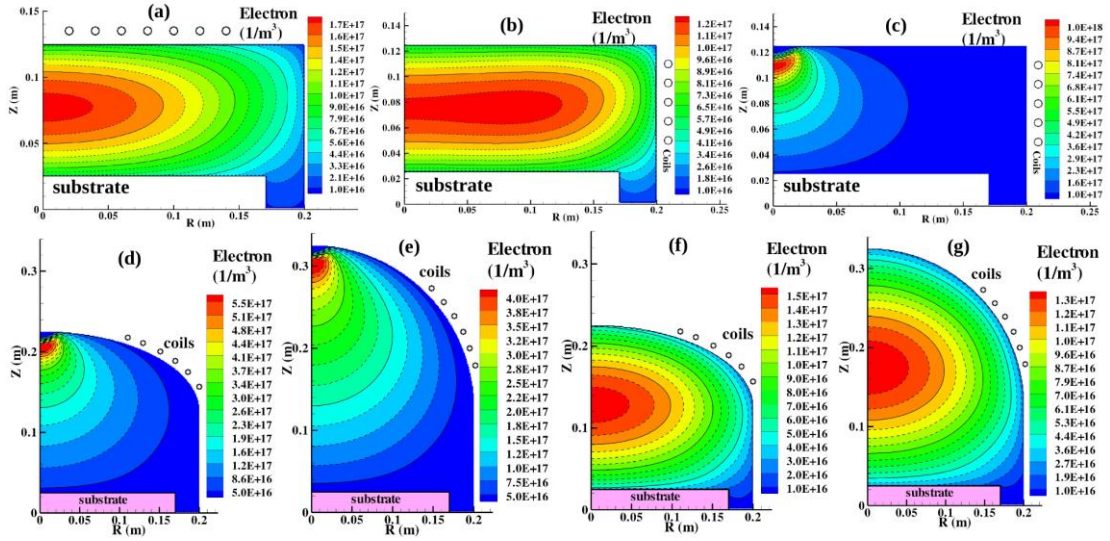
Figure 58: Two-dimensional contour of electron densities (m⁻³) at a power absorption of 200 W and a pressure of 20 mTorr.
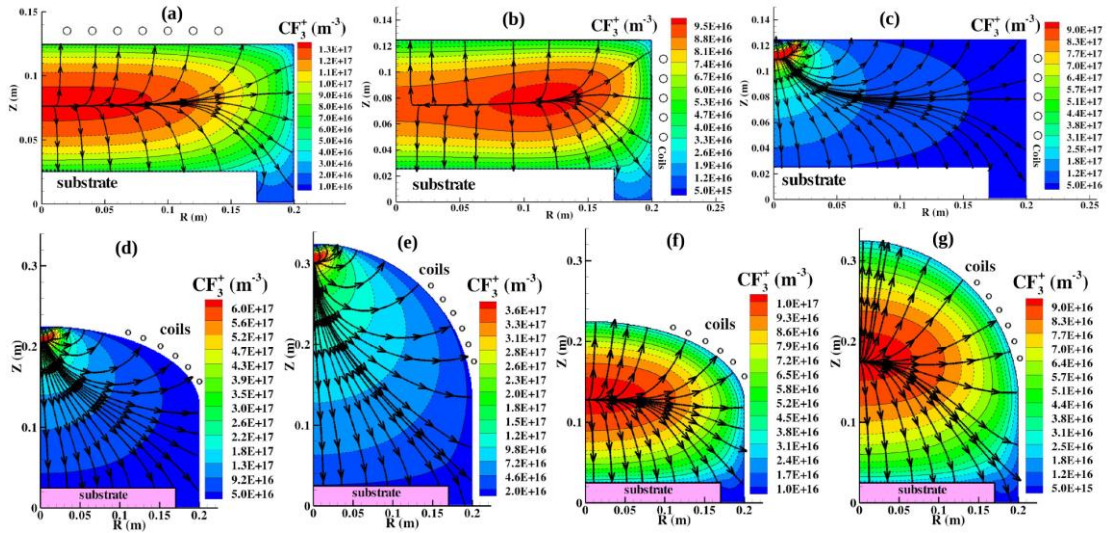
Figure 59: Two-dimensional contour of CF₃⁺ densities (m⁻³) at a power absorption of 200 W and a pressure of 20 mTorr.
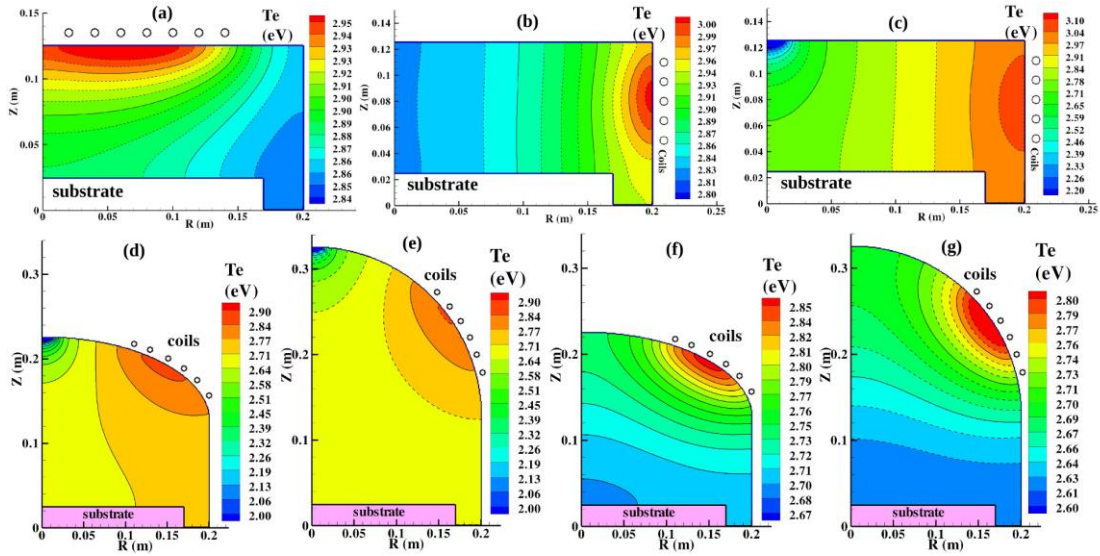
Figure 60: Two-dimensional contour of electron temperature (eV) at a power absorption of 200 W and a pressure of 20 mTorr.
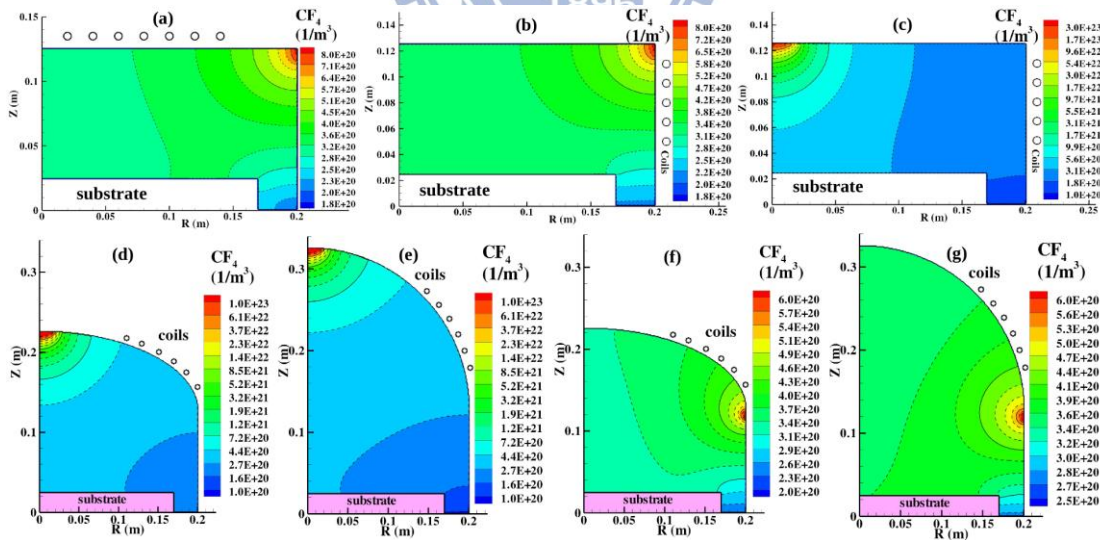
Figure 61: Two-dimensional contour of feedstock gas CF₄ densities (m⁻³) at a flow rate 230 sccm.
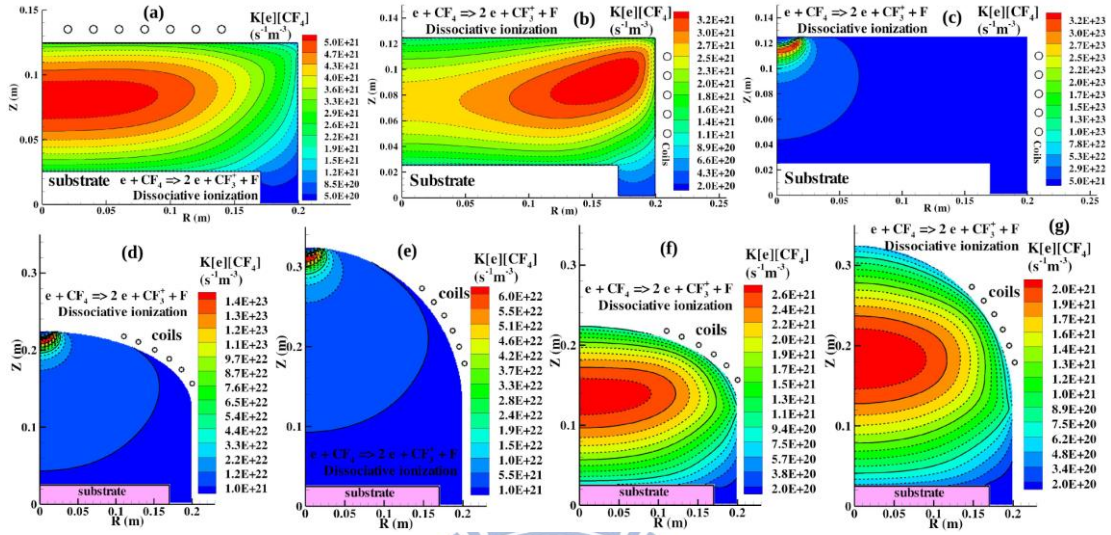
Figure 62: Two-dimensional contour of production rate (dissociative ionization) at a power absorption of 200 W and a pressure of 20 mTorr.
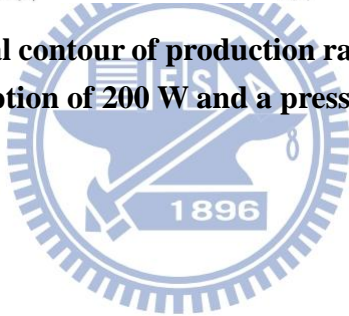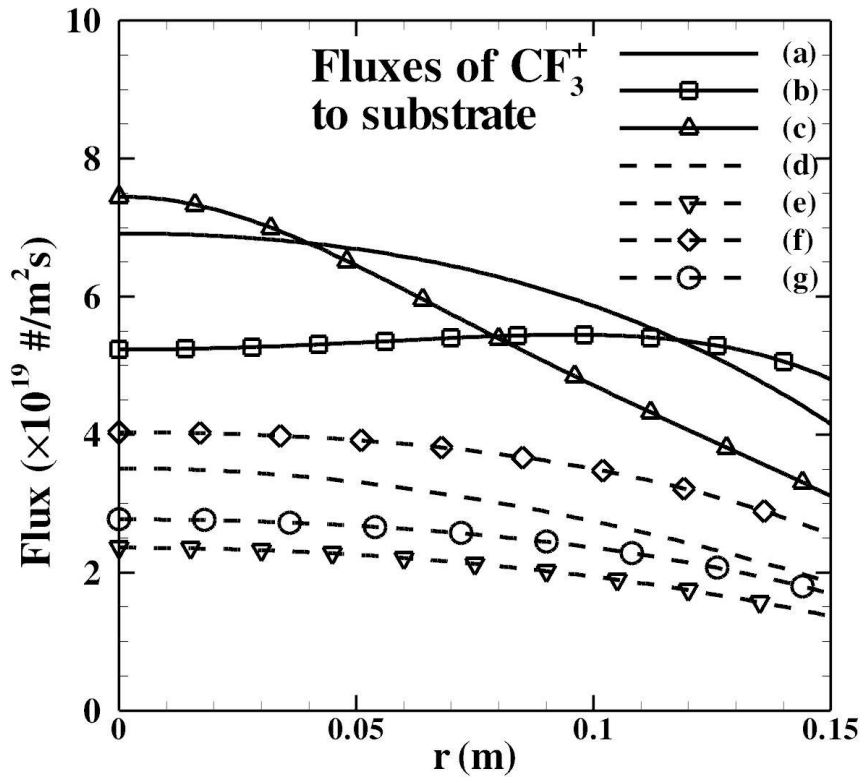
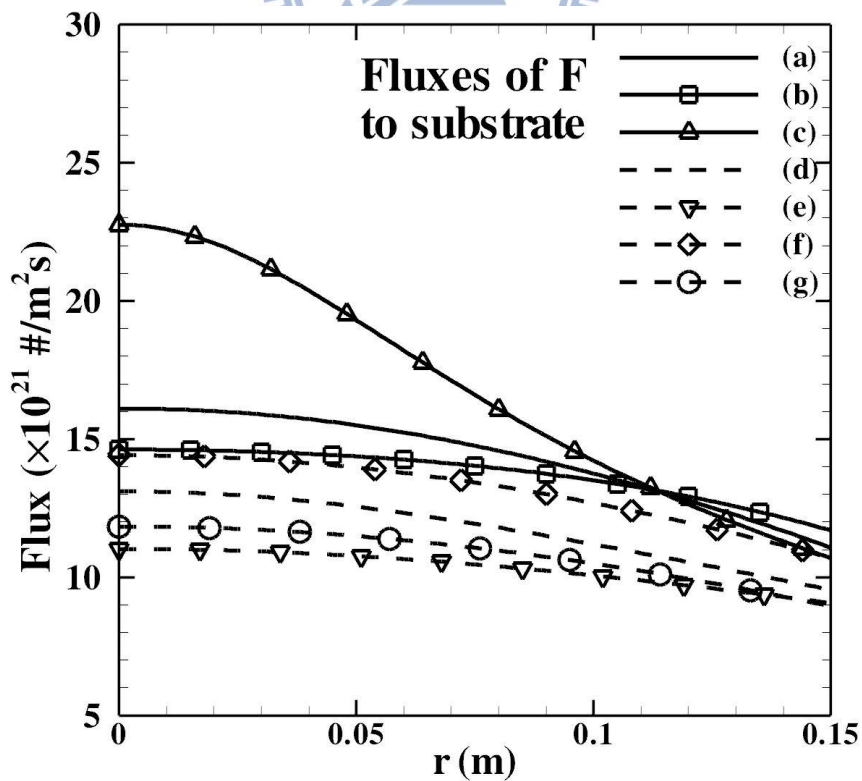**Figure 63: CF_3^+ fluxes as a function of radial distance on the SiO_2 substrate.**

Figure 64: F fluxes as a function of radial distance on the SiO_2 substrate.
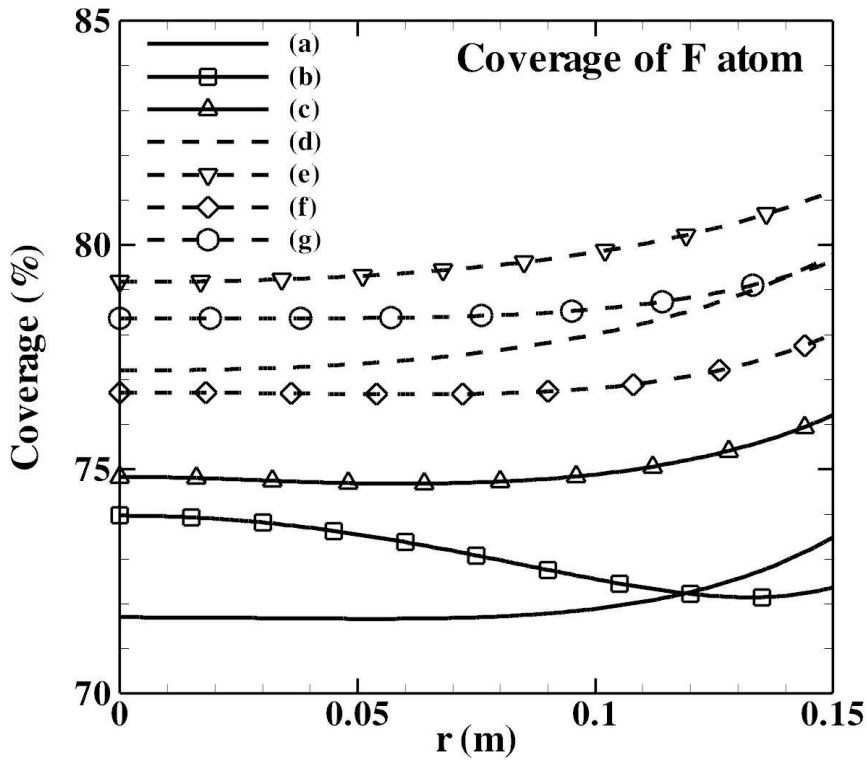
Figure 65: Surface coverages as a function of radial distance on the substrate.
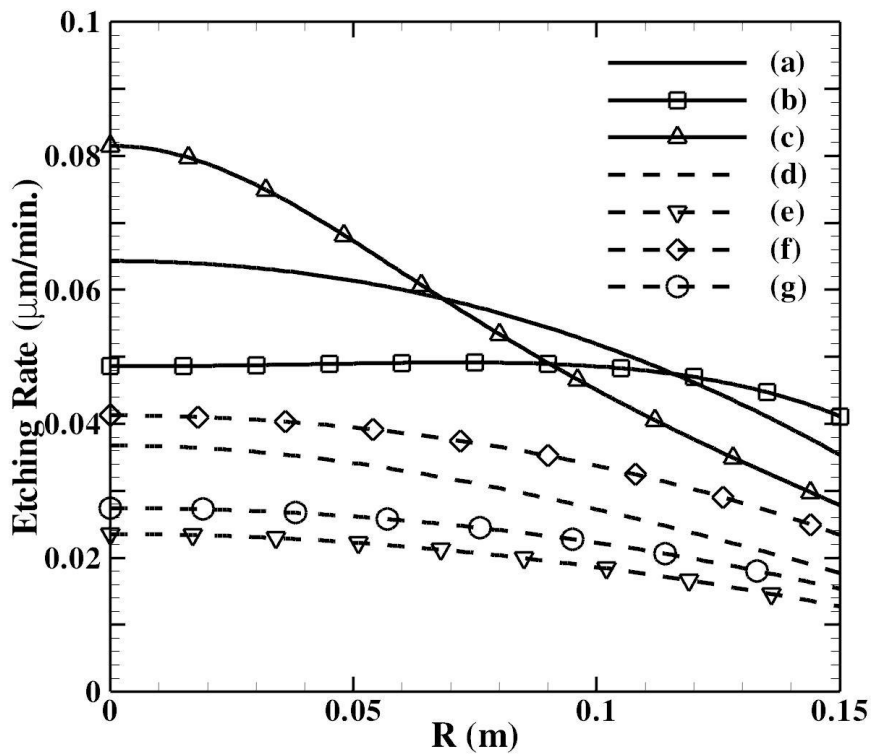

Figure 66: Etching rate as a function of radial distance on the substrate.

LIST OF PUBLICATIONS

Journal Papers:

1. **Y.-M. Chiu**, C.-T. Hung, F.-N. Hwang, M.-H. Chiang, J.-S. Wu*, S.-H. Chen, ″Effect of Plasma Chemistry on the Simulation of Helium Atmospheric-Pressure Plasmas,″ Computer Physics Communications, Vol. 182, pp. 167-169, 2011.

2. C.-T. Hung, **Y.-M. Chiu**, F.-N. Hwang, J.-S. Wu*, ″Development of a Parallel Implicit Solver of Fluid Modeling Equations for Gas Discharges,″ Computer Physics Communications, Vol. 182, pp. 161-163, 2011.

3. C.-T. Hung, **Y.-M. Chiu**, F.-N. Hwang, M.-H. Chiang, J.-S. Wu* and Y.-C. Wang, ″Investigation of the Atmospheric Helium Dielectric Barrier Discharge Driven by a Realistic Distorted-Sinusoidal Voltage Power Source,″ Plasma Chemistry and Plasma Processing, Vol. 31, No. 1, pp. 1–21, 2011.

4. S.-Y. Jou, C.-T. Hung, **Y.-M. Chiu**, J.-S. Wu*, B.-Y. Wei, ″Simulation of Excimer Ultraviolet (EUV) Emission from a Coaxial Xenon Excimer Ultraviolet Lamp Driven by Distorted Bipolar Square Voltages,″ Plasma Chemistry and Plasma Processing, Vol. 30, pp. 907–931, 2010.

5. S.-Y. Jou, C.-T. Hung, **Y.-M. Chiu**, J.-S. Wu*, B.-Y. Wei, ″Enhancement of VUV Emission from a Coaxial Xenon Excimer Ultraviolet Lamp Driven by Distorted Bipolar Square Voltages,″ Contributions to Plasma Physics, pp. 1-14, 2011.

6. K.-W. Cheng, C.-T. Hung, K.-M. Lin, **Y.-M. Chiu**, J.-S. Wu* and J.-P. Yu, ″Fluid Modeling of a Nitrogen Atmospheric-Pressure Planar Dielectric Barrier Discharge Driven by a Realistic Distorted Sinusoidal AC Power Source,″ Japan Journal of Applied Physics, 2012

7. **Yuan-Ming Chiu**, Chieh-Tsan Hung, Jong-Shinn Wu, and Feng-Nan Hwang, "Parallel 2-D Axisymmetrical Fluid Modeling of Tetrafluoromethane Gas Discharge in an Inductively Coupled Plasma Source" , Plasma Sources Science and Technology 2012 (Submitted)

8. **Yuan-Ming Chiu**, Chieh-Tsan Hung, Jong-Shinn Wu, and Feng-Nan Hwang, "Comparison of Etching Properties of Various Inductively Coupled Plasma Sources Using Parallel Fluid Modeling", Journal of Physics D: Applied Physics (Preparing to submit)

166

Internal Conference Papers:

1. **Ying-Ming Chiu**, Chieh-Tsan Hung, Feng-Nan Hwang, J.-S. Wu* and Shiaw-Huei Chen, "Effect of plasma chemistry on the simulation of helium atmospheric-pressure plasmas," Conference on Computational Physics (CCP) 2009, Kaohsiung, Taiwan, December 15-19, 2009.

2. **Y.-M. Chiu**, C.-T. Hung, J.-S. Wu*, Feng-Nan Hwang, "Development of Parallel Fluid Modeling for Non-equilibrium Inductively Coupled Plasma", 7th International Conference on Flow Dynamics, p. 166, Sendai, Japan, November 1-3, 2010.

3. **Y.-M. Chiu**, C.-T. Hung, J.-S. Wu*, F.-N. Hwang, "Development of Parallel Fluid Modeling for Low-temperature Inductively Coupled Plasma Source in Etching or Deposition Process," 8th International Conference on Flow Dynamics, p. 382, Sendai, Japan, November 9-11, 2011.

4. **Y.-M. Chiu**, C.-T. Hung, J.-S. Wu*, F.-N. Hwang, "Parallel Fluid Modeling for Low-temperature Inductively Coupled Plasma Etching Process Using Carbon Tetrafluoride", 7th Asia-Pacific International Symposium on the Basics and Applications of Plasma Technology (APSPT-7), Taipei, Taiwan, April 14-16, 2012.

Domestic Conference Papers:

1. **Y.-M. Chiu**, C.-T. Hung, J.-S. Wu*, F.-N. Hwang, "Parallel Fluid Modeling of Silane Gas Discharge in an Inductively Coupled Plasma Source," 18th Computational Fluid Dynamics Conference in Taiwan, Yilan, Taiwan, August 3-5, 2011

2. **Y.-M. Chiu**, C.-T. Hung, J.-S. Wu* and F.-N. Hwang, "Parallel Fluid Modeling for Low-temperature Inductively Coupled Plasma Etching Process using Carbon Tetrafluoride," NCHC User Conference, Hsinchu, November 24, 2011.
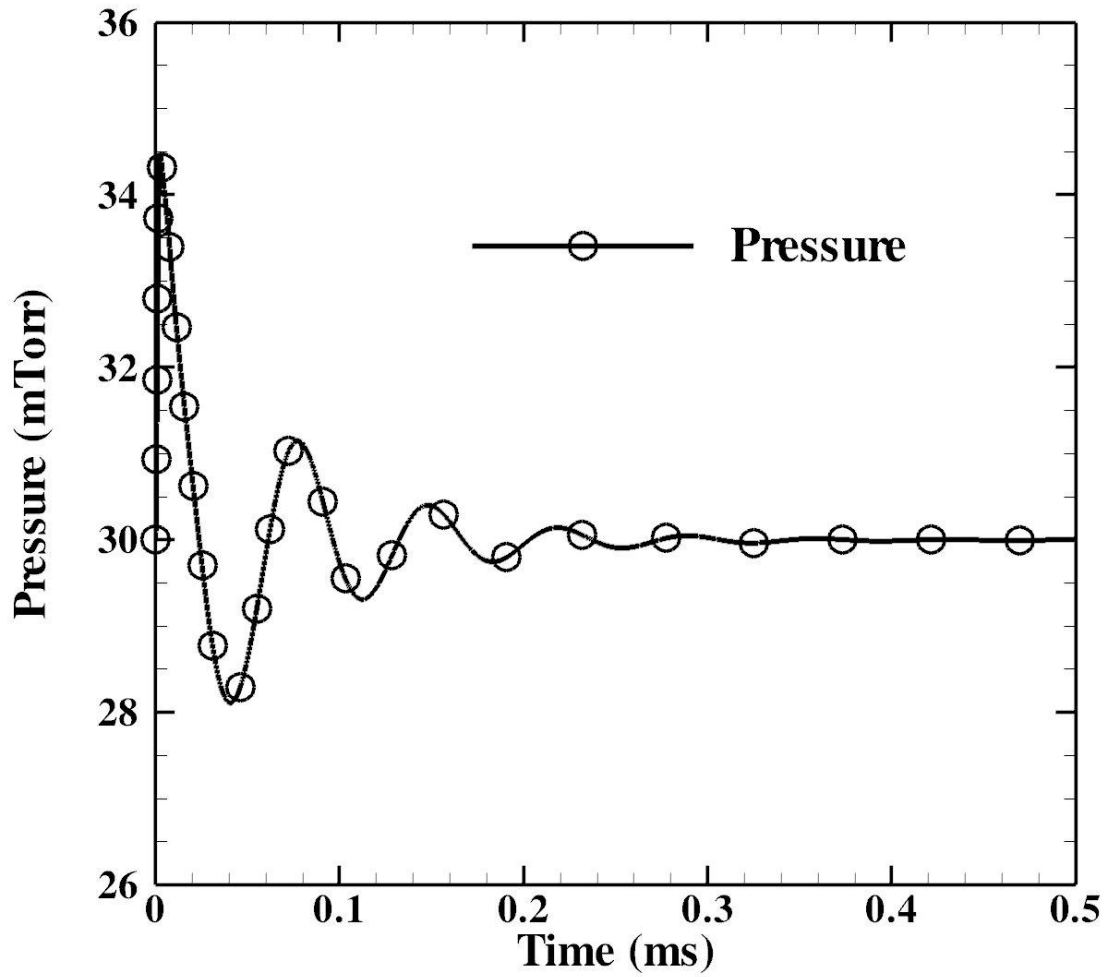
APPENDIX A

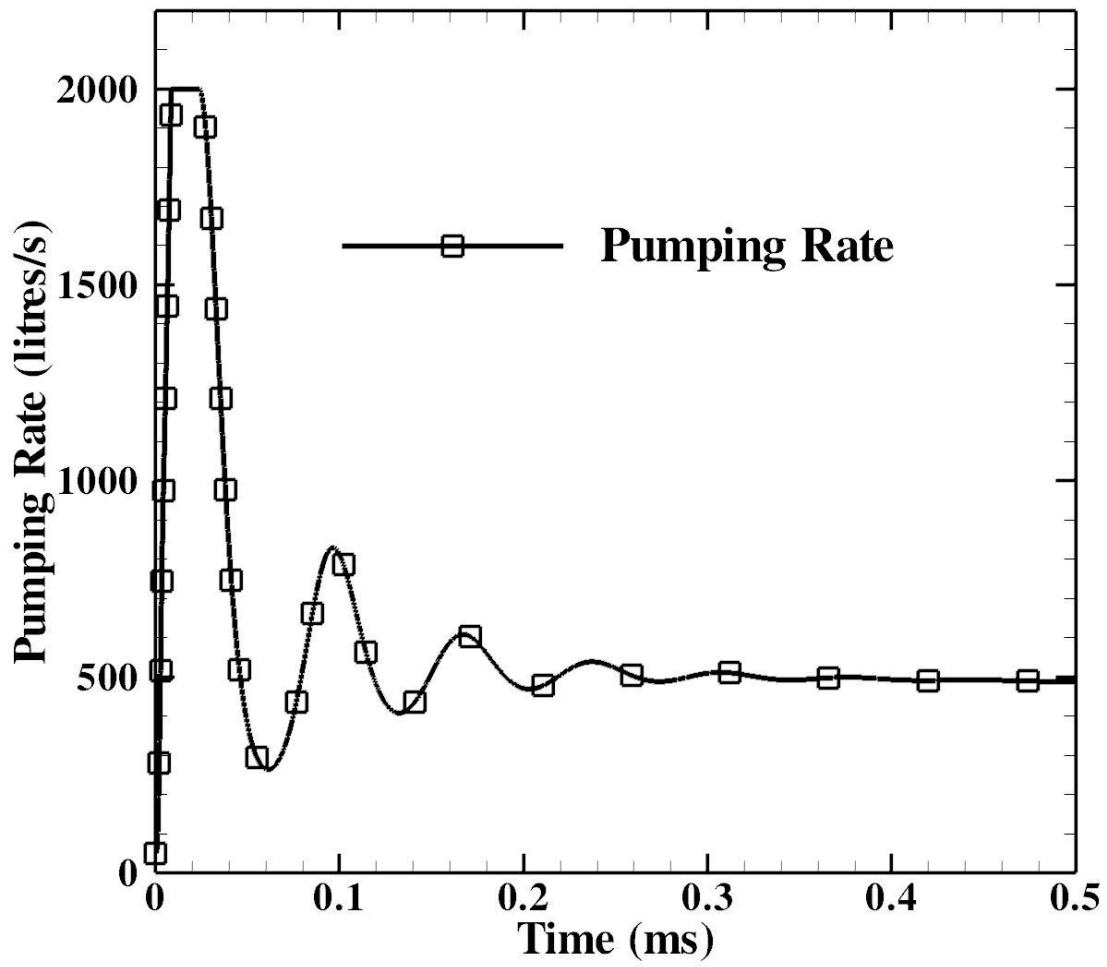**Figure A-1: Time evolution of total pressure averaged entire reactor (GECRC).**

Figure A-2: Time evolution of pumping rate (GECRC).
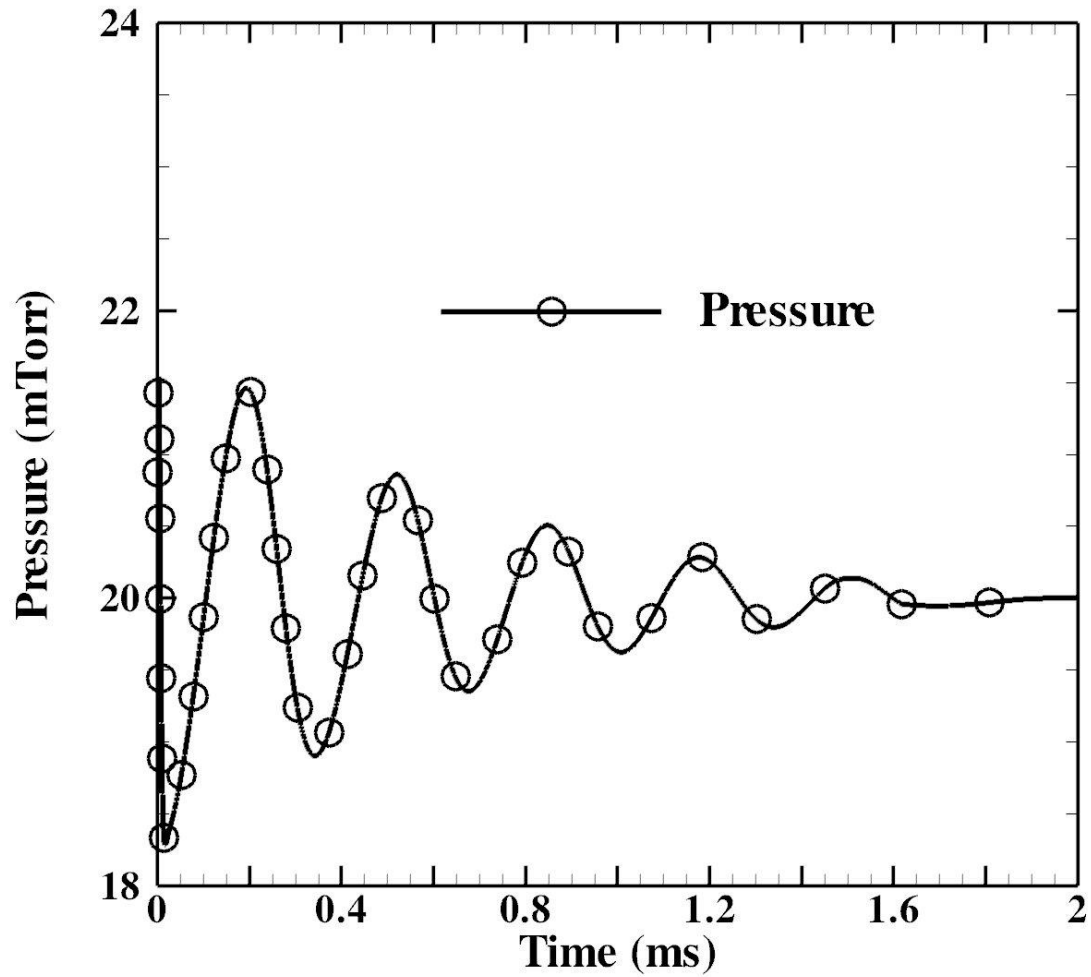
APPENDIX B

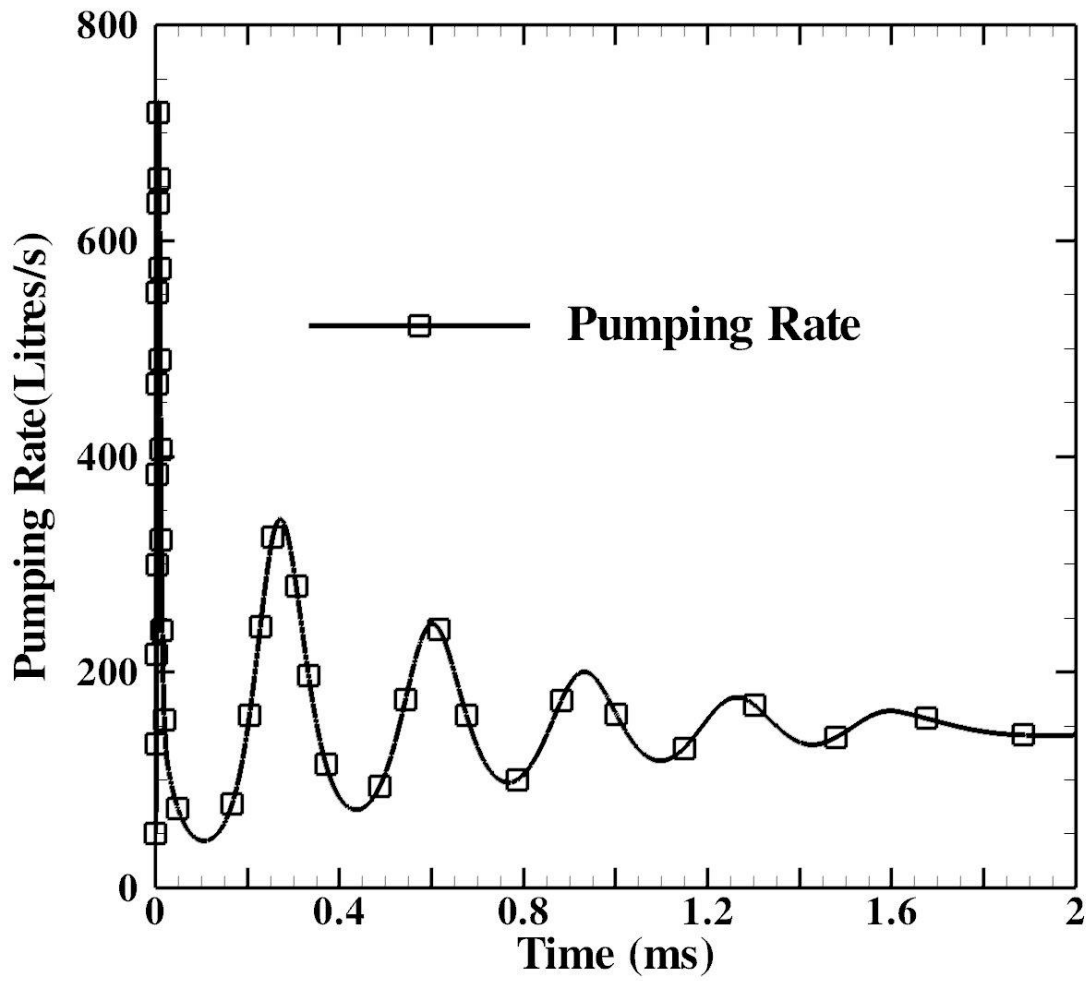**Figure B-1: Time evolution of total pressure averaged entire reactor (Dome-shaped reactor).**

Figure B-2: Time evolution of pumping rate (Dome-shaped reactor).